University of South-Eastern Norway

www.usn.no

FMH606 Master's Thesis 2023
Electrical Power Engineering

Data acquisition application with implemented digital twin based on thermal and electrical parameters and state estimation of a real synchronous generator

Fredrik Andre Strøm

Faculty of Technology, Natural Sciences and Maritime Sciences
Campus Porsgrunn

University of South-Eastern Norway

www.usn.no

Course: FMH606 Master's Thesis 2023

Title: *Data acquisition application with implemented digital twin based on thermal and electrical parameters and state estimation of a real synchronous generator*

Pages: *129*

Keywords: *Synchronous Machine, Parameter estimation, State Estimation, Kalman Filter, Extended Kalman Filter, Bayesian inference, 4th order synchronous generator, Thermal model, LabView, Data acquisition*

Student: *Fredrik Andre Strøm*

Supervisor: *Thomas Øyvang and Emil Ghieh Melfald*

External partner: *Kelda and Tinfos*

Summary:

The synchronous generator is a vital part of the electrical power system. During normal operation conditions, the generator units have power losses which affect the machine's efficiency and operating temperatures. Mechanistic models of the generator can help increase the knowledge of the machine's operating conditions. This relies on model parameters to be known and the models to be sufficiently representative. The project was resolved around further development of a data acquisition application with a digital twin, built on mechanistic models of the electrical, power loss and thermal phenomenons in the generator. In addition, was electrical and thermal parameter and state estimation procedures investigated and carried out through three study cases.

Standard electrical parameters were identified with low deviation. An extended Kalman filter was proposed to estimate the rotor angle from noisy measurements of the rotor angle. Resulting estimations after the extended Kalman filter was applied presented promising results, with lowered deviations and low correlation between parameters.

A simplified thermal model of the generator was developed, and thermal parameters were estimated based on two separate measurement sessions. The results support some of the assumptions that were made when developing the thermal model, yet, other simplifications are proven too comprehensive.

The University of South-Eastern Norway accepts no responsibility for the results and conclusions presented in this report.

Preface

This Master's thesis was written at the University of South-Eastern Norway during the spring semester of 2023, written as a dissertation finalizing a Master's degree in Electrical Power Engineering. Tinfos and Kelda were external partners in the master's thesis project. The master's thesis was done as a continuation of a master's project, continuing the work towards developing a data acquisition application for use with the test rig at USN. The work has proved an exciting challenge with both practical and theoretical challenges to establishing a data acquisition application, as well as parameters, and state estimation of the generator. Several of the project challenges proved time-consuming, which to some extent caused the last sub-objective, (O8), not to be accomplished yet. The implementation of software AVR did prove unstable when tested with soft sensors, resulting in the control method not being implemented into the data acquisition application. Some of the main features of the application are showcased through short videos, submitted as part of the electronic appendices, Appendix D, with the videos in E3.

I want to thank my supervisor and professor, Thomas Øyvang, for preserving me on the project and continuing with excellent support throughout the work. I also want to thank him for the opportunity to attend PTK, which proved exciting and gave me a great insight into the working environment I am stepping into upon completing my master's degree. I also want to thank my supervisor and PhD candidate Emil Ghieh Melfald for allowing close communication throughout the project work. His guidance has been impeccable, both in regard to practical wiring and assistance at the laboratory and theoretical discussions on the thesis subjects.

Finally, I want to thank my family for their immense unconditional support. It would not be possible to complete this master's degree without it. Porsgrunn, 15th May 2023

Fredrik Andre Strøm

Contents

List of Figures

List of Tables

Nomenclature

Symbol	Explanation
AVR	Automatic voltage regulator
$\cos\phi$	Powerfactor of the power [-]
D	Damping coefficient
δ	Rotor angle [rad]
emf	Electromotive force [V]
ε	Emissivity, heat transfer through radiation
F	Magnetomotive force [AT]
h	Total heat transfer coefficient $[W/(KA^2)]$
m_{cu}	Copper Mass rotor [kg]
m_{fe}	Iron Mass stator [kg]
m^s_{cu}	Copper Mass stator [kg]
mmf	Magnetomotive force [AT]
M	Inertia constant [Jω^2/VA]
N	Normal/gaussian distribution [-]
ψ	Flux linkage [Wb]
ω	Angluar velocity [rad/s]
P_{mec}	Mechanical power [W]
P_{core}	Core losses [W]
P_{stray}	Stray load losses [W]
$P_{f\&w}$	Friction and windage losses [W]
P_{el}	Electrical Active Power [W]
Q	Reactive Power [VAr]
$\mathscr{R}$	Reluctance [1/H]
R	Stator winding resistance [Ω]
R_f	Field winding resistance [Ω]
τ	Mechanical torque [Nm]
θ	Phase angle between voltage and current in phase a [rad]
T^s_{cu}	Stator winding temperature [°C]
T^s_{fe}	Core temperature [°C]
T_r	Rotor temperature [°C]
T'_{d0}	d-axis transient time constant [s]
T'_{q0}	q-axis transient time constant [s]

Symbol	Explanation
U	Uniformly distribution [-]
X'_d	d-axis transient reactance [Ω]
X_d	d-axis reactance [Ω]
X'_q	quadrature axis transient reactance [Ω]
X_q	quadrature axis reactance [Ω]
X_{ad}	d-axis magnetizing reactance [Ω]

1 Introduction

Synchronous generators are an essential part of the electrical power system, mainly because of the controlled, inertia-based generation of electrical energy. Throughout the operation, the electrical power grid face changing power demand, and differences in production and demand cause the power grid frequency to vary. A low inertia power grid will be vulnerable to highly changing demand, causing frequency deviations. The inertia of the generator will cause inertia to the power grid frequency, increasing stability during changing demand. In case of severe frequency deviations, the synchronous generator cannot remain synchronous with the power grid. A loss of synchronism can cause severe damage and will, in the best-case scenario, force the generator to restart. Solar panels and wind power are selected as possible solutions to increase electrical energy production in a world with an increasing need for electricity. While these sources of energy cause increased production of energy, both solar and wind power are non-controllable, with no inertia. The low inertia cause worse frequency fluctuations, which makes the state of the remaining inertia-based synchronous generators more crucial. In addition to the influence on the grid frequency, will high-demand periods for electrical power demand a sufficient output of reactive power to ensure no collapse of the system voltage. To ensure the operation of the power grid and generator, each generator contains several governing control schemes. The control schemes control both active and reactive power production through changes to the magnetization and torque applied to the generator rotor. Hydropower utilizes hydro turbines connected to the generator shaft. The hydro turbines add a dynamic to the production of electrical power, as changes in active power cannot be controlled directly, yet, have to be controlled through the flow of water.

The operational point of the synchronous generator causes changing efficiency due to power losses being dependent on the operation. The power losses represent heat sources in the generator, causing the thermal profile of the generator to change with the losses.

Though mechanistic models of the electrical, mechanical, and thermal state of the synchronous generator and driver, can a hydropower plant be emulated as a digital twin. A digital twin emulation allows a simulation of operational conditions and will allow more dynamic generator operation with increased confidence. However, the realisticity of the emulated system highly depends on the mechanistic models and parameters. Mechanistic models are well established, while parameters depend on each individual generator and driver. Several laboratory test procedures have been established to estimate the parameters. Other methods include estimations of the parameters through known relationships.

1.1 Background

During the fall of 2021, an in-house synchronous generator test rig was installed at the University of South-Eastern Norway as part of a master project [1]. The synchronous generator is rated 2 kVA, with a DC motor as the primary runner, with static excitation of the generator. The generator allows physical laboratory tests of a synchronous generator. The generator has run manual laboratory exercises like open-circuit and short-circuits tests. During the fall of 2022, multiple sensors were installed on the generator, all combined into a data acquisition hardware, NI cDAQ -9189. In addition, software was developed for the acquisition of the sensor values as part of a master Project work. The software developed during the project was written in C#, handling configuration, measuring, soft sensor estimations, and SQL database storage. The project work also featured several laboratory sessions, from which generator parameters and power losses were estimated. Static digital test cases were also established as part of the software, allowing digital simulation of the parameter estimation laboratory sessions [2].

1.2 Motivation

The previous work on the synchronous generator test rig includes data acquisition software with static simulations and estimation of several parameters and power losses obtained through manually controlled laboratory sessions. In addition, the data acquisition hardware installed contains analog output modules, allowing control signals. The control signals can replicate the generator's governing control mechanisms during laboratory sessions. Hence eliminates the need for manual control and human error.

A thermal model is vital to increase the synchronous generator knowledge during operation. The synchronous generator consists of several parts of different sizes and stress, resulting in a non-uniform distribution of the generated heat. Through dynamic state and parameter estimation of the generator, the operational knowledge of the generator is further increased. Furthermore, adding the possibility to simulate the behaviour of the synchronous generator as a dynamic system through mechanistic models which use the estimated parameters will allow digital simulations of entire laboratory sessions, saving time, ensuring operational safety, and increasing knowledge about the synchronous generator.

1.3 Problem Statement

In an attempt to address the aforementioned challenges, was a project description made, available in Appendix A. The outlined scope of the thesis is summarized below, divided

into main and sub-objectives. The main objective of the thesis is given by (MO).

(MO) Further develop the data acquisition application.

To further specify the indistinct main objective, are several sub-objectives ((O1)-(O8), specified accordingly.

(O1) Survey digital twin of hydropower modeling and control systems.

(O2) The software should be developed to control the speed controller, and an AVR for voltage regulation should be implemented. In addition, if time allows, tune controllers towards IEEE and Norwegian standards and implement simple overexcitation and stator current limiters. (OXL/SCL)

(O3) A simple electrical model of the generator, e.g., a third-order model and a lumped parameter thermal model from [3], should be implemented in LabView.

(O4) Implement an already developed loss model of the synchronous machine.

(O5) Controllers should be tested on the generator lab setup, with control through the Compact DAQ.

(O6) Collect a sufficient amount of data from the generator through test runs to estimate the model parameters of the lab generator for both the thermal and electrical models. In addition, if time allows, expand data collection to an external study case

(O7) Implement a Kalman filter for real-time state estimation of the synchronous generator states and variables and do proper verification tests of the filters.

(O8) The work should be compiled into a paper manuscript for further publication.

1.4 Method and structure

The thesis project will utilize literature on hydropower plants and synchronous generators as well as thermodynamics to conduct the research. The theoretical approaches will be tested on measurements from the physical test rig at USN and through simulations. The physical laboratory situated on the campus of USN will be used to carry out laboratory experiments, using the previously installed sensors together with a Labview application which will be created during the work, as mentioned in Section 1.3. The LabView application will use the previously made SQL database as cloud storage. A summary of the libraries with usage areas is listed below.

- Python version 3.8, with Libraries; Pandas for data frame utilization, Numpy for numerical computations, PyMc3 for Bayesian Inference, matplotlib for plotting, sklearn for statistic measures.

- LabVIEW with modules; Database connectivity, DAQmx, Control design and simulation module.
- NI MAX for verification of DAQ measurements and control.
- Overleaf for writing in LaTex.
- Microsoft Visio for diagrams
- Microsoft Excel for Gannt diagram
- Microsoft Azure SQL database

Including the current chapter, the report consists of six main chapters. The current chapter aims to introduce the thesis with an introduction, a brief background overview and a presentation of the problem statements. The next chapter will present the theoretical background needed to address solutions to the problem statements. First, the survey will look into the main concerns regarding the hydraulic part of the hydropower plant without focusing on the findings. Next, the central controller schemes relevant to hydropower will be presented. The survey will then focus on the electrical model of the generator, focusing on the salient pole synchronous generator and the two-reaction theory. The operational losses of the generator will then be presented. At last will, the thermal phenomena created by the power losses will be presented to conclude the survey. Next, chosen parameter and state estimation techniques will be presented and measures to validate obtained results. Next, a methodology chapter will present the presented theory's setup and implementation. Then, will the obtained results be presented in a result chapter, separated into three study cases. At last, the results will be discussed before a conclusion will be made, and future work will be proposed.

Throughout the report, the main chapters will be divided into subchapters, focusing on a more specific subject of the thesis. A general separation throughout the report is between the thermal and electrical parameter estimations. However, these are combined in the making of the digital twin. To increase the readability of the report, some results and data of interest are stored in Appendix B.

2 Theory

In order to address the technical challenges presented throughout the Objectives (01)-(O8) requires some general theory about the hydropower plant with a focus on the synchronous generator. This chapter will present the general theory, starting with a survey on Digital Twin for hydropower modelling, and later moving to the electromechanical aspects of the synchronous generator. From there will, the power losses and the thermodynamics relevant to the synchronous generator be presented. At last, will parameter and state estimation theory be presented together with relevant validation measures.

2.1 Digital twin for hydropower modeling

This chapter will present the general basis needed for establishing a digital twin for hydro power plant modelling, through a survey. At first, will relevant digital twin technology be presented, and later will, relevant hydropower plant theory be presented.

2.1.1 Digital Twin

Digital twin technology is a virtual representation of a physical system driven by mechanical or mathematical models of the system [4]. In addition, the physical system to be created as a digital twin is often equipped with sensors, gathering data to strengthen the similarity between the digital twin and the physical system [4]. Table 2.1 presents the different types of digital twin technology.

Table 2.1: Types of Digital twins [4].

Type	Name	Scope
T1	Component twin/Parts twin	Basic units and small parts
T2	Asset twin	Several components
T3	System or Unit twins	Several asset twins
T4	Process twins	Several system twins

At the lowest level is the component and parts twin; when combined, they form an asset twin, which can be used to study the interaction between the components. Combining

assets forms a system/unit twin, which forms a functioning system, forming valuable insight into the interaction between the assets. At the highest level, the Process twin reveals how system and unit twins work together in a process [4]. The direct use of digital twins is typically divided into three sections, as presented in Table 2.2 [5].

Table 2.2: Sections of digital twin technology[4]

Type	Section	Usage area
S1	Product	Simulation of product behavior in different conditions
S2	Production	Production and manufacturing
S3	Performance	Digital twin technology used to analyze and optimize operational states

When including physical components in the twin, will the digital twin be considered hardware in the loop simulation, and not a fully digital twin, a process typically used when the behaviour of the physical component is difficult to describe using mechanistic models [6].

2.1.2 Hydropower plant

The hydropower plant operates by converting kinetic energy water into electrical power. It is done through an interconnected turbine and synchronous generator. This Section will give an overview of the hydropower plant, while the specific working of the synchronous generator will be presented in section 2.2. A simplified version of the hydropower plant is shown in Figure 2.1.

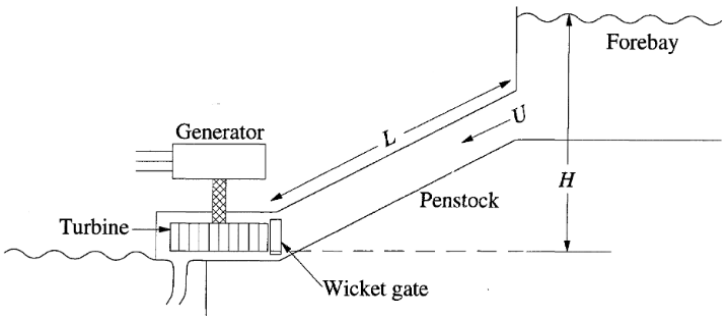

Figure 2.1: Simplified overview of a hydropower plant [7].

As seen in Figure 2.1, does the water flow represent kinetic energy applying torque to the turbine, causing shaft rotation. The amount of nominal active power of a hydropower plant generator is given by Equation 2.1 [8].

$$P_n = g\rho Q_n H_n \tag{2.1}$$

Where g is the gravitational acceleration, ρ is the density of the water, Q_n is the nominal volumetric flow, and H_n is the available height difference from the reservoir to the turbine, with losses considered. The losses are caused by friction and changing dimensions/pressure. The volumetric flow and available height difference depend on the geometric placement of the hydropower plant, as the waterway varies with nature's natural geometrical shape. The two main usage areas which are typically used for the location of a hydropower plant are listed below;

- River
- Damn/Reservoir

The river type represents uncontrolled water flow which will vary with seasonal changes. The damn/reservoir type does provide control of water flow, while the seasonal influx changes will still change the height of the reservoir, altering the nominal active power. The seasonal changes alter the operational state of the hydropower plant; as a result, are several turbine types provided to maximize the efficiency of the hydropower plant throughout its lifetime. There are two main typologies of hydropower turbines, either reaction or impulse. The reaction type uses the general flow of water for rotating the turbine, while the impulse type uses the impulse hit of water into the turbine. The most common turbine types and their topology are given in Table 2.3.

Table 2.3: Turbine types [8]

Name	Type
Francis	Reaction and impulse
Kaplan	Impulse
Pelton	Reaction

Given the different types, the efficiency characteristic for each of the turbine types is presented in Figure 2.2.

The differences in efficiency characteristics make the different turbines attractive in specific usage areas. The Pelton turbine does have increased control through multiple injectors. Hence the efficiency will be higher at a lower load ratio. The efficiency of the turbine is not considered in this thesis.

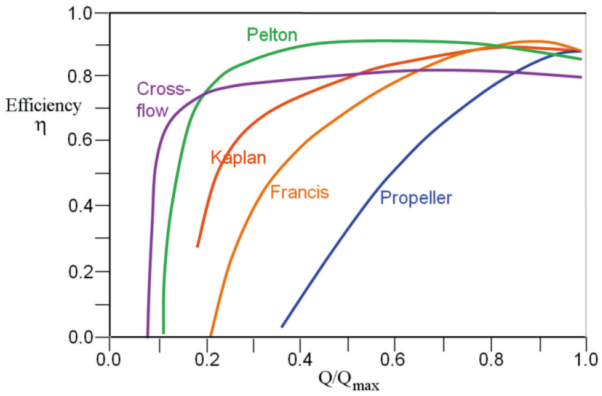

Figure 2.2: Efficiency characteristics for the different turbines [9].

2.1.3 Hydro Power Control Systems

The synchronous generator depends on control systems in order to maintain compliance with standards and regulations and to maintain production. The controlled parameters of the hydropower plant consist of water flow and field excitation, controlling respectively active and reactive power. The common control systems that handle control of the active and reactive power are the governor and automatic voltage regulator (AVR), respectively [10].

Governor control

The main objective of the governor control scheme is to maintain close to nominal grid frequency. The power grid frequency is a global phenomenon, meaning that all production and load contribute to changes in the frequency. The changes in frequency are caused by the differences between the production and demand of active power, hence will control of the active power control the contribution to the remaining nominal grid frequency. Figure 2.3 shows a graphical overview of the process [10].

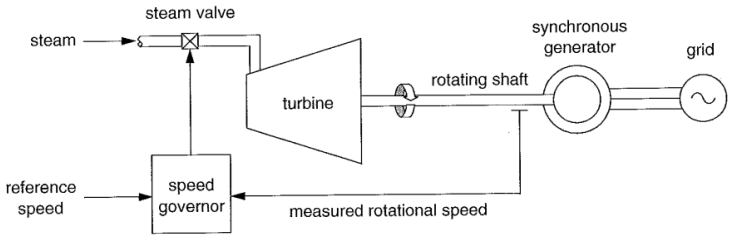

Figure 2.3: Overview of the governor control for a steam turbine [10].

The process presented in Figure 2.3 is the same for a hydropower plant. The governor controls the gate valve, which controls the amount of applied torque through the water flow

The power grid consists of many sources of generation. Direct control of the active power would cause an unstable grid, as all generators would try to restore the frequency, resulting in an overshooting reaction in the generation. To overcome this issue, the governor controls are equipped with droop control. The droop control acts as a fixed ratio between frequency deviation and power production deviation from the setpoint, as presented in Figure 2.4 [10].

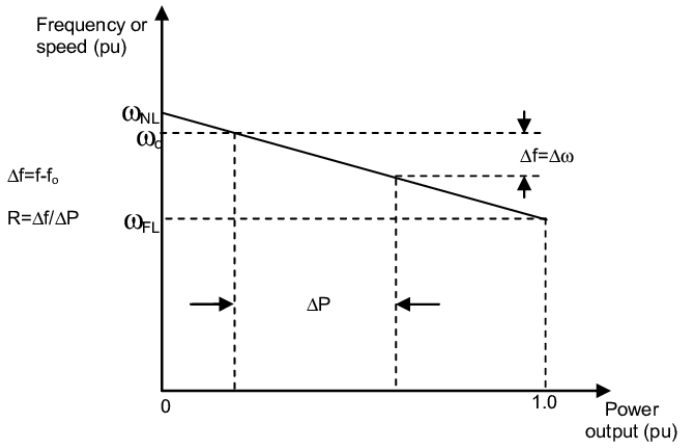

Figure 2.4: Governor control [11].

The slope of the governor curve in Figure 2.4 is known as the droop. The droop decides how the production of active power changes with the frequency changes, given by Equation 2.2 [10].

$$R = -\frac{\Delta f / f_n}{\Delta P / P_n} \tag{2.2}$$

Where R is the droop, Δf is the deviation in frequency, f_n is the nominal frequency, ΔP is the active power deviation from the original setpoint, and P_n is the rated power of the generator. Equation 2.3 gives the resulting change in active power production from a frequency deviation.

$$\Delta P = -\frac{\Delta f P_n}{R f_n} \tag{2.3}$$

As seen from Equation 2.3, will a low droop will result in a great change in active power production, while a higher droop will restrict the change in active power production. The change in grid frequency versus active power is known as the network power frequency characteristic, given by Equation 2.4.

$$\lambda = -\frac{\Delta P}{\Delta f} \tag{2.4}$$

Transient droop

The governor droop regulates the amount of active power production by opening of the gate valve, which ultimately controls the load ratio of the hydropower plant. When subject to changes in the gate valve, does the water flow respond peculiarly [7] [12]. Hence, a slowdown of the initial gate valve motion is needed to stabilize the water flow. The slowdown is accomplished with a transient droop feedback loop as shown in Figure 2.5 [12].

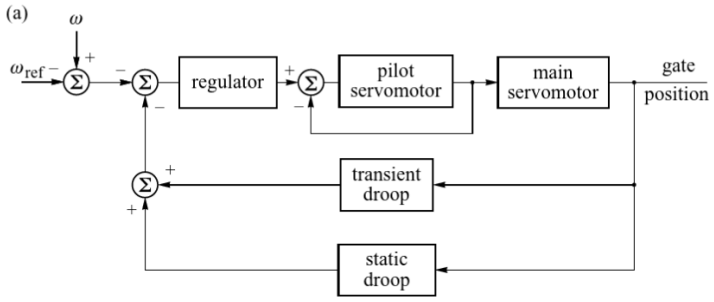

Figure 2.5: Transient and static droop control loops [12]

The transient droop reduces the transient gain of the governor droop, allowing water in the penstock to respond to the changes in the gate valve position [12].

Automatic voltage regulator

The voltage level is a local phenomenon in the power grid, in opposition to the system frequency [10]. Changes in voltage level at the generator terminals compared to the infinite bus will change the amount of reactive power produced/absorbed. A lower voltage level at the terminals of the generator causes the synchronous generator to absorb reactive power. During high demand for active power, the voltage relies on an increased supply of reactive power [13]. The main task of the automatic voltage regulator is to control the terminal voltage of the synchronous generator, done by adjusting the field voltage. A more specific reaction of the terminal voltage from changes in the field voltage will be presented in Section 2.2. The overview of the AVR process is shown in Figure 2.6.

The voltage regulator in Figure 2.6 consists of control schemes, as presented in Figure 2.7. The resulting output from the regulator gets fed into the exciter, which applies the excitation voltage to the field. Chapter 2.2 will show that the terminal voltage depends on the field current as well as the angular velocity of the rotor, hence does also the rotor angle depend on the excitation current. Hence, are a power system stabilizer implemented to make the AVR dynamically able to contribute to the stability and decaying of low-frequency oscillations, LFO [14]. A common voltage regulator control scheme is presented in Figure 2.7.

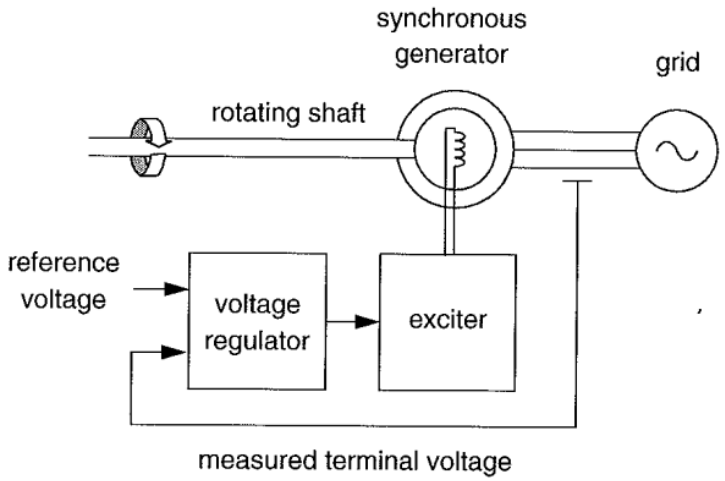

Figure 2.6: Simplified overview of the AVR [10].

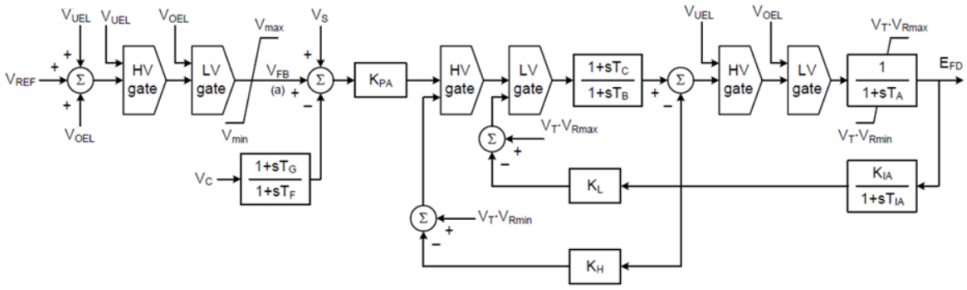

Figure 2.7: Control scheme ST7C [15].

2.2 The synchronous machine

The synchronous machine can be divided into two topologies, the synchronous generator and the synchronous motor, depending on whether the machine supplies or absorbs electric power. The theory presented in this section applies to both topologies, just contrary, yet, the thesis will focus on the generator topology.

2.2.1 The electrical model

This chapter will establish a general mathematical model of the electrical parts of the synchronous generator. The chapter builds on the general mathematical model presented in Machowski [12] with the adoption of the changed orientation of the directional and quadrature axes, the same orientation as used in Kundur [7].

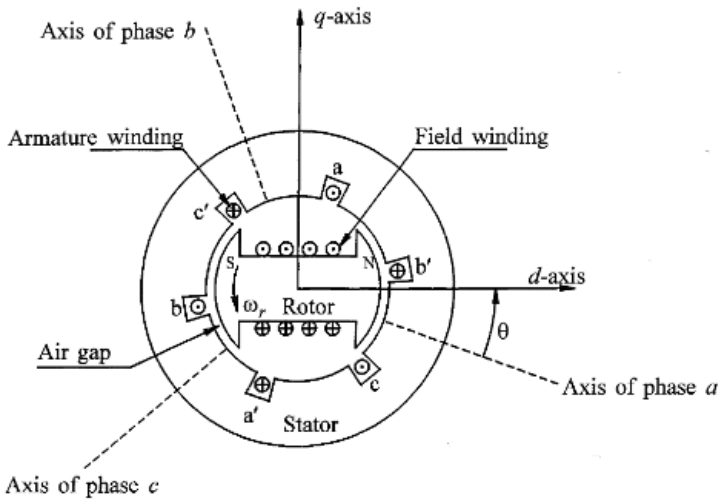

Figure 2.8: Simplified salient pole synchronous generator overview [7].

A simplified overview of the synchronous generator is presented in Figure 2.8. During operation, the rotor field winding drives the field flux ϕ, controlled by the excitation, producing an mmf wave through the air gap at steady angular velocity resulting in a sinusoidal waveform for each pole. The mmf is given by Equation 2.5 [12].

$$F_f = N_f i_f \tag{2.5}$$

The shape of the rotor can be round, called round-rotor machine, or salient, called salient pole machine, which is the case for the generator presented in Figure 2.8. The salient pole geometric shape causes lower magnetic reluctance in the d-axis compared to the q-axis, as seen in Figure 2.9 [12].

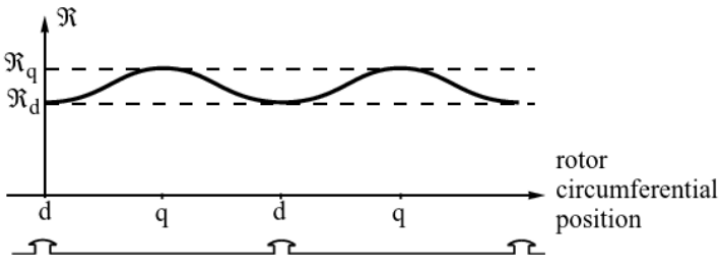

Figure 2.9: Reluctance in d- and q-axis [12].

The reluctance, $\mathscr{R}$, has a direct impact on the excitation flux per pole ϕ_f driven by the field mmf, given by Equation 2.6 [12].

$$\phi_f = \frac{F_f}{\mathscr{R}} \tag{2.6}$$

For a round rotor machine, does this cause coincides with the peak of the field flux and the field mmf. The mmf cause a time-varying flux linkage, ψ, with each of the armature phases, phase A given by Equation 2.7 [12].

$$\psi_{fA} = N_\phi \phi_f \cos \omega t = N_\phi \frac{F_f}{\mathscr{R}} \cos \omega t = M_f i_f \cos \omega t \tag{2.7}$$

Where M_f is the mutual inductance between the field and armature winding. Referenced to Faradays Law, does the time-varying flux linkages induces an internal voltage in the stator windings, given by Equation 2.8 [12].

$$e_{fA} = -\frac{N_\phi \phi_f}{dt} \cos \omega t = \omega M_f i_f \sin \omega t \tag{2.8}$$

In a salient pole machine, the difference in the air gap between the directional and quadrature axes results in a non-uniform air gap flux. The shape of the rotor causes the maximum flux linkage value at the directional axis and the minimum value at the quadrature axis. To handle the non-uniform flux, A. Blondel developed a two-reaction theory, resolving the mmf acting along the directional- and quadrature- axes, causing constant values of reactances to the mmfs, considered separately [12]. The total mmf will then be given by the Equation 2.9 [12].

$$\vec{F}_r = \vec{F}_d + \vec{F}_q \tag{2.9}$$

Where the directional axes are the sum of the excitation mmf and the directional axes mmf $\vec{F}_d = F_f + F_{ad}$, there is no excitation winding in the quadrature axis; hence, $\vec{F}_q = \vec{F}_{aq}$. $\vec{F}_{ad}$

and $\vec{F}_{aq}$ are the armature directional and quadrature axis mmfs. As seen from Equation 2.7, does the resulting induced internal voltage, emf, lag their respective mmf by 90 degrees, causing E_q to be induced by the d axis mmf, and E_d to be induced by $-\vec{F}_q$, assuming q leads d axis by 90 degrees as in Figure 2.8 [12] [7]. The generator circuits can be seen as several electrical circuits connected through mutual coupling. Each of the circuits has its resistance and inductance. The general generator contains three terminal windings, rotor winding, and damper windings on the rotor, shown in Figure 2.10 [12].

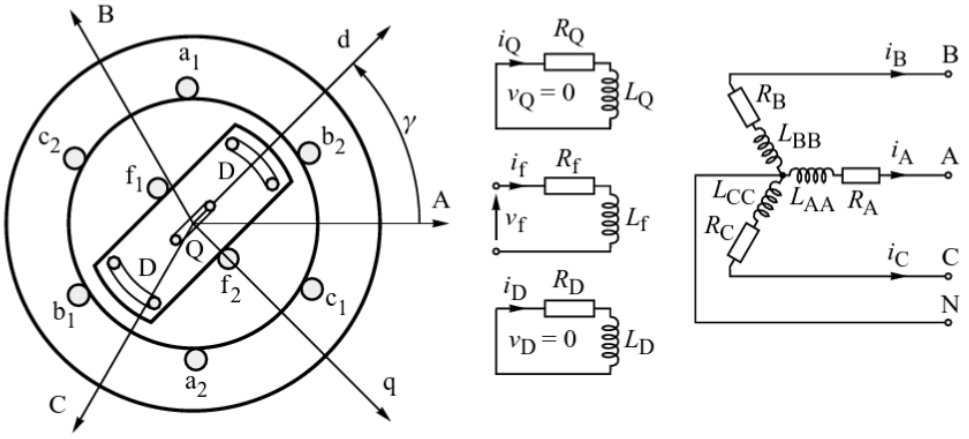

Figure 2.10: Simplified generator topoligy circuits [12]. (Alignment of the d and q axis are not the same as used in this thesis.)

Each of these windings has been modelled such as the flux in each winding depends on the currents in all the other windings, given by Equation 2.10 [12].

$$\begin{bmatrix} \psi_A \\ \psi_B \\ \psi_C \\ \psi_f \\ \psi_D \\ \psi_Q \end{bmatrix} = \begin{bmatrix} L_{AA} & L_{AB} & L_{AC} & L_{Af} & L_{AD} & L_{AQ} \\ L_{BA} & L_{BB} & L_{BC} & L_{Bf} & L_{BD} & L_{BQ} \\ L_{CA} & L_{CB} & L_{CC} & L_{Cf} & L_{CD} & L_{CQ} \\ L_{fA} & L_{fB} & L_{fC} & L_{ff} & L_{fD} & L_{fQ} \\ L_{DA} & L_{DB} & L_{DC} & L_{Df} & L_{DD} & L_{DQ} \\ L_{QA} & L_{QB} & L_{QC} & L_{Qf} & L_{QD} & L_{QQ} \end{bmatrix} \begin{bmatrix} i_A \\ i_B \\ i_C \\ i_f \\ i_D \\ i_Q \end{bmatrix} \tag{2.10}$$

The self-inductance of each of the phases is at maximum when the rotor angle is aligned with the respective winding, resulting in maximum self-inductance for phase A at the alignment of the rotor directional axis and armature windings.

$$L_{AA} = L_s + \Delta L_s \cdot \cos(\#p\delta) \tag{2.11}$$

With $\#p$ being the number of poles, and δ being the rotor angle relative to the stator phase A. The same is valid for phases B and C, shifted with -120 and +120 degrees. The self-inductance in the rotor is constant and does not vary with the rotor position. The

mutual inductances between stator phase windages are shifted by 120, hence negative, and are at a maximum when the rotor position is midway between the windings. Given by Equation 2.12 [12].

$$L_{AB} = L_{BA} = -M_s - \Delta L_s \cos(2(\delta + \frac{1}{6}\pi) \tag{2.12}$$

The mutual inductance between the stator and rotor changes with the rotor position and is at a maximum when they are aligned, as seen by Equations 2.13- 2.15.

$$L_{Af} = L_{fA} = M_f \cos(\delta) \tag{2.13}$$
$$L_{AD} = L_{DA} = M_D \cos(\delta) \tag{2.14}$$
$$L_{AQ} = L_{QA} = M_Q \cos(\delta) \tag{2.15}$$

The same is valid for phases B and C, shifted by -120 and +120 degrees. The mutual inductance in the rotor is zero, as the directional and quadrature axis are perpendicular [12].

2.2.2 Park Transformation

Equations 2.11 to 2.15 present that the majority of Equation 2.10 depends on the rotor position referenced to phase A. The rotor position are changing with time, so Equations 2.11 to 2.15 will also vary with time. Park transformation is given as a reference frame change from time to rotor angle referenced to stator phase A winding. The transformation matrix is given by Equation 2.16 [12].

$$W = \sqrt{\frac{2}{3}} \begin{bmatrix} \cos(\delta) & \cos(\delta - \frac{2}{3}\pi) & \cos(\delta + \frac{2}{3}\pi) \\ -\sin(\delta) & -\sin(\delta - \frac{2}{3}\pi) & -\sin(\delta + \frac{2}{3}\pi) \\ \frac{1}{\sqrt{2}} & \frac{1}{\sqrt{2}} & \frac{1}{\sqrt{2}} \end{bmatrix} \tag{2.16}$$

Given in compact form by Equation 2.17.

$$i_{dq0} = W \cdot i_{abc} \tag{2.17}$$

The park transformation allows a transformation from ABC to DQ0 space, given as Equation 2.18.

$$\begin{bmatrix} i_{abc} \\ i_{fDQ} \end{bmatrix} = \begin{bmatrix} W^{-1} & 0 \\ 0 & 1 \end{bmatrix} \begin{bmatrix} i_{dq0} \\ i_{fDQ} \end{bmatrix} \tag{2.18}$$

This allows the transformation of Equation 2.10, resulting in, Equation 2.19.

$$\begin{bmatrix} \psi_d \\ \psi_q \\ \psi_0 \\ \psi_f \\ \psi_D \\ \psi_Q \end{bmatrix} = \begin{bmatrix} L_d & & & kM_f & kM_D & \\ & L_q & & & & kM_q \\ & & L_0 & & & \\ kM_f & & & L_f & & \\ kM_D & & & L_{fD} & L_D & \\ & kM_Q & & & & L_Q \end{bmatrix} \begin{bmatrix} i_d \\ i_q \\ i_0 \\ i_f \\ i_D \\ i_Q \end{bmatrix} \tag{2.19}$$

Where L_d is the directional axis inductance, L_q is the quadrature axis reactance, L_{fD} is the mutual reactance between rotor d axis and damper winding in d axis, k is a constant $\sqrt{\frac{3}{2}}$ and M_f, M_D, LQ [12]. Equation 2.19 identifies three sets of magnetic couplings, each perpendicular to the others, presented by Figure 2.11 [12].

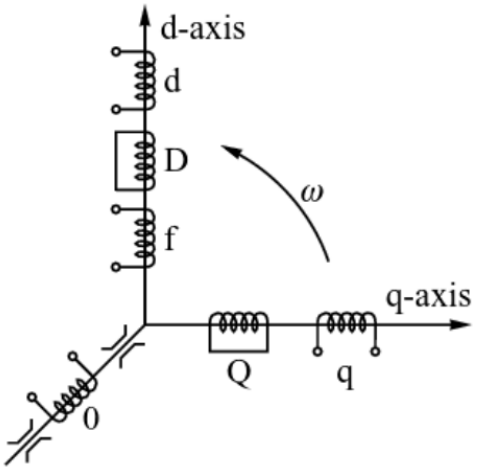

Figure 2.11: Fictious perpendicular windings [12]. (Alignment of the d and q axis are not the same as used in this thesis.)

2.2.3 Rotor angle

The rotor angle used throughout Equation 2.12-2.16 presents the rotor angle with the mmf in stator phase A as reference. During operation, the angle varies based on the rotor's angular velocity compared to the power grid's synchronous frequency, given by Equation 2.20 [12].

$$\delta = \delta_0 + \int \omega_{elec} - \omega_s dt \tag{2.20}$$

Where δ_0 is the initial rotor angle and the integral accounts for the speed differences over time, assuming both ω_s and ω_{elec} are given in the electrical radians per second. The rotor angle can also be estimated by Equation 2.21 [16] [7].

$$\delta_i = \arctan\left(\frac{P_i}{\frac{V_i^2}{X_q} + Q_i}\right) \tag{2.21}$$

Where δ_i is the rotor angle at time i, and P_i, V_i, and Q_i is the terminal quantities at time i.

2.2.4 Voltage equations

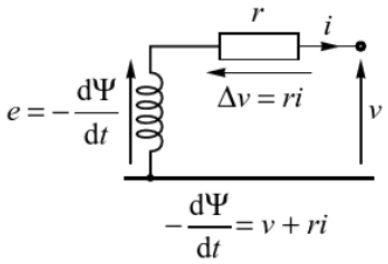

Figure 2.12: General generator circuit [12].

Figure 2.12 presents the general generator circuit, represented as an emf given by the changing flux behind a resistance. Applying the dq0 reference frame for voltage, currents, and flux linkages, together with Kirchhoff's voltage law in Figure 2.12 given the relationship given by Equation 2.22.

$$\begin{bmatrix} v_{dq0} \\ v_{fDQ} \end{bmatrix} = -\begin{bmatrix} R_{ABC} & \\ & R_{fDQ} \end{bmatrix} \begin{bmatrix} i_{dq0} \\ i_{fDQ} \end{bmatrix} - \begin{bmatrix} \dot{\psi}_{dq0} \\ \dot{\psi}_{fDQ} \end{bmatrix} + \begin{bmatrix} \Omega & \\ & 0 \end{bmatrix} \begin{bmatrix} \psi_{dq0} \\ \psi_{fDQ} \end{bmatrix} \tag{2.22}$$

With $\dot{\psi}_{dq0}$ and $\dot{\psi}_{fDQ}$ being the transformator emfs, and $\Omega\psi_{dq0}$ being present as the ems induced in the stator windings by the rotating magnetic field applied by the rotor, with the rotational emfs present, given as Equation 2.23 [12]

$$\Omega\psi_{dq0} = \begin{bmatrix} -\omega\psi_q \\ \omega\psi_d \\ 0 \end{bmatrix} \tag{2.23}$$

Equation 2.23 confirms that the directional axis emf is being induced by the quadrature axis flux linkages, and vice versa, with the being a result of the assumed rotational

direction and orientation of the axes, assumed q axis leading the d axis by 90 degrees. Assuming balanced operations would allow neglecting the zero-axis, as it cancels out. It would also allow neglection of the transformer emf as it is relatively small compared to the rotational emf given in Equation 2.23 [12]. Assuming a steady state would make the armature flux penetrate through all the circuits, making the directional and quadrature damping windings constant, hence does the armature current only see the directional- and quadrature-axis inductance L_d and L_q, this allows neglection of the damping windings [12]. These simplifications result in Equation 2.24.

$$\begin{bmatrix} v_d \\ v_q \\ -v_f \end{bmatrix} \approx - \begin{bmatrix} R & 0 & 0 \\ 0 & R & 0 \\ 0 & 0 & R_f \end{bmatrix} \begin{bmatrix} i_d \\ i_q \\ i_f \end{bmatrix} + \begin{bmatrix} -\omega\psi_q \\ \omega\psi_d \\ 0 \end{bmatrix} \tag{2.24}$$

Inserting for directional and quadrature flux linkages and combining results in the simplified Equation 2.25 of the steady-state voltage equations.

$$\begin{bmatrix} V_d \\ V_q \\ -V_f \end{bmatrix} = - \begin{bmatrix} R & -X_q & 0 \\ X_d & R & -X_{ad} \\ 0 & 0 & R_f \end{bmatrix} \begin{bmatrix} I_d \\ I_q \\ I_f \end{bmatrix} \tag{2.25}$$

Where the directional and quadrature voltages are given as Equations 2.26 and 2.27 [7].

$$V_d = V\sin(\delta) \tag{2.26}$$
$$V_q = V\cos(\delta) \tag{2.27}$$

Where V is the amplitude of the terminal voltage of the generator and δ is the rotor angle, the directional and quadrature currents referenced from the terminal current are given by Equations 2.28 and 2.29 [7].

$$I_d = I\sin(\delta + \theta) \tag{2.28}$$
$$I_q = I\cos(\delta + \theta) \tag{2.29}$$

Where I is the amplitude of the terminal current and θ is the phase angle between the terminal voltage and current.

2.2.5 Per unit system

There are two per-unit systems to consider when modelling the synchronous generator. Base values at both the rotor and stator must be assessed. The stator per unit values is

well established, given by Equations 2.30 and 2.31 [13]. -

$$I_{base} = \frac{S_{base}}{\sqrt{3}V_{base}} \tag{2.30}$$

$$Z_{base} = \frac{V_{base}^2}{S_{base}} \tag{2.31}$$

Where S_{base} and V_{base} typically are selected as the three-phase rated apparent power and line-line voltage [13]. The rotor base values are typically set by the field current, where the base field current value is the value required, in amperes, to induce a rated voltage on the armature terminals during an open circuit test, given by Equation 2.25 at open circuit, hence no current in the stator windings, resulting in Equation 2.32 [7].

$$V_q = X_{ad} I_{f_{base}} \quad |_{V_t = V_{nominal}} \tag{2.32}$$

Where the base field voltage is given by the Equation

$$V_{f_{base}} = I_{f_{base}} R_f \tag{2.33}$$

Where R_f is the field winding ohmic resistance given. This is known as the non-reciprocal per-unit system. When considering parameter estimation of parameters in Equation 2.25, is the process simplified if the rotor and stator see the same value for L_{ad}. This is achieved by converting to the reciprocal per unit system, also known as the L_{ad}-base system. The reciprocal per unit system is achieved by dividing through L_{ad}, as seen in Figure 2.13 [7].

The resulting base field current is now given by Equation 2.34.

$$i_{base} = \frac{I_{f_{base}}}{L_{ad}} \tag{2.34}$$

With the resulting base field voltage given by Equation 2.35.

$$v_{base} = V_{f_{base}} \frac{R_f}{L_{ad}} \tag{2.35}$$

Where v_{base} and i_{base} are the reciprocal per unit base values for the rotor, with $I_{f_{base}}$ and $V_{f_{base}}$ being the non-reciprocal per unit base values [7].

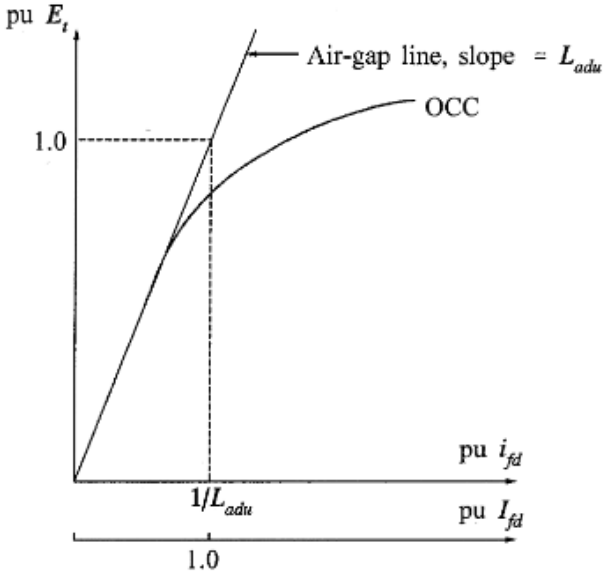

Figure 2.13: Reciprocal per units system [7].

2.2.6 Fourth order model

The general behaviour of the synchronous machine can be summarized as a set of differential and algebraic equations, with the order of the model depending on the degree of considered transient reactance, with the direct and quadrature axis voltage being viewed as an emf behind transient reactances and resistances, given by Equation 2.36 [12].

$$\begin{bmatrix} V_d \\ V_q \end{bmatrix} = \begin{bmatrix} E'_d \\ E'_q \end{bmatrix} - \begin{bmatrix} R & -X'_q \\ X'_d & R \end{bmatrix} \cdot \begin{bmatrix} I_d \\ I_q \end{bmatrix} \tag{2.36}$$

The overall model of the synchronous generator can be presented with models of different orders, depending on the considered depth of transient reactions given by Equations 2.37-2.40 [12].

$$M\Delta\dot{\omega} = P_m - P_e - D\Delta\omega \tag{2.37}$$
$$\dot{\delta} = \omega - \omega_s \tag{2.38}$$
$$T'_{d0}\dot{E}'_q = E_f - E'_q - Id(X_d - X'_d) \tag{2.39}$$
$$T'_{q0}\dot{E}'_d = -E'_d + Iq(X_q - X'_q) \tag{2.40}$$

Where E_f represents the induced voltage, given by Equation 2.41 [12].

$$E_f = \omega L_{ad} \cdot I_f = X_{ad} \cdot \frac{V_f}{R_f} \tag{2.41}$$

The electrical power supplied through the air gap is given by Equation 2.42 [12].

$$P_e = E'_q I_q + E'_d I_d + (X'_d - X'_q) I_d I_q \tag{2.42}$$

2.3 Power losses

Chapter 2.2 presented that the synchronous generator consists of an electromagnetic phenomenon, many of which depend on the rotor's angular velocity, implying mechanical movement. As a result, all parts will contribute to losses, compromising the generator's efficiency and lowering the electrical power output from the applied mechanical power. These losses will be addressed throughout this section.

2.3.1 Electrical power losses

The electrical power losses, called ohmic power losses, result from the voltage drop throughout the electric circuit. The losses are given by 2.43 [13].

$$P_{electical} = RI^2 \tag{2.43}$$

Where R is the resistance in the conducting material, given by Equation 2.44.

$$R = \frac{\rho_{T_0} \cdot l}{A_{cs}} (1 + \alpha (T_w - T_0)) \tag{2.44}$$

Where T_w is the actual temperature, T_0 is the temperature at the specified resistivity of the material, often room temperature, $\sim 20\ ^\circ$, and α is the temperature coefficient giving the change in resistance of the material pr. Kelvin increase in temperature. Hence, assuming a positive α, results in increased resistance proportionally with the increase in temperature. Hence, the ohmic losses will increase proportionally with the medium's temperature. The armature conductors are subject to an alternating current. The alternating currents represent changing magnetic fields, as presented in Section 2.2. These magnetic fields will induce currents, called eddy currents, in conductive materials, and also in the main conductor. Lenz's law gives that the induced currents will be induced such that their magnetic field will oppose the main magnetic field. This causes the current density through the conductor to be non-uniform, with the highest density in the periphery. The phenomenon is called the skin effect, and the density depth is given by Equation 2.45 [7].

$$\delta = \sqrt{\frac{2\rho}{\omega\mu}} \tag{2.45}$$

Where ρ is the resistivity of the medium and μ is the permeability of the medium. ω is the angular velocity in electrical rad/s. Seen by equation 2.44 will an increased cross-sectional area of the conductor lower the resistance, hence lowering the ohmic losses given by Equation 2.43. At higher current levels, will this be important, in a synchronous generator, will an increased cross-sectional area of the conductors lead to less space for windings, hence will the induced emf in the phases be lowered. The increased cross-sectional areas increase the effect on the skin effect. The ohmic losses in the synchronous generator are present in both the rotor and the armature windings, given by Equations 2.46 and Equation 2.47.

$$P_r = R_r I^2 \tag{2.46}$$
$$P_a = R_a I^2 \tag{2.47}$$

2.3.2 Mechanical power losses

The high angular velocity causes considerable losses from friction from the bearings as well as air drag. The nominal friction losses are given by the mechanical power required to keep synchronous angular velocity without excitation of the field windings. The losses are called friction, and windage losses, with the nominal losses given in Equation 2.48 [17].

$$P_{f\&w} = P_m = \tau \cdot \omega \qquad |_{\omega=\omega_s} \tag{2.48}$$

Where τ is the applied torque and ω is the angular mechanical velocity, given in rad/s, with ω_s representing the synchronous mechanical velocity. The synchronous angular velocity of the generator depends on the system grid frequency and the number of pole pairs on the generator, given by Equation 2.49.

$$n = \frac{60 \cdot f}{\#p} \tag{2.49}$$

Where n is the synchronous angular velocity given in RPM, f is the system grid frequency given in Hz, and $\#p$ is the number of pole pairs [13].

2.3.3 Iron power losses

The varying magnetic field created by the mmf in the generator's core will experience losses due to work done by altering the directional orientation of the ferromagnetic structure in the material. Altering the directional orientation will introduce a Power loss due to eddy currents induced in conductive material close to the conductors and core hysteresis. The nominal core losses are given by the mechanical power applied at synchronous angular velocity at a magnetization that gives nominal Voltage levels induced in the armature windings. Given by Equation 2.50 [17].

$$P_{core} = \tau\omega - P_{f\&w} \qquad |_{\omega=\omega_s} \tag{2.50}$$

2.3.4 Stray load losses

The losses presented thus far have been subject to a more or less specified location in the generator. At the loading of the generator, there will still be some losses that are not accounted for, known as the stray load losses. The stray load losses represent induced eddy currents in conductive materials near the generator. The losses are difficult to assign a specific location, hence difficult to measure directly. The nominal losses are measured by measuring the applied torque of the generator shaft at rated loading and subtracting the delivered active power and known losses, given by Equation 2.51 [17].

$$P_{stray} = \tau\omega - P_e - 3 \cdot P_a - P_{core} - P_{f\&w} \qquad |_{\omega=\omega_s} \tag{2.51}$$

2.3.5 Scaling losses

The presented losses all depend on the operational point of the synchronous generator. The ohmic losses in the rotor and the armature are self-scaling with changes in the currents in the rotor and phases. However, several of the losses introduced in this Section was represented as nominal losses, due to the difficulty of measuring them directly. Therefore, the nominal losses are given at the nominal load of the synchronous generator, scaling with the point of operation. The scaling of the nominal losses is given in Equations 2.52-2.54 [18].

$$P_{f\&w} = P^*_{f\&w} \cdot (\frac{\omega}{\omega_s}) \tag{2.52}$$

$$P_{core} = P^*_{core} \cdot (\frac{V}{V^*})^2 \tag{2.53}$$

$$P_{stray} = P^*_{stray} \cdot (\frac{I}{I^*})^2 \tag{2.54}$$

2.3.6 Total power losses

The Summarized losses of the generator are combined in Equation 2.55 [1].

$$P_{loss} = P_{f\&w} + 3 \cdot P_a + P_{core} + P_{stray} + P_r \tag{2.55}$$

With the total efficiency of the generator, given by Equation 2.56.

$$\eta = \frac{P_{out}}{P_{in}} = \frac{P_{in} - P_{loss}}{P_{in}} \tag{2.56}$$

2.4 Thermal model

This section will present the basis for establishing a thermal model of the synchronous generator. Starting from the heat balance, later presenting heat transfer processes and a simplified lumped capacitance thermal model.

2.4.1 Heat Balance

The first law of thermodynamics applied to a control volume yield, *"The increase in the amount of energy stored in a control volume must equal the amount of energy that enters the control volume, minus the energy that leaves the control volume"* - [19]. The law must be valid at every instant of time. Hence, all energy rates must be balanced, including the work applied inside the control volume. The resulting rate of change in energy in the control volume is given by Equation 2.57 [19].

$$\dot{P}_{st} = \dot{P}_{in} - \dot{P}_{out} + \dot{P}_g \tag{2.57}$$

Where $\dot{P}_{st}$ is the rate of stored energy in the control volume, given by Equation 2.58 [19].

[1] Hydraulic losses are not considered part of the generator losses

$$\dot{P}_{st} = m\hat{c}_p \frac{dT}{dt} \tag{2.58}$$

With m being the mass and $\hat{c}_p$ being the specific heat for the medium of the object.

$$P_{stored} = cM \frac{d\Delta T}{dt} \tag{2.59}$$

Energy can be transferred between elements through interactions of work or heat. Section 2.3 presented the work done in different parts of the synchronous generator during operation. From the instant the work is done, will it be transferred to surroundings through heat transfer or stored inside the control volume [19].

2.4.2 Heat Transfer

In case of heat differences between mediums, will there always be heat transfer, as heat transfer is thermal energy in transit due to a spatial temperature difference [19]. The heat transfer process is presented in different modes, listed below.

- Conduction
- Convection
- Radiation

Conduction

Conduction refers to heat transfer across a stationary medium. The medium may be a fluid or solid material. The dissipation of energy through conduction represents energy dissipated through solid material and is given by Fourier's law [19].

$$P_{cond} = -\lambda A_{cs} \nabla T \tag{2.60}$$

When considered in one dimension, the equation reduces to Equation 2.61 [19].

$$P_{cond} = \frac{-\lambda}{s} A_{cs} \Delta T \tag{2.61}$$

Convection

Convection refers to heat transfer between media. The process comprises two mechanisms, diffusion and a bulk motion of the fluid flow. Where diffusion is given as random molecular motion, in the case of a fluid in motion with a temperature T_a, close to a heated surface with temperature T_s, will the heat flux be given by Newton's Law of cooling, given in Equation 2.62 [19].

$$q'' = h(T_s - T_a) \tag{2.62}$$

Where h is known as the heat transfer coefficient, which depends on the geometrical shape of the surface as it depends on the conditions in the thermal buoyancy layer of the surface (Layer from surface to finite fluid flow). The heat flux q'', is given in W/A^2. Hence, the total energy transfer due to convection is given by Equation 2.63 [19].

$$P_{conv} = hA_{surf}(T_s - T_a) \tag{2.63}$$

Where A_{surf} is the surface area of the heated object. Convection can be present as free convection or forced convection, with free convection referring to flow due to buoyancy forces, such as density differences in the fluid. Forced convection refers to the fluid flow due to the presence of an external force forcing the fluid motion. The forced convection adds to the natural convection, and it will also alter the thickness of the thermal buoyancy layer as it forces a given fluid flow, hence will the forced convection increase the heat transfer coefficient [19].[2]

Radiation

The radiation process is referred to as energy emitted through radiation by matter above nonzero temperature. The radiation energy transport is due to electromagnetic waves. Released radiation emitted from an object's surface area originates from the thermal energy bounded by the surface, given an upper limit prescribed by the Stefan-Boltzmann law, given by Equation 2.64 [19].

$$P_b = \sigma T_s^4 \tag{2.64}$$

Where σ is the Stefan-Boltzmann constant and T_s is the absolute temperature. Equation 2.64 presents the radiation of a perfect radiator. Total radiation heat flux from an actual surface will be reduced by the surface's emissivity, ε, given by Equation 2.65.

$$q''_{rad} = \varepsilon f_{view} \sigma (T^4 - T_0^4) \tag{2.65}$$

[2] Assuming that the forced convection is not in the opposite direction of natural convection, or perpendicular the natural convection.

Again the radiation heat flux is given in W/A^2, and the total power heat transfer due to radiation is given by Equation 2.66 [19].

$$P_{rad} = \varepsilon f_{view} \sigma A_{surf} (T_s^4 - T_0^4) \tag{2.66}$$

A_{surf} is the object's surface area, and f_{view} is the configuration factor, depending on the temperatures of surrounding materials.

2.4.3 Total lumped capacitance heat method

The three heat transfer processes work together to validate the first law of thermodynamics, Equation 2.57 becomes,

$$\dot{P}_{st} = mV\hat{c}_p \frac{dT}{dt} = \dot{P}_{in} + \dot{P}_g - P_{cond} - P_{rad} - P_{conv} \tag{2.67}$$

Considering the object with stored energy as a lumped capacitance model assumes that the object's temperature is spatially uniform, eliminating the internal temperature gradient and making it possible to neglect the conduction process from the heat transfer, neglecting the internal thermal generation of energy in the objects. The resulting heat balance consists of power losses as the input work to the objects, with simultaneous radiation and convection transferring heat to respectively surrounding surfaces and ambient fluid. Simplifying the model further to include both convection and radiation in a total heat transfer coefficient given the simplified heat transfer, given in Equation 2.68 [19].

$$P_{diss} = hA_{surf}\Delta T \tag{2.68}$$

It should be noted that the simplified equation does use relative temperature, while radiation was originally given as a result of absolute temperatures. Applying Equation 2.57 gives the rate of change in temperature given in Equation 2.69.

$$\dot{T} = \frac{P_{in} - P_{diss}}{cM} = \frac{P_{in} - hA_{surf}\Delta T}{cM} \tag{2.69}$$

If assumed constant temperature around an object can Equation 2.69 be solved over time as Equation 2.70.

$$\Delta T = \Delta T_e \cdot (1 - e^{-\frac{t}{\tau}}) \tag{2.70}$$

Where τ is the time constant of the object, given by Equation 2.71.

$$\tau = \frac{hA_{surf}}{\hat{c}_p M} \tag{2.71}$$

It should be noted that the solution assumes constant temperatures in the surrounding fluid.

2.5 Parameter and state estimation

The process of estimating parameters or states involves the determination of parameters and states based on observations and knowledge of the background of the observation. The knowledge can be known as noise in the signals or state space models of the observed system. In the case of parameter estimation will, the methods aim to minimize the residual error between the observed and estimated value of the state, where the estimated values use a state space model of the observation with estimated parameters. In the case of state estimation, will the method also aims to minimize the residuals by using the known state-space model of the system [20].

Based on the possibility of describing the system through mathematical models, will the models developed adopt different names. If the model can describe the exact same system, the model is said to be deterministic. In the case of uncertainty in the mathematical model, will the model be able to give an estimation of where the system state is, typically within specified limits of certainty, the model is now said to be stochastic [20].

2.5.1 Kalman Filter

The Kalman Filter was presented in 1960 by Rudolf Kalman [21]. The filter was originally presented as a discrete filter for recursive estimation. When applied, the algorithm of the filter separates the stochastical model and stochastical measurement noise. During measurements from physical s, sensors, imperfections will always be present, creating uncertainty in the measurements. The order of this uncertainty will vary depending on the accuracy of the equipment and external noise. The Kalman filter takes the noise and uncertainty of the measurements of the system into account, creating an estimate of the states or the parameters. Considering a linear stochastic state space model given in Equation 2.73.

$$\dot{x} = Ax + Bw \tag{2.72}$$
$$z = Hx + v \tag{2.73}$$

Where A is the system dynamics and state transition matrix, Bw is the model disturbance. Z is the measurement vector with H being the state to measurement matrix and v being the measurement noise. As considered stochastic, the model is assumed Gaussian normally distributed, as given by Equation 2.74 [22].

$$f(x;\mu,\sigma^2) = \frac{1}{\sqrt{2\pi\sigma^2}} e^{\frac{-(x-\mu)^2}{2\sigma^2}} \tag{2.74}$$

Where σ is the standard deviation to a state, applying the Kalman filter to the state space model is divided into two steps. The first is the prediction step, which uses the system state model and the last known state to update the state estimate and uncertainty, given by Equations 2.75-2.77 [21].

$$\hat{x}_{n+1} = Ax_n \tag{2.75}$$
$$\hat{P}_{n+1} = APA^T + Q \tag{2.76}$$
$$\tag{2.77}$$

$\hat{x}$ and $\hat{P}$ indicate predicted values at state $n+1$. A is the state transition matrix from Equation 2.73 and P is the state error covariance matrix. Q is the noise covariance matrix of the state transition [21]. The final step of the Kalman filter is the estimation step, where the residual between the measured and estimated state is calculated, multiplied by the estimated Kalman gain, and the state covariance error matrix is also updated. The estimation step is given in Equations 2.78- 2.80 [21].

$$K = \hat{P}H^T(H\hat{P}H^T + R)^{-1} \tag{2.78}$$
$$x_{n+1} = \hat{x}_{n+1} + K(z - H\hat{x}) \tag{2.79}$$
$$P_{n+1} = \hat{P} - KH\hat{P} \tag{2.80}$$

K is the Kalman gain, R is the measurement covariance error.

2.5.2 Extended Kalman Filter

As mentioned, the basic Kalman filter assumes a linear stochastic Gaussian distributed model, limiting it to linear systems. The extended Kalman filter adopts a non-linear system state estimation by linearizing the system around the current state. Increasing the need for information about the system being estimated, due to the possibility of several equilibrium points in the system [7]. The state transition matrix now changes to the non-linear function, given in Equation 2.81.

$$\hat{x}_{n+1} = f_j(x_n) \tag{2.81}$$

Also, the state-to-measurement matrix will become non-linear, given by Equation 2.82.

$$z = h_j(\hat{x}) \tag{2.82}$$

The Jacobian of the state transition matrix is considered for the prediction of the next state space covariance error matrix, given in Equations 2.83 and 2.84 [21].

$$F_j = \begin{bmatrix} \frac{df_1}{dx_i} & \frac{df_1}{dx_{i+1}} & .. & \frac{df_1}{dx_n} \\ \frac{df_2}{dx_i} & \frac{df_2}{dx_{i+1}} & .. & \frac{df_2}{dx_n} \\ .. & .. & .. & .. \\ \frac{df_2}{dx_i} & \frac{df_2}{dx_{i+1}} & .. & \frac{df_2}{dx_n} \end{bmatrix} \tag{2.83}$$

$$\hat{P}_{n+1} = F_j P F_j^T + Q \tag{2.84}$$

The estimation step of the Kalman filter will use the Jacobian of the state-to-measurement matrix when calculating the Kalman gain and the nonlinear state-to-measurement matrix h_j. Otherwise, is the algorithm the same as the basic Kalman filter. The prediction step is given by Equations 2.88 [21].

$$H_j = \begin{bmatrix} \frac{dh_1}{dx_i} & \frac{dh_1}{dx_{i+1}} & .. & \frac{dh_1}{dx_n} \\ \frac{dh_2}{dx_i} & \frac{dh_2}{dx_{i+1}} & .. & \frac{dh_2}{dx_n} \\ .. & .. & .. & .. \\ \frac{dh_2}{dx_i} & \frac{dh_2}{dx_{i+1}} & .. & \frac{dh_2}{dx_n} \end{bmatrix} \tag{2.85}$$

$$K = \hat{P} H_j^T (H_j \hat{P} H_j^T + R)^{-1} \tag{2.86}$$

$$x_{n+1} = \hat{x}_{n+1} + K(z - h_j \hat{x}) \tag{2.87}$$

$$P_{n+1} = \hat{P} - K H_j \hat{P} \tag{2.88}$$

2.5.3 Bayesian Inference

Bayesian inference is a statistical approach to the estimation of parameters or states, with the benefit of including statistical certainty as well as a definite estimate as the mean probability. The Bayesian probability theory builds on propositions, either true or false statements—explained by the Bayes Theorem, Equation 2.89 [23].

$$P(A|B) = \frac{\text{Likelyhood} \cdot \text{prior}}{\text{Marginal Likelyhood}} = \frac{P(B|A) \cdot P(A)}{P(B)} \tag{2.89}$$

Where $P(A|B)$ is considered a measure of how strongly proposition B implies proposition A. $P(B|A)$ is the likelihood measure of how strongly proposition A implies proposition B,

and $P(A)$ is the prior probability distribution of A. Now considering A as a parameter and B as an observation, will Bayes theorem measure how strongly the propositional measurement, B, implies that the parameter A, value is true [23]. Considering known background information, α, Bayes Theorem gives Equation 2.90.

$$P(A|B,\alpha) = \frac{P(B|A,\alpha)}{P(B|\alpha)}P(A|\alpha) \tag{2.90}$$

Given that B consists of multiple independently distributed observations, B_i. Bayes theorem can be applied as Equation 2.91 [23].

$$P(A|B,\alpha) = \frac{P(B|A,\alpha)}{\sum_i P(B|A_i,\alpha)P(A_i|\alpha)}P(A|\alpha) \tag{2.91}$$

Where the marginal likelihood results from the marginalization rule, the likelihood proposition that B implies proposition A is given as independent random variables, given by Equation 2.92 [23].

$$P(B|A,\alpha) = \prod_i P(B_i|A,\alpha) \tag{2.92}$$

The prior distribution, $P(A|\alpha)$, measures how strongly proposition A, implies the background information α prior to observation B. To apply the method to a state space model, functional estimation of A is considered, given the observations b as a function of x. The resulting distribution is obtained by Equation 2.93.

$$P(A|b,x,\alpha) = \frac{P(b|x,A,\alpha)}{P(b|x,\alpha)}P(A|x,\alpha) \tag{2.93}$$

The likelihood, $P(b|x,A,\alpha)$, is now derived from the full likelihood given by Equation 2.94 [23].

$$P(b|x,A,\sigma,f,\alpha) \tag{2.94}$$

Where σ is the unknown variance of the data [23].

2.5.4 Goodness of fit

There are several statistical measures to determine the goodness of fit for regression models and other estimations and observations. The goodness of fit measures included for validating the estimations done in this thesis is listed with a description in table 2.4.

Table 2.4: Goodness of fit measures [24].

Measure	Description
R^2	A measure from 0-1 how much the deviations of the observation can be explained by the deviations in the estimated data.
MSE	Measures the variance of the residuals, the mean difference between the squared observations, and estimations.
RMSE	Measures the standard deviation of the residuals result in the same unit as the data

3 Methodology

The process from theory to results must undergo a methodical process in order to address the technical objectives given to the thesis, these will be presented in this chapter, divided into their respective section. Starting with presenting practical information about the setup, proceeding with presenting an overview of the data acquisition application and the processes of the digital twin. At last, will the relevant electrical and thermal theory be used to build models to enable parameter estimation in both areas.

3.1 Setup

As mentioned in Section 1.1, the setup in the laboratory at USN Porsgrunn consists of a DC motor connected as a prime mover to the shaft of a 2 KVA synchronous generator. The excitation system is a static exciter. The setup is presented in Figure 3.1.

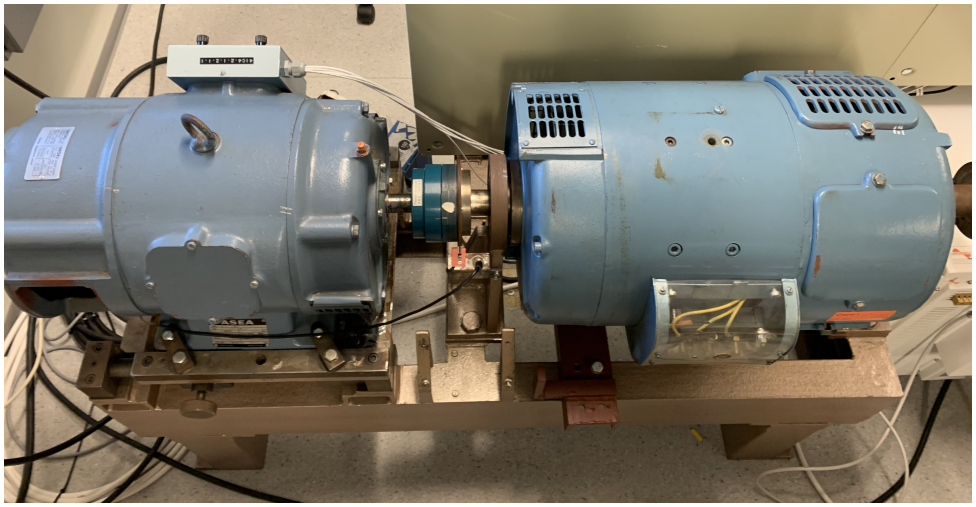

Figure 3.1: Synchronous generator and DC motor at the laboratory of USN

The national instrument modules installed on the setup are presented in Table 3.1.

The available sensors installed on the test rig are presented in Figure 3.2. With three-phase voltages and currents from the terminal, together with temperature measurements

Table 3.1: Sensors with specifications and placement, *=Aggeregate between channels [2].

Sensor Module	Analog in/out	Limit	Unit	Sampling range [kS/s]	Number of Channels
NI-9225	Analog in	±300	V	1.613-50 k	3
NI-9246	Analog in	± 20	A	1.613-50 k	3
NI-9216	Analog in	0-400	Ω	1-400*	8
NI-9207	Analog in	±10 [V] and ±20 [mA]	V/mA	1-500*	16
NI-9263	Analog out	± 10	V	100 k	4

from the room, core and phase windings. The remaining measurements are a torque sensor situated at the bearings of the DC motor, as well as field voltage and current. The control signals consist of field voltage and currents, as well as control signals to speed and torque signals to the DC motor.

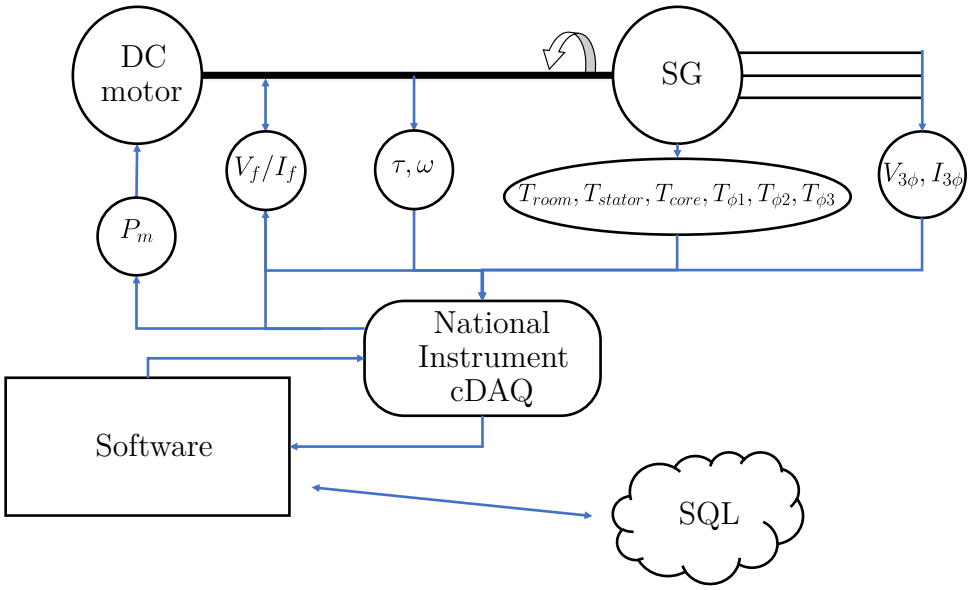

Figure 3.2: Sensors installed at test-rig.

The known parameters for the synchronous generator are presented in Table 3.2. The nominal losses of the test rig were previously estimated [2], yet, they were estimated during the thesis work, presented in Appendix C, as part of the recalibration of the force sensor used to estimate applied mechanical torque to the shaft of the setup. the nominal losses of the setup are given in Table 3.3.

Table 3.2: Known parameters of the Synchronous Generator

Parameter	Value	Unit	Description
R	0.804	Ω	Armature resistance in each phase
X_d	26.2	Ω	d-axis reactance
R_f*	39.2	Ω	Rotor resistance
V_{nLL}	230	V	Nominal Voltage
I_n	5.02	A	Nominal Current at rated load
S_n	2	kVA	Nominal apparent power
P_n	1.6	kW	Nominal active power
Q_n	1.2	kVAr	Nominal reactive power
$\cos\phi$	0.8 (lagging)	-	Powerfactor
M_r	24	kg	Total mass of rotor
M_s	44	kg	Total mass of armature
$I_{f_{base}}$	0.88	A	Field current needed for nominal voltage during open circuit test.
$V_{f_{base}}$	34.9	V	Field voltage at nominal voltage during open circuit test

Table 3.3: Nominal losses of the Synchronous Generator

Loss	Value	Unit
$P_{f\&w}$	170	W
P_{core}	113.2	W
P_{stray}	90	W

3.2 Data acquisition application

This chapter will present the application that was made as part of the thesis work. Focusing on the transition of the application onto LabVIEW, and the significant changes that were made, an overall process flow diagram for the software will be presented, as well as a process flow diagram for the measurement state of the software.

3.2.1 Labview

The application was adopted onto a Labview application as part of the thesis work. The application was implemented as a state machine, with inspiration from Halvorsen [25]. The application consists of the following states;

- Initialization

- Configuration
- Measurement
- Digital Twin

Where the initialization consists of resetting the application's graphical user interface and establishing whether the application is connected to the database. In between states is the software sent to a waiting state, where it will act on input from the user, either configuration of database parameters or transitions to another state. The measurement and digital twin states are recurring states, while the others run once before the software is sent to the waiting state. The overall state transitions are presented in Figure 3.3.

Figure 3.3: Flowchart for the overall application states

As seen from Figure 3.3, the software behaves differently, depending on whether there is a connection to the database. In case of no connection to the database, does the software save queries, measurement files and configurations on the computer. These can then be uploaded to the database at a later point. If the software is connected to the database, will configurations, and other queries with info be sent to the database upon change. After a measurement session, can the measurements be uploaded or stored locally, and

then be uploaded at a later occasion. The flowchart for the measurement state, from reading measurement data to sending control signals, is presented in Figure 3.4.

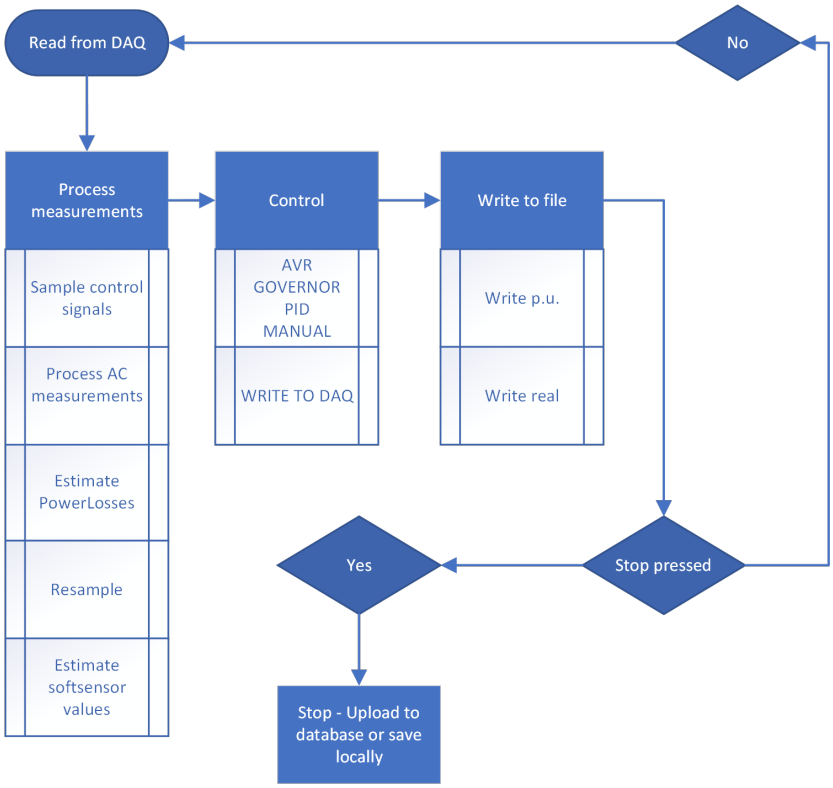

Figure 3.4: Flowchart for the measurement and control process

The measurement process starts upon measuring values from the cDAQ device. The measurements are then resampled, where frequency, phase and amplitude measurements are done for alternating current signals. Soft sensor values are also estimated, as well as common generator values, such as active and reactive power, rpm of the shaft, power factor and power losses, according to Chapter 2.3. The software then estimates and sends control signals. The control signal is estimated based on the control method, which can vary from direct signals to AVR, governor or PID-controlled signals.

3.2.2 Digital Twin

The digital twin of the synchronous generator was implemented based on the fourth-order model of the synchronous generator, presented in Chapter 2.2.6, together with the loss model presented in Section 2.3, the loss model makes the basis for the heat generation in the synchronous generator, which is represented by the thermal model from Section 2.4. The overall process is presented in Figure 3.5.

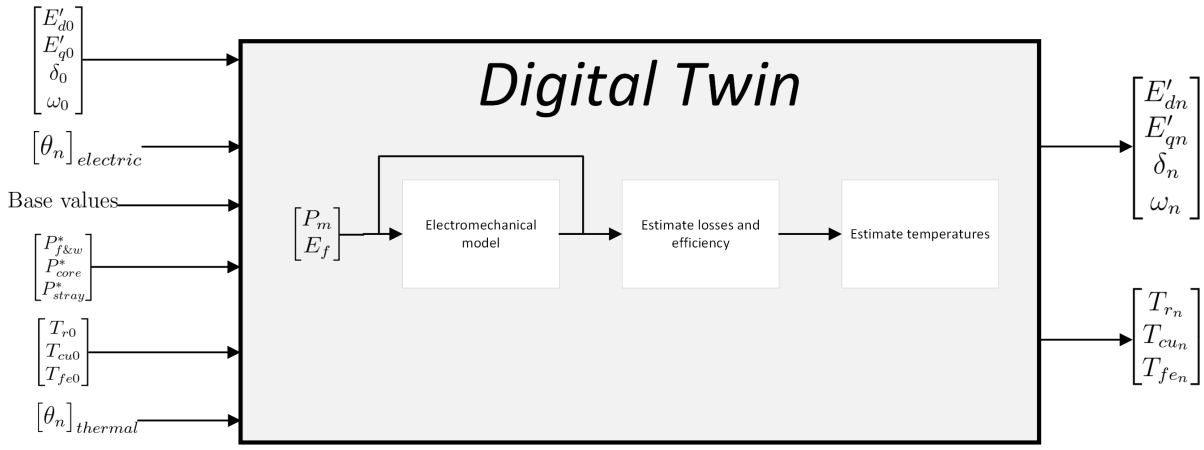

Figure 3.5: Digital Twin process

3.3 Electrical parameter estimation

Chapter 2.2 presented that the topology of the electromagnetic phenomena in the synchronous generator is different in the steady state compared to transient operation, due to the penetration depth of the armature flux linkage. In transient operation, will the penetration depth of the flux linkage not fully penetrate the damper windings, hence allowing damping winding currents and transient reactances. In the steady state, on the other hand, will, the armature flux linkage fully penetrates the damping windings, and allow some assumptions which result in the simplified voltage equations, given by Equation 2.24.

3.3.1 Steady state parameter estimation

Considering the simplified voltage equations at steady-state as a linear stochastic state space model gives the state space model in Equation 3.2

$$\begin{bmatrix} I_d \\ I_q \\ I_f \end{bmatrix}_{n+1} = A \begin{bmatrix} I_d \\ I_q \\ I_f \end{bmatrix}_n + Bw \tag{3.1}$$

$$\begin{bmatrix} V_d \\ V_q \\ -V_f \end{bmatrix}_{n+1} = - \begin{bmatrix} R & -X_q & 0 \\ X_d & R & X_{ad} \\ 0 & 0 & R_f \end{bmatrix} \begin{bmatrix} I_d \\ I_q \\ I_f \end{bmatrix}_{n+1} + Gv \tag{3.2}$$

Where $A = 1$

Kalman Filter KF- Parameter estimation of parameters of synchronous generator

Considering the 3.2, with the parameters as states, allow estimation of the parameter values through a Kalman filter, with voltages as measurements, with currents building the state to measurement matrix, results in Equation 3.4.

$$\begin{bmatrix} R \\ X_q \\ X_d \\ X_{ad} \\ R_f \end{bmatrix}_{n+1} = A \begin{bmatrix} R \\ X_q \\ X_d \\ X_{ad} \\ R_f \end{bmatrix}_{n} + Bw \tag{3.3}$$

$$\begin{bmatrix} V_d \\ V_q \\ -V_f \end{bmatrix}_{n+1} = - \begin{bmatrix} I_d & -I_q & 0 & 0 & 0 \\ I_q & 0 & I_d & -I_f & 0 \\ 0 & 0 & 0 & 0 & I_f \end{bmatrix}_{n+1} \begin{bmatrix} R \\ X_q \\ X_d \\ X_{ad} \\ R_f \end{bmatrix}_{n+1} + v \tag{3.4}$$

Where $A = 1$, with $Q = diag[0.05, 0.05, 0.05, 0.05, 0.05]$ representing the process covariance matrix and $R = diag[0.05, 0.05, 0.05]$ representing the measurement covariance matrix with values based on a similar filter [26].

Bayesian inference e1: parameter estimation at steady state

Considering the state space model in Equation 3.2 as the functional likelihood distributions for Bayesian inference. Assumptions for selecting prior distributions for the parameters are as follows.

- Resistance in stator windings is usually very small [26].
- Salient pole generator is considered, hence, $X_d > X_q$ as seen in Chapter 2.2.1.

Based on these assumptions are the parameter priors with hyperparameters given in Equations 3.5-3.10. All hyperparameters are assumed weakly informed as uniformly distributed in reasonable a p.u. range.

$$R \sim \quad U < 0, 0.1] \tag{3.5}$$
$$X_d \sim \quad U < 0, 2] \tag{3.6}$$
$$X_q \sim \quad U < 0, X_d] \tag{3.7}$$
$$X_{ad} \sim \quad U < 0, 2] \tag{3.8}$$
$$R_f \sim \quad U < 0, 2] \tag{3.9}$$
$$\tag{3.10}$$

The likelihood distributions are given by Equations 3.11-3.13, all assumed Gaussian with low standard deviations as the units are in p.u.

$$\hat{V_d} \sim N(V_d(R, X_q, I_d, I_q), 0.1) \tag{3.11}$$
$$\hat{V_q} \sim N(V_q(R, X_d, X_{ad}, I_d, I_q, I_f), 0.1) \tag{3.12}$$
$$\hat{V_f} \sim N(V_f(R_f, I_f), 0.1) \tag{3.13}$$

Bayesian inference e2: parameter estimation without rotor angle measurements

When the rotor angle is not accessible either through measurements or by Equations presented in Chapter 2.2.3, will the prior distribution change, given by Equations 3.14-3.19.

$$R \sim U < 0, 0.1] \tag{3.14}$$
$$X_d \sim U < 0, 2] \tag{3.15}$$
$$X_q \sim U < 0, X_d] \tag{3.16}$$
$$X_{ad} \sim U < 0, 2] \tag{3.17}$$
$$R_f \sim U < 0, 2] \tag{3.18}$$
$$\delta_i \sim U < 0, \tfrac{\pi}{2}] \tag{3.19}$$

Where δ_i is added rotor angle position at each steady state position considered. As the available observations now consist of terminal quantities, will the resulting likelihood distributions be given as Equations 3.20-3.22.

$$\hat{V_{di}} \sim N(\tfrac{V_d(R, X_q, I_d, I_q)}{\sin(\delta_i)}, 0.1) \tag{3.20}$$
$$\hat{V_{qi}} \sim N(\tfrac{V_q(R, X_d, X_{ad}, I_d, I_q, I_f)}{\cos(\delta_i)}, 0.1) \tag{3.21}$$
$$\hat{V_{fi}} \sim N(V_f(R_f, I_f), 0.1) \tag{3.22}$$

Where i represents the $i'th$ rotor angle position, hence, given multiple steady-state rotor angles, does the model have to be split into multiple sets of likelihood distributions.

3.3.2 Extended Kalman filter for Rotor angle state estimation

Chapter 2.2.1 presented a reference change from the time domain to the rotor angle domain, with this making the reactances constant w.r.t. time. The reference change demands knowledge of the rotor angle. Section 2.2.3 presented common methods of calculating the rotor angle. The methods require knowledge of either parameters, optical

measurements, or measurements of the mechanical velocity compared to the grid frequency. All of which will be vulnerable to noise or error in measurements. As presented in 2.5.2 will, a Kalman filter will be able to filter out stochastic noise and estimate non-measured values with enough information about the system. As presented in Chapter 2.2.1 are, the electromechanical reactions in the synchronous generator non-linear, requiring an extended Kalman filter.

Extended Kalman Filter - algorithm

Considering the case of measured terminal voltage, current, and angle, as well measurements of active and reactive power. With the goal of estimating the rotor angle, the states are presented as Equation 3.23.

$$x = \begin{bmatrix} V \\ I \\ \theta \\ \delta \end{bmatrix}, z = \begin{bmatrix} V \\ I \\ \theta \\ P \\ Q \\ \delta \end{bmatrix} \tag{3.23}$$

The resulting state transition matrix is given in Equation 3.24, using the theory presented in Chapter 2.2 [7].

$$\hat{x_k} = f(x_{k-1}) = \begin{bmatrix} \sqrt{V_d^2 + V_q^2} \\ \sqrt{I_d^2 + I_q^2} \\ \theta \\ \delta \end{bmatrix} \tag{3.24}$$

With the Jacobian given in Equation 3.25.

$$F(\hat{x_k}) = \begin{bmatrix} 1 & 0 & 0 & 0 \\ 0 & 1 & 0 & 0 \\ 0 & 0 & 1 & 0 \\ 0 & 0 & 0 & 1 \end{bmatrix} \tag{3.25}$$

The measurement to state-matrix is given in Equation 3.26.

$$h(x) = \begin{bmatrix} \sqrt{V_d^2 + V_q^2} \\ \sqrt{I_d^2 + I_q^2} \\ \tan^{-1}\frac{I_d}{I_q} - \tan^{-1}\frac{V_d}{V_q} \\ V_d \cdot I_d + V_q \cdot I_q \\ V_q \cdot I_d - V_d \cdot I_q \end{bmatrix} \tag{3.26}$$

With the Jacobian of the state transition matrix given in Equation 3.27.

$$H(\hat{x_k}) = \begin{bmatrix} 1 & 0 & 0 & 0 \\ 0 & 1 & 0 & 0 \\ 0 & 0 & 1 & 0 \\ I_d \sin(\delta) + I_q \cos(\delta) & V_d \sin(\delta + \phi) + V_q \cos(\delta + \phi) & V_d I_q - V_q I_d & 0 \\ 0 & 0 & \frac{1}{V_q(\frac{V_d^2}{V_q^2}+1)} & 1 \end{bmatrix} \tag{3.27}$$

Given the relationships between states as presented in Chapter 2.2.1, must the process covariance matrix represent the covariances, the close covariance of the The process covariance matrix is given by knowledge of the system, or calculated using Equation 3.28.

$$Q = COV(V, I, \theta, \delta) \tag{3.28}$$

Where V, I, θ, and δ are previous measurements/estimated values from the system. With an estimated rotor angle, will the overall estimation process be as according to Figure 3.6.

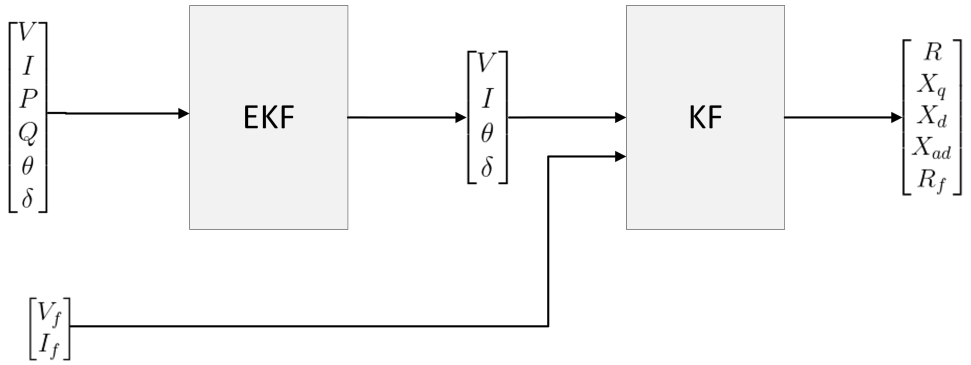

Figure 3.6: Estimation process with extended Kalman filter for rotor angle estimation and Kalman filter for parameter estimation at steady state

3.4 Thermal parameter estimation

This chapter will use the theory presented in Chapter 2.4, to build a thermal model of the synchronous generator. The model will consider general assumptions made from the geometrical shape of the synchronous generator together with heat sources presented in Chapter 2.3.

Heat sources

Considering the losses presented in Chapter 2.3, a summary of the power losses and their physical location on the generator is presented in Table 3.4.

Table 3.4: Power losses and respective location and material

PowerLoss	Location	Material
Rotor ohmic loss	Rotor winding	Copper
Stator ohmic loss	Stator winding	Copper
Core loss	Stator core	Iron
Stray loss	Unidentified	Unidentified
Friction and Windage loss	Unidentified	Unidentified

Table 3.4 shows that there are three losses that can be identified to a specific location; Rotor ohmic loss and stator ohmic- and core losses.

3.4.1 Thermal model

A summary of the assumptions made to establish a lumped capacity thermal model from Chapter 2.4 is given as;

- Spatially uniform internal temperature of the object - conduction dissipation neglected.
- Simultaneous heat dissipation through radiation and convection
- Radiation dissipated to the surrounding surfaces
- Convection dissipated to the surrounding fluid flow

When considering the heat sources from Table 3.4 and available measurements of the generator test rig from Figure 3.2 together with the assumptions for the lumped capacity thermal model it is clear that the model thermal model must be simplified as surface areas such as the generator cage are not measured. From Chapter 2.4, it is seen that

radiation is the dissipation process that is mostly affected by unknown surrounding surface temperatures. Hence are the final assumptions for the thermal model of the synchronous generator given;

- The friction and winding losses, as well as the stray losses, do not contribute directly to power loss in specific components in the generator, therefore they are assumed negligible for the heating of the stator core, stator windings, and rotor windings.
- Convection dissipation from all heat source elements to room temperature
- Dissipation between rotor and stator is neglected.
- The thermal buoyancy layers of the heat source elements in the stator will be affected by each other. Hence will the intermedium finite fluid flow be affected by multiple buoyancy layers. Based on this, it is assumed convective dissipation from the stator core to a fluid with the temperature of the stator windings, and from the stator windings to a fluid with the temperature of the stator core.
- Based on the aforementioned assumptions, specific radiation dissipation between elements is neglected.
- Convection heat transfer coefficient is viewed as a total heat transfer coefficient, with radiation included.

Using the Equation for simplified total heat transfer, Equation 2.68 are the considered heat transfers in the model given by Equations 3.29-3.33.

$$P_{r2a} = hA_{r2a}(T_r - T_a) \tag{3.29}$$
$$P^s_{cu2a} = hA_{cu2a}(T^s_{cu} - T_a) \tag{3.30}$$
$$P^s_{fe2a} = hA_{fe2a}(T^s_{fe} - T_a) \tag{3.31}$$
$$P^s_{fe2cu} = hA_{fe2cu}(T^s_{fe} - T^s_{cu}) \tag{3.32}$$
$$P^s_{cu2fe} = hA_{cu2fe}(T^s_{cu} - T^s_{fe}) \tag{3.33}$$

P_{r2a} is the dissipation from the rotor to air. P^s_{cu2a} and P^s_{fe2a} are the dissipation from, respectively, stator windings and core to air. Were P^s_{cu2fe} are the heat transfer from stator windings to the core, and P^s_{fe2cu} are the heat transfer from stator core to windings, where $hA_{fe2cu} = hA_{cu2fe}$ as a result of the first law of thermodynamics [19]. Applying Equation 2.58 gives the heat storage capabilities in each element in Equations 3.34 - 3.36.

$$P_{st_r} = m^r_{cu}\hat{c}_{cu}\frac{dT_r}{dt} \tag{3.34}$$

$$P_{st_{cu}} = m^s_{cu}\hat{c}_{cu}\frac{dT^s_{cu}}{dt} \tag{3.35}$$

$$P_{st_{fe}} = m^s_{fe}\hat{c}_{fe}\frac{dT^s_{fe}}{dt} \tag{3.36}$$

$$\tag{3.37}$$

Where m^r_{cu} is the weight of the copper windings in the rotor, m^s_{cu} the weight of the copper windings one stator winding, and m^s_{fe} is the weight of the iron core. Considering the energy balance presented in Equation 2.57 with the heat transfers in Equations 3.29-3.33 and stored energy from Equations 3.34-3.36, results in the thermal model of the generator in Equations 3.38-3.40.

$$\dot{T}_r = \frac{P_r - hA_{r2a}(T_r - T_a)}{c_{cu}m^r_{cu}} \tag{3.38}$$

$$\dot{T}^{s1\phi}_{cu} = \frac{P_s - hA_{cu2fe}(T^s_{cu} - T^s_{fe}) - hA_{s2a}(T_s - T_a)}{c_{cu}m^s_{cu}} \tag{3.39}$$

$$\dot{T}^s_{fe} = \frac{P_{fe} - 3hA_{fe2cu}(T^s_{fe} - T^s_{cu}) - hA_{fe2a}(T_{fe} - T_a)}{c_{fe}m^s_{fe}} \tag{3.40}$$

Where P_r, P_s and P_{core} are the power losses in, respectively, the rotor windings, stator winding, and core. The parameters of the thermal model are summarized in Table 3.5.

Where the specific heat and temperature coefficients are given in Table 3.6.

3.4.2 Likelihood and prior distribution of thermal parameters

The unknown parameters in Table 3.5 were estimated by Bayesian inference in Python, using the PyMc3 Library. In order to apply Bayesian inference must, the samples be independently distributed, as presented in Chapter 2.5.3. This was achieved by forward linearizing the model, resulting in Equations 3.41 - 3.43.

$$T_{r+1} = T_r + \Delta t\frac{P_r - hA_{r2a}(T_r - T_a)}{c_{cu}M^r_{cu}} \tag{3.41}$$

$$T^{s1\phi}_{cu+1} = T_{cu} + \Delta t\frac{P_s - hA_{cu2fe}(T^s_{cu} - T^s_{fe}) - hA_{s2a}(T_s - T_a)}{c_{cu}M^s_{cu}} \tag{3.42}$$

$$T^s_{fe+1} = T_{fe} + \Delta t\frac{P_{fe} - 3hA_{fe2cu}(T^s_{fe} - T^s_{cu}) - hA_{fe2a}(T_{fe} - T_a)}{c_{fe}M^s_{fe}} \tag{3.43}$$

Table 3.5: Parameters of the thermal model, *=estimated

Parameter	Description	Unit	Known
P_r	Power loss form the copper windings in rotor	W	Yes
P_s	Power loss from one phase of stator copper windings	W	Yes
P_{fe}	Power loss from armature core	W	Yes
P_{fe}	Power loss from armature core	W	Yes
T_a	Room temperature	K	Yes
T_r	Rotor temperature	K	Yes*
T_s	Stator winding temperature	K	Yes
T_{fe}	Armature core temperature	K	Yes
c_{cu}	Specific heat copper	$J/kg \cdot K$	Yes
c_{fe}	Specific heat iron	$J/kg \cdot K$	Yes
α_{cu}	Temperature coefficient copper	Ω/K	Yes
M_{rotor}	Total mass of rotor	kg	Yes
M_{stator}	Total mass of stator	kg	Yes
hA_{r2a}	Total heat transfer coefficient and surface area, rotor to air	W/m^2	No
hA_{cu2fa}	Total heat transfer coefficient and surface area, stator copper to air	W/m^2	No
hA_{cu2fe}	Total heat transfer coefficient and surface area, copper to iron	W/m^2	No
hA_{fe2a}	Total heat transfer coefficient and surface area, iron to air	W/m^2	No
M_{cu}^r	Rotor copper mass	kg	No
M_{cu}^s	Stator copper mass	kg	No
M_{fe}	Stator iron mass	kg	No

The prior distribution for the parameters, the hyperparameters, was selected based on the given assumptions.

- The total weight of the armature consists of the core and phase windings.
- The parameter distribution is unknown and therefore set to be uniformly distributed.
- The rotor copper weight is lower than the known total rotor weight of 24 kg.
- All masses are constrained to be positive.
- The heat dissipation from a source of heat to air is positive.

Table 3.6: Specific heat and temperature coefficients [27] [28]-

Parameter	Description	Value	Unit
c_{cu}	Specific heat copper	385	$J/kg \cdot K$
c_{fe}	Specific heat iron	462	$J/kg \cdot K$
α_{cu}	Temperature coefficient copper	$4e^{-}3$	Ω/K

- The likelihood distributions are assumed normally distributed with a low standard deviation.

The summarized prior distributions are given in Equations 3.44- 3.50.

$$hA_{r2a} \sim \quad U < 0,20] \tag{3.44}$$
$$hA_{cu2a} \sim \quad U < 0,50] \tag{3.45}$$
$$hA_{fe2a} \sim \quad U < 0,50] \tag{3.46}$$
$$hA_{cu2fe} \sim \quad U[-10,10] \tag{3.47}$$
$$m^r_{cu} \sim \quad U < 0,24] \tag{3.48}$$
$$m^s_{fe} \sim \quad U < 0,44] \tag{3.49}$$
$$m^s_{cu} = \quad \frac{44-M^s_{fe}}{3} \tag{3.50}$$

Almost every prior distribution is given as weakly informed with only a range specified without any bias. The only prior that is not given distributed value based on hyperparameters is m^s_{cu}, which is deterministic, based on the known weight of the stator from Table 3.5. The likelihood distributions are given as Equations 3.51-3.53.

$$\hat{T_r} \sim \quad N(\dot{T_r}(P_r, hA_{r2a}, m^r_{cu}, T_r, T_a), 1) \tag{3.51}$$
$$\hat{T_s} \sim \quad N(\dot{T_s}(P_s, hA_{cu2fe}, m^s_{cu}, T_{cu}, T_{fe}, , T_a), 1) \tag{3.52}$$
$$\hat{T_{fe}} \sim \quad N(\dot{T_{fe}}(P_{fe}, hA_{cu2fe}, m^s_{fe}, T_{fe}, T_{cu}, T_a), 1) \tag{3.53}$$

4 Results

This chapter will present the results obtained from using the theory from Chapter 2, together with the methodology presented in Chapter 3. The chapter is built up by first presenting the implemented control system results, then three study cases will be considered; the first case, Study Case A, will simulate results from the electrical model implemented in the digital twin. The Kalman filters, the basic KF, and the extended Kalman filter, EKF will be applied for estimating the electric parameters and state of the simulated model. Later will Study Case B present measured values through the data acquisition application, from the test-rig, with applied Kalman filters for estimation of electrical parameters. At last will, thermal measurements from measurement sessions with the test-rig be presented, and thermal parameters will be estimated.

4.1 Control system

This section will present results from implemented control systems, both in the digital twin and in the test rig through the DAQ.

4.1.1 Digital twin control systems

Both automatic voltage regulator and governor control were implemented in the digital twin. Figure 4.1 presents a simulation initialized with approximately steady state, delivering 0.7 p.u. active power and absorbing 0.2 reactive power. The governor setpoint is changed at $t = 100$ s and $t = 200$ s; voltage reactions with and without AVR are presented in Figure 4.1.

The field voltage effectively oscillates to reduce the impact on the terminal voltage when AVR is activated, compared to without AVR.

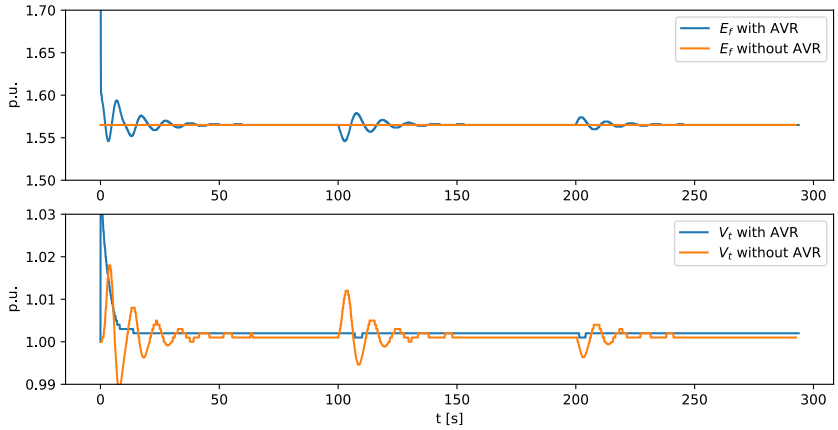

Figure 4.1: Voltage oscillations due reaction due to a frequency deviation at infinity bus with and without AVR (Non-reciprocal per unit rotor values).

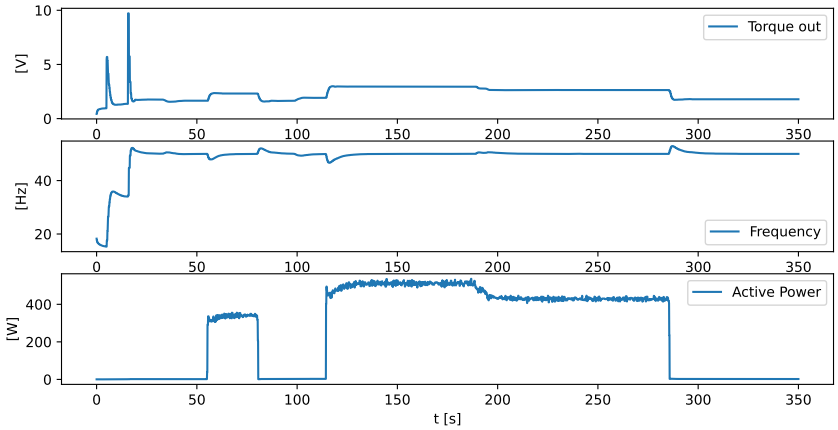

Figure 4.2: Torque PID controlled to 50 Hz, reactions to load activation and rejections

4.1.2 Test rig control systems

Torque PID control reactions when subject to load activation and rejection are presented in Figure 4.2.

As seen from Figure 4.2 does the torque output signal effectively adjust to the load rejection and activations to restore the frequency of 50 Hz.

4.2 Case A: Electrical Parameter estimation - Simulation

This Study Case considered a simulation of generator reaction subject to several changes in setpoint. The study case is simulated using the digital twin, hence the fourth-order

synchronous generator model, presented in Chapter 2.2.1. The case will first consider direct parameter estimation through the presented Kalman filter and Bayesian Inference at steady-state conditions. Later will, the proposed extended Kalman filter, EKF, be tested upon increasing noise to the rotor angle measurement, to get an overview of the robustness of the filter. The Synchronous Generator parameters used for the study case are listed in Table 4.1. The standard parameters are based on previous knowledge of the test rig synchronous generator [2].

Table 4.1: Simulated Generator model parameters.

Parameter	Value [p.u.]
M	3.5
D	0.5
R	0.03
X_d	0.86
X'_d	0.75
X_q	0.65
X'_q	0.65
T'_{d0}	1.3 s
T'_{q0}	0.03 s
R_f	1.5
X_{ad}	0.96

The selected transient directional and quadrature reactances, as well as time constants, T'_{d0} and T'_{q0}, inertia constant M and damping coefficient, D, are based on typical salient pole generator values [7].

Simulated session

The study case simulation was selected to be simulated for 500 s, with an initial state of no active or reactive power generation. The events applied to the generator model during the simulation time are listed in Table 4.2.

Table 4.2: Simulated Generator model parameters.

Time [s]	Event
0	Governor setpoint changed: $P_m = 0.7$
100	Governor setpoint changed: $P_m = 1.0$
200	Governor setpoint changed: $P_m = 0.8$
300	AVR setpoint changed: $V_t = 0.9$
400	AVR setpoint changed: $V_t = 1.1$

The resulting simulation measurements of terminal voltage and current values, as well as terminal active and reactive power, are presented in Figure 4.3.

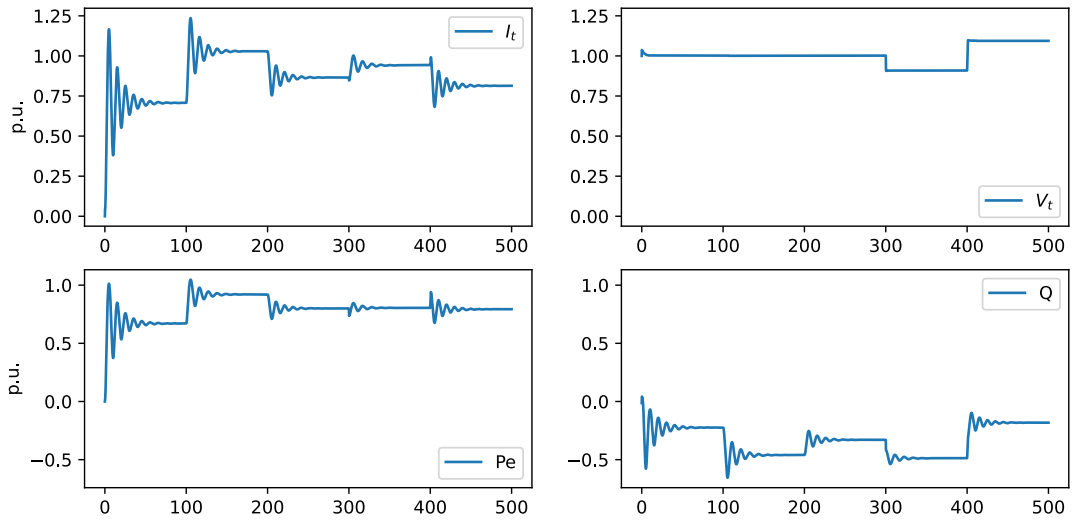

Figure 4.3: Simulated terminal voltage, currents and power.

As presented in Chapter 3.3.1, does the presented methodology for electrical parameter estimation require steady-state conditions. The identified steady-state conditions, with reference to the rotor angle during the simulation, are presented in Figure 4.4.

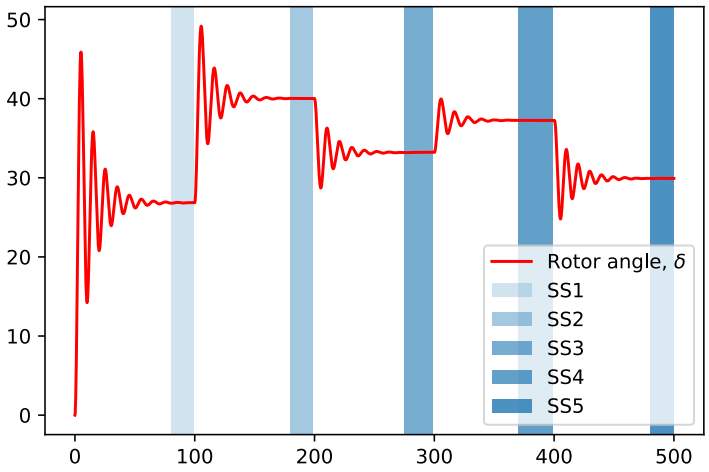

Figure 4.4: Rotor angle throughout the simulated session with the identified steady-state operation.

Table 4.3: Results Kalman Filter with correct initial values

Parameter	Est. value	Error [%]	Mean last 100 iterations	Std. dev. last 100 iterations
Noise=0				
R	0.03	0.007	0.03	0.0
X_q	0.65	0.0	0.65	0.0
X_d	0.861	0.001	0.861	0.0
X_{ad}	0.96	-0.0	0.96	0.0
R_f	1.5	0.0	1.5	0.0
Noise=0.03				
R	-0.027	-1.905	-0.033	0.006
X_q	0.638	-0.018	0.63	0.01
X_d	0.985	0.146	0.983	0.002
X_{ad}	0.933	-0.029	0.946	0.009
R_f	1.506	0.004	1.493	0.012
Noise=0.1				
R	0.108	2.609	0.099	0.021
X_q	0.664	0.021	0.673	0.04
X_d	0.752	-0.125	0.749	0.006
X_{ad}	0.972	0.012	0.98	0.029
R_f	1.529	0.019	1.514	0.035

Kalman filter electrical parameter estimation

Applying the presented Kalman filter, KF, for estimating standard electrical parameters. Using the simulation measurements of directional and quadrature voltage and currents, together with, the results of the estimated values, compared to the correct values as a reference. The estimated parameters from the Kalman filter are listed in Table 4.3, with correct initial values given to the Kalman Filter,KF.

The filter successfully keeps the correct values for all parameters at no noise, there are also no deviations in estimates for the last 100 iterations. At higher noise levels are, the filter still able to identify most parameters correctly, yet, with higher deviation in estimations for the last 100 iterations. The estimation of parameter R, shows a higher error with 2.6 % at 0.1 % noise applied. Running the Kalman Filter again, with all initial parameter values at zero, the estimated parameters are listed in Table 4.4.

The resulting estimations with zero initial parameters present larger estimation errors of all parameters, with the highest estimation error with parameter R. The estimation of parameters, X_d and X_{ad}, does also present a higher estimate error, with the largest error at zero noise. Using the final estimated values at all considered noise levels and initial

Table 4.4: Results Kalman Filter with zero initial values

Parameter	Est. value	Error [%]	Mean last 100 iterations	Std. dev. last 100 iterations
Noise=0				
R	-0.04	-2.341	-0.04	0.0
X_q	0.629	-0.033	0.629	0.0
X_d	0.512	-0.405	0.512	0.0
X_{ad}	0.839	-0.126	0.84	0.0
R_f	1.5	0.0	1.5	0.0
Noise=0.03				
R	0.061	1.025	0.06	0.005
X_q	0.666	0.025	0.665	0.01
X_d	0.646	-0.249	0.645	0.001
X_{ad}	0.934	-0.027	0.936	0.006
R_f	1.513	0.009	1.5	0.01
Noise=0.1				
R	-0.01	-1.328	-0.007	0.018
X_q	0.636	-0.021	0.645	0.031
X_d	0.33	-0.616	0.332	0.006
X_{ad}	0.836	-0.129	0.829	0.026
R_f	1.463	-0.025	1.51	0.033

Table 4.5: Goodness of fit using the last value of the Kalman Filter.

	Initial θ *=0*			*Initial* θ *=*$\theta_{correct}$		
State	R^2	MSE	RMSE	R^2	MSE	RMSE
Noise=0						
V_d	0.984	0.0	0.008	1.0	0.0	0.0
V_q	0.744	0.0	0.022	1.0	0.0	0.0
V_f	1.0	0.0	0.0	1.0	0.0	0.0
Noise=0.03						
V_d	0.981	0.0	0.009	0.997	0.0	0.004
V_q	0.744	0.0	0.022	0.944	0.0	0.01
V_f	0.887	0.001	0.033	0.9	0.001	0.031
Noise=0.1						
V_d	0.992	0.0	0.006	0.995	0.0	0.005
V_q	0.538	0.001	0.03	0.212	0.002	0.039
V_f	0.394	0.012	0.107	0.419	0.011	0.105

values to calculate the directional, quadrature and field voltages. The results, compared to the actual directional, quadrature and field voltage, are listed in Table 4.5.

The R^2 of the estimates of the directional voltage, V_d, presents the highest value throughout changing initial values and noise level applied. With the R^2 of the estimations of the quadrature voltage, V_q, presenting a low value at the wrong initial parameters, as well as in the highest noise case. The estimation of field voltage, V_f, presents a R^2 which becomes lower with applied noise to the signals. The MSE and $RMSE$ of the estimates are lowest for the directional voltage and quadrature voltage, be

Bayesian Inference

Applying Bayesian Inference, using the prior and likelihood distributions presented in Chapter 3.3.1, using the steady-state measurements as observations, results in the posterior parameter distribution Figure 4.5.

The mean values of the posterior distributions present correct estimates. The confidence interval of the estimated parameters is in the order of magnitude of -5 for all parameters except the parameters R and X_d, which got a confidence interval in the order of magnitude -4. The standard deviation, σ, of the observations from the likelihood distributions is given a mean value of $5.1e^{-}5$. The kernel density estimation of the estimated parameters is presented in Appendix B, Figure B.1. The kernel density estimation for the parameters presents a low correlation for most of the parameters, with some a small positive correlation for X_{ad} - R, R - X_q, and R - X_{ad}.

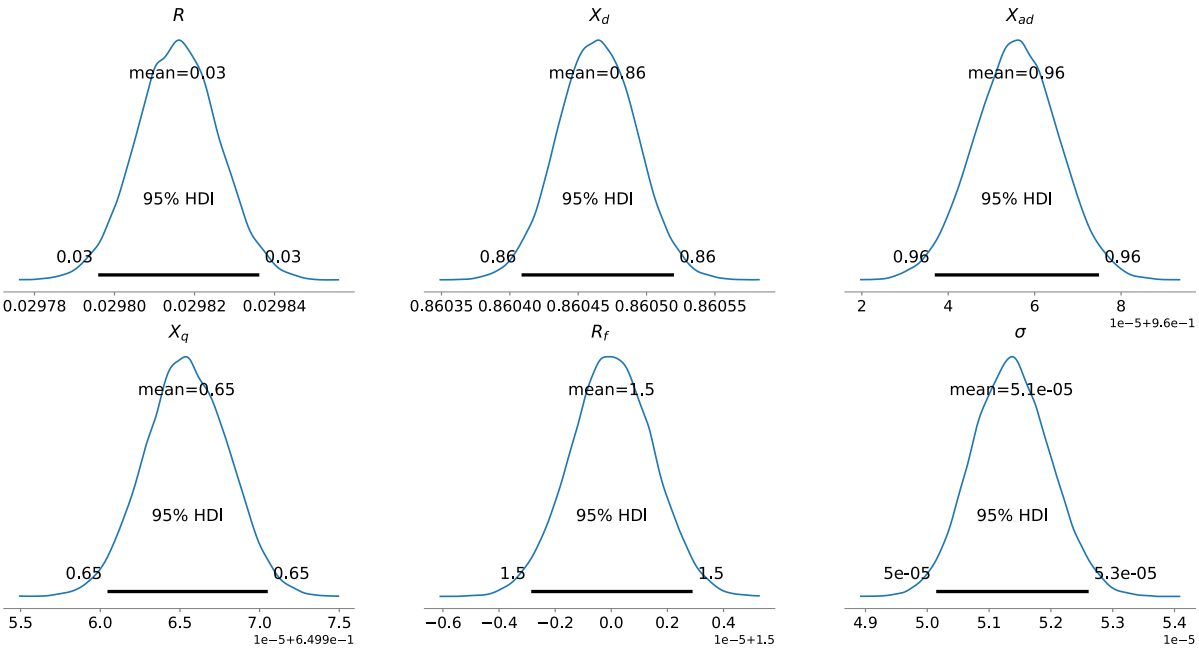

Figure 4.5: Posterior distribution simulation.

Table 4.6: Goodness of fit measures of the estimated rotor angle versus simulated value during the simulation.

Noise	R^2	MSE	RMSE
0.01	0.932	0.001	0.027
0.1	0.956	0.0	0.022
0.5	0.58	0.004	0.067
1.0	-0.29	0.014	0.117

4.2.1 Rotor angle state estimation

The extended Kalman filter, EKF, was applied to estimate the rotor angle throughout the simulated session, with an increased degree of noise added to the rotor angle measurement provided to the filter. The noise added to the remaining measurements was kept at 0.01. The resulting estimation of the rotor angle at different noise levels is presented in Figure 4.6, with the actual rotor angle as a reference.

The noisy rotor angle measurements given to the filter are included in Appendix B, Figure B.2. The goodness of fit measures for each of the noise levels is presented in Table 4.6.

The filter was able to estimate the rotor angle at low noise levels. With added noise of 0.01 and 0.1 radians, the filter estimates the rotor angle with a R^2 value of, respectively, 0.932 and 0.956. The mean error is 0.027 radians for the case with 0.01 noise, and 0.022

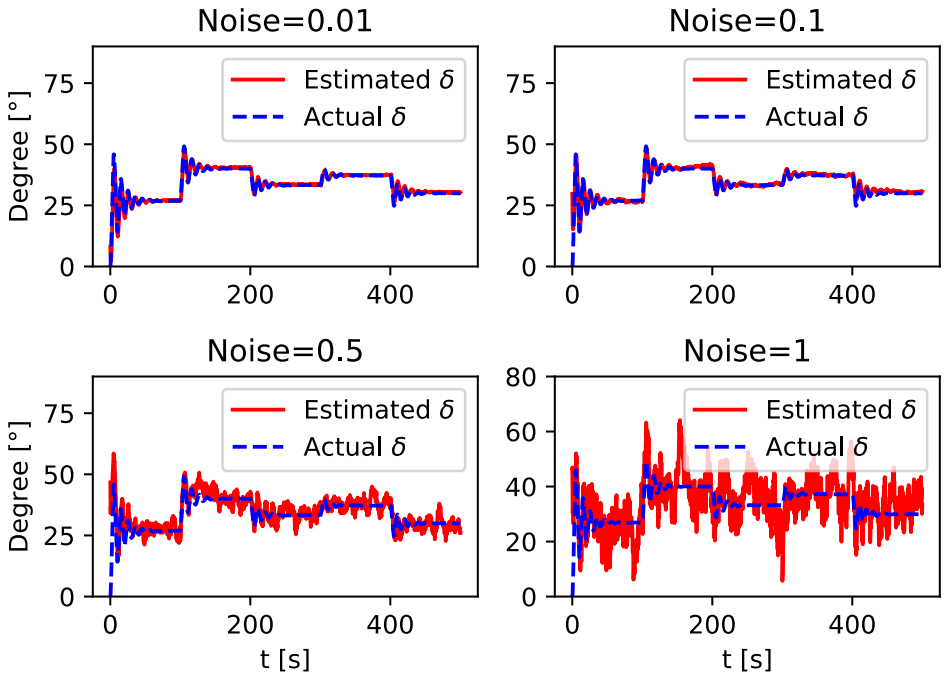

Figure 4.6: Estimated rotor angle at different noise level added to the rotor measurements

in the case with 0.1 noise. At higher noise levels, does the R^2 value decrease to 0.58 at 0.5 noise, and -0.29 at 1.0 noise. Yet, the filter keeps a low mean error, 0.067 radians at 0.5 noise, and 0.117 at 1.0 noise.

4.3 Case B: Electrical Parameter estimation - test rig

This section will present a study case consisting of the estimation of the electrical parameters of the generator test rig. Unlike Case A, this case does not access measurements of quadrature and directional voltage and current measurements. As a result, are EKF-A applied as an intermediate step of estimating the electrical parameters of the generator. The algorithms will be applied to a measurement session made from a dynamic loading session. The dynamic loading session represents the measurements of generator values during different loading conditions. The session was initially used to establish nominal stray loss of the generator, Journal in Appendix C. Post-processed measurements of terminal voltage, current and active and reactive power with identified steady-state conditions; $SS1, SS2,$ and $SS3$, are Presented in Figure 4.7. Raw measurements are available in Appendix B, Figure B.3.

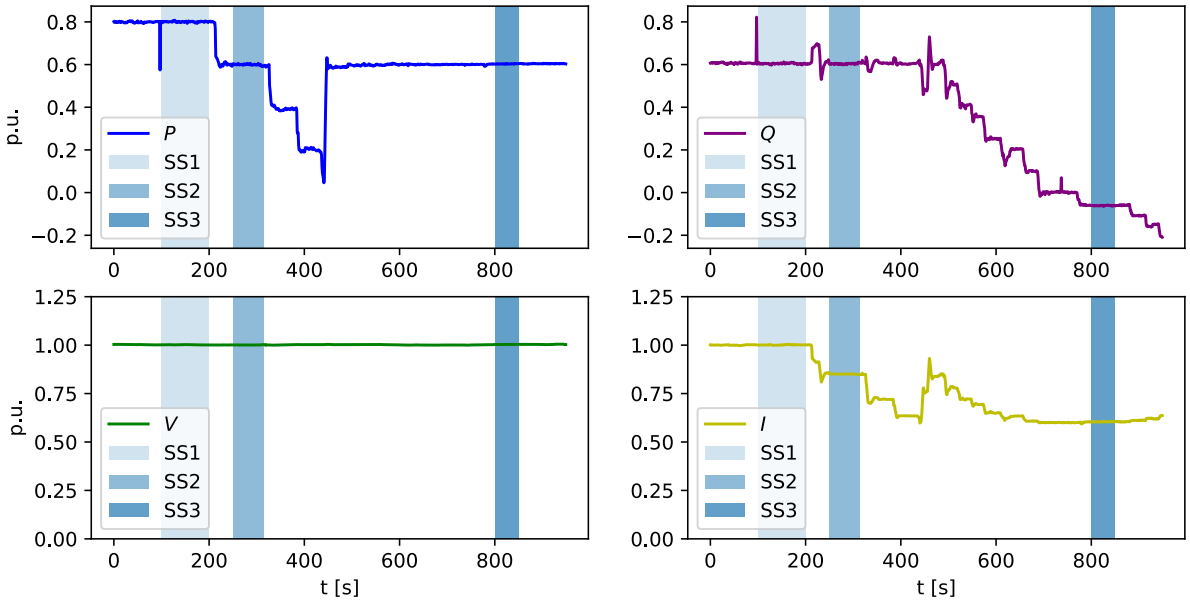

Figure 4.7: Measured terminal values during the session.

4.3.1 Per unit values

X_{ad} are calculated as the slope of the open circuit measurements of the generator presented in Figure 4.8 [2] [7].

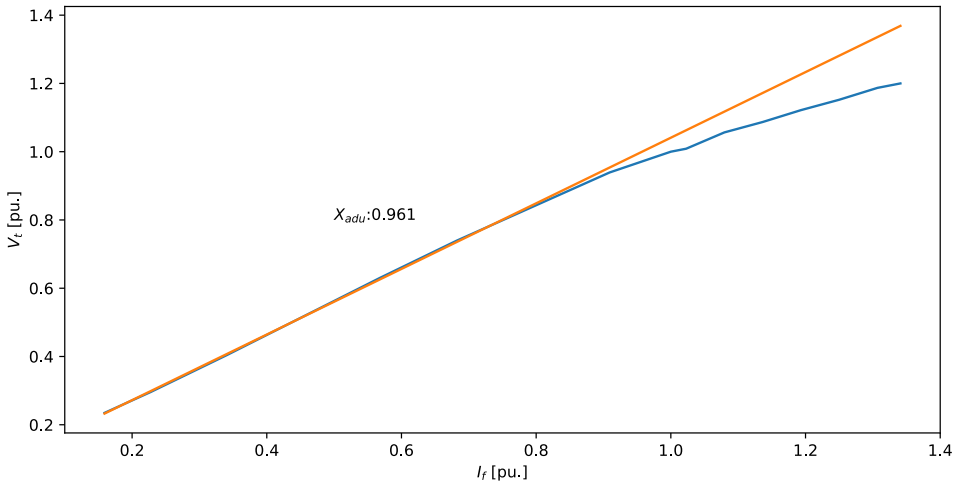

Figure 4.8: Estimated slope of the open circuit curve of the generator

The resulting reciprocal per unit base values of the generator, given the previously known parameters of the generator, the Equations presented in Chapter 2.2.5 and estimated X_{ad} are presented in Table 4.7.

Table 4.7: Reciprocal per unit values

Variable	Reciprocal base value	Unit
S_{base}	2000	VA
V_{base}	230	V
I_{base}	5.02	A
Z_{base}	26.5	Ω
$v_{f_{base}}$	22.33	V
$i_{f_{base}}$	0.845	A

Where S_{base}, V_{base}, I_{base}, and Z_{base} are stator base values and $v_{f_{base}}$, $i_{f_{base}}$ are reciprocal rotor base values.

4.3.2 Bayesian Inference

Applying Bayesian inference, at the identified steady-state conditions, with the prior and likelihood distribution presented in Chapter 3.3.1. The resulting posterior rotor angle distributions are presented in Figure 4.9.

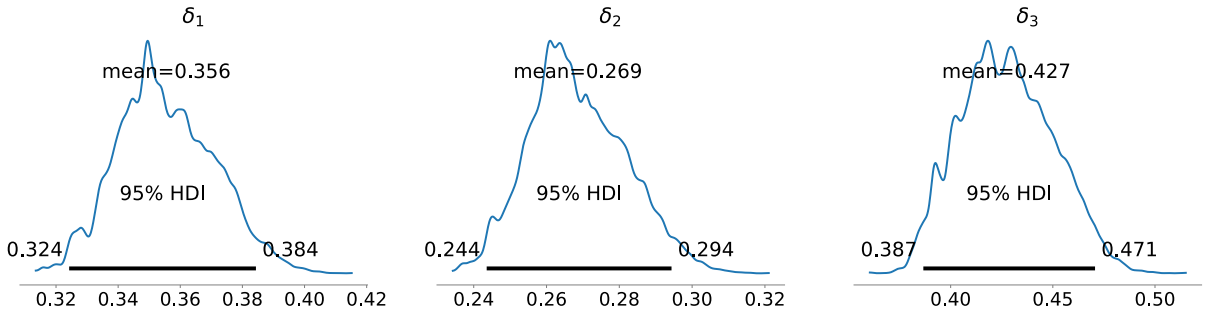

Figure 4.9: Estimated rotor angle during steady states during the dynamic loading session.

The posterior rotor angle distribution at steady state condition 1 is estimated to be 0.37 radians, with a certainty of 95 % that the rotor angle is in the interval from 0.3-0.44 radians. Steady-state condition 2 has an estimated rotor angle of 0.269 radians, with a certainty of 95 % that the rotor angle is within the interval of 0.244 to 0.294 radians. The posterior rotor angle distribution in the latter steady state condition that was considered resulted in an estimate of 0.427 radians with a certainty of 95 % that the rotor angle is within an interval of 0.387 to 0.471 radians. The resulting posterior parameter distribution is presented in Figure 4.10.

The posterior distribution of most parameters presents identified parameters, yet, the posterior distribution of stator phase resistance R does not have an amplified protrusion. The estimated parameter of the field winding resistance is the most certain estimation,

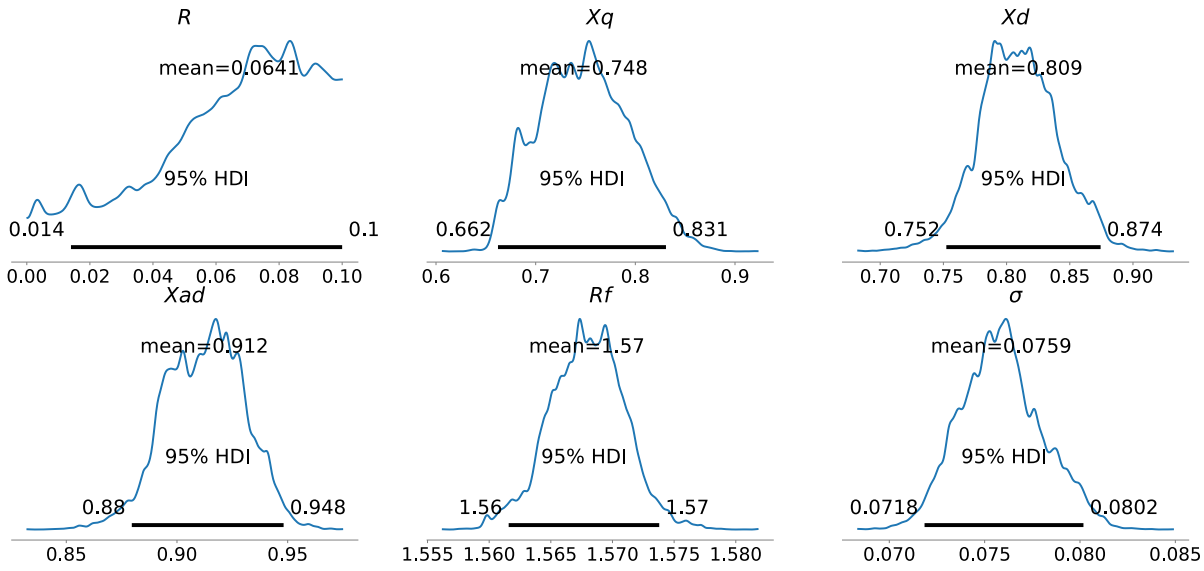

Figure 4.10: Estimated rotor angle during the dynamic loading session.

with a 95 % certainty of the resistance being in the interval of 1.56-1.57 p.u. The reactances are all estimated with a confidence interval of 0.2 p.u. The kernel density estimation of the estimated parameters is presented in Appendix B, Figure B.4. The kernel density estimation presents a high positive correlation between rotor angles 1 and 3, as well as some positive correlation between X_d and X_{ad}. The remaining densities present a very low correlation, the stator windings resistance presents an increased value of the peak density throughout the kernel density estimation.

4.3.3 Rotor angle estimation

Based on the resulting parameter estimation of the test rig parameters, the rotor angle calculated using Equation 2.20, considered as the stochastic parameter presented in Figure 4.10, approximately a standard deviation of 0.05. The proposed extended Kalman filter is applied to estimate the true rotor angle, both calculated and estimated through the EKF is presented in Figure 4.11.

4.3.4 Parameter estimation from the estimated rotor angle

Applying the Kalman Filter, KF, to estimate parameters at the identified steady-state conditions, based on the estimated rotor angle from Figure 4.11. Electrical parameters estimated from initial conditions at zero are presented in Table 4.8, with the error calculated as a percentage deviation from the mean posterior parameters from Figure 4.10.

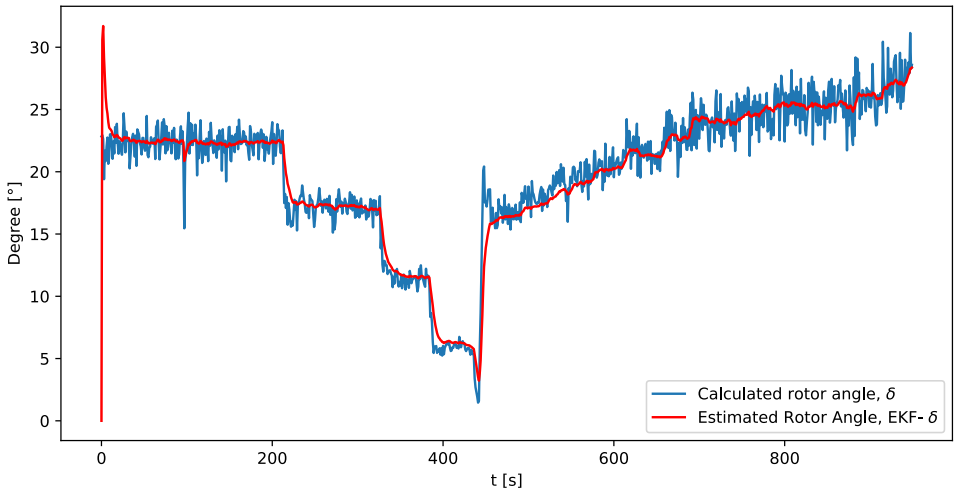

Figure 4.11: Estimated and calculated rotor angle during the session.

Table 4.8: Results Kalman Filter with zero initial parameter values

Parameter	Est. value	Error [%]	Mean last 100 iterations	Std. dev. last 100 iterations
Noise=0.01				
R	-0.062	-1.963	-0.156	0.099
X_q	0.729	-0.028	0.496	0.233
X_d	0.509	-0.371	0.196	0.318
X_{ad}	0.805	-0.118	0.623	0.18
R_f	1.392	-0.11	1.498	0.12
Noise=0.1				
R	0.207	2.222	-0.126	0.32
X_q	0.737	-0.018	0.4	0.452
X_d	0.66	-0.184	0.229	0.467
X_{ad}	0.948	0.04	0.639	0.295
R_f	1.406	-0.101	1.509	0.128

Table 4.9: Results Kalman Filter with correct initial parameter values

Parameter	Est. value	Error [%]	Mean last 100 iterations	Std. dev. last 100 iterations
Noise=0.01				
R	-0.044	-1.683	-0.018	0.016
X_q	0.725	-0.033	0.738	0.013
X_d	0.664	-0.18	0.714	0.038
X_{ad}	0.846	-0.072	0.863	0.023
R_f	1.388	-0.113	1.498	0.121
Noise=0.1				
R	-0.225	-4.51	-0.179	0.096
X_q	0.5	-0.334	0.577	0.127
X_d	0.555	-0.314	0.746	0.162
X_{ad}	0.74	-0.188	0.815	0.127
R_f	1.372	-0.124	1.51	0.124

The error in the estimates is highest for the stator winding resistance and directional reactance, with an error from 1.4 to 2.22% for the resistance. The quadrature reactance and magnetisation reactance proves the highest accuracy of the estimates. Electrical parameters estimated from initial conditions at correct values are presented in Table 4.9.

The error in the estimates proved again highest for the stator winding resistance and directional reactance, with an error of -4.51 % for the resistance at a noise level of 0.1. The quadrature reactance and magnetisation reactance did also prove the highest accuracy of the estimates. The Bayesian Inference (e1), was applied using the estimated rotor angle from Figure 4.11, and the resulting posterior distributions are presented in Figure 4.12.

The standard deviation from the likelihood distributions has a mean probability of 0.074 p.u. The magnetizing reactance is estimated to have a mean probability of 0.88 p.u. with 95% certainty of the value being in the range of 0.86 to 0.91 p.u. The directional and quadrature reactances mean probabilities are estimated to have the same value of 0.77 p.u. with a confidence interval in the range of 0.74 to 0.81 for the quadrature reactance, and 0.71 to 0.83 p.u. for the direct reactance. The field winding resistance is estimated to have a value of 1.6 p.u. while the phase winding in the stator have an estimated value of 0.017 p.u. with a confidence interval of 95 % from $5.3e^{-5}$ to 0.039. The kernel density estimation, presented in Appendix B, Figure B.5, presents a low correlation between the parameters, with some positive correlation between the magnetizing reactance, X_{ad} and directional reactance, X_d, and little positive correlation between the stator winding resistance and quadrature reactance, R and X_q.

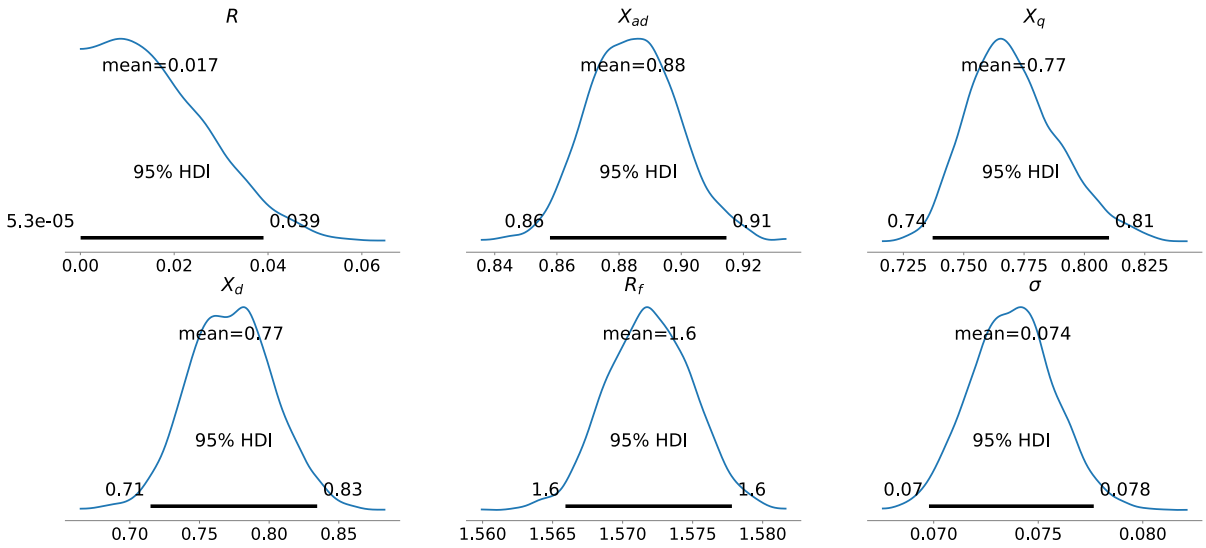

Figure 4.12: Bayesian inference, based on extended Kalman filter values.

4.4 Case C: Thermal Parameter estimation

This section will present the results from the estimation of the thermal properties of the test rig generator from two separate measurement sessions, together with the goodness of fit.

4.4.1 Dynamic load

The measured temperatures during the dynamic loading session are Presented in Figure 4.13.

The changes in estimated power losses that cause the deviation in temperature gradients for the windings and core during the session are presented in Figure 4.14.

Parameter estimation of stator thermal parameters

Bayesian inference was applied with the presented measurements as observations, and likelihood and prior distributions as presented in Chapter 3.4.2. The resulting posterior distribution for each of the parameters is presented in Figure 4.15.

The overall standard deviation for the likelihood distributions was estimated at 0.003 K. The total heat transfer coefficient and surface area from the core to the air at room temperature, hA_{fe2a}, was estimated to have a mean probability of 17.8 W/K, with a 95 % certainty that the value is within the range of 16.9 to 18.6 W/K. The total heat

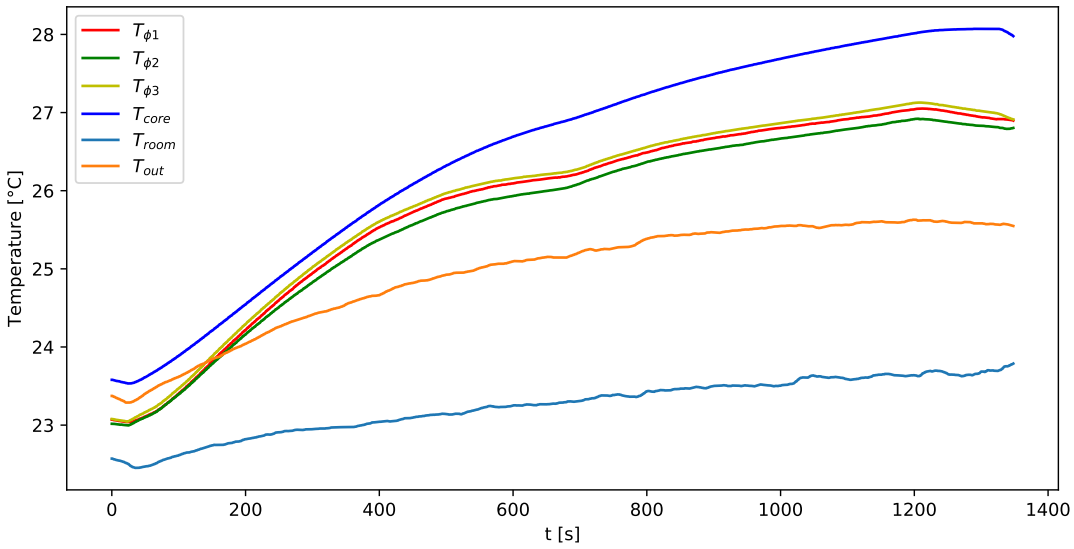

Figure 4.13: Measured temperatures of stator windings and core during the session.

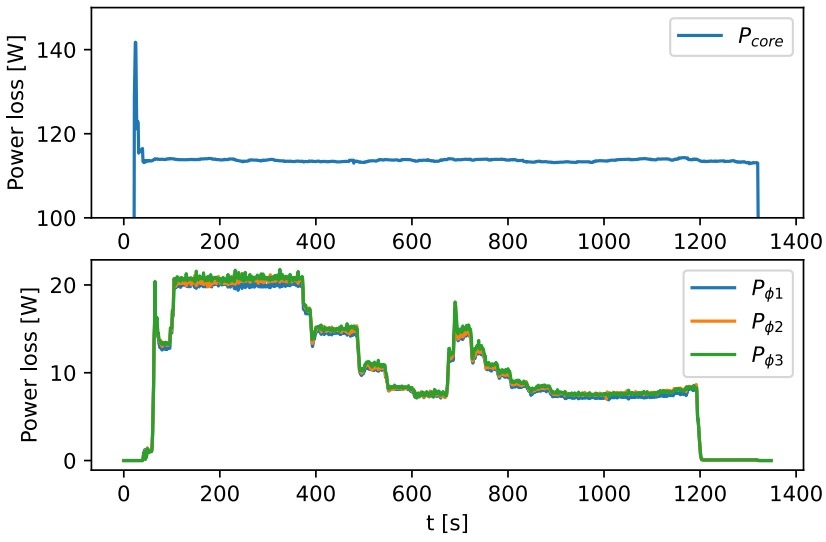

Figure 4.14: Estimated power losses in core and stator windings during the dynamic load session.

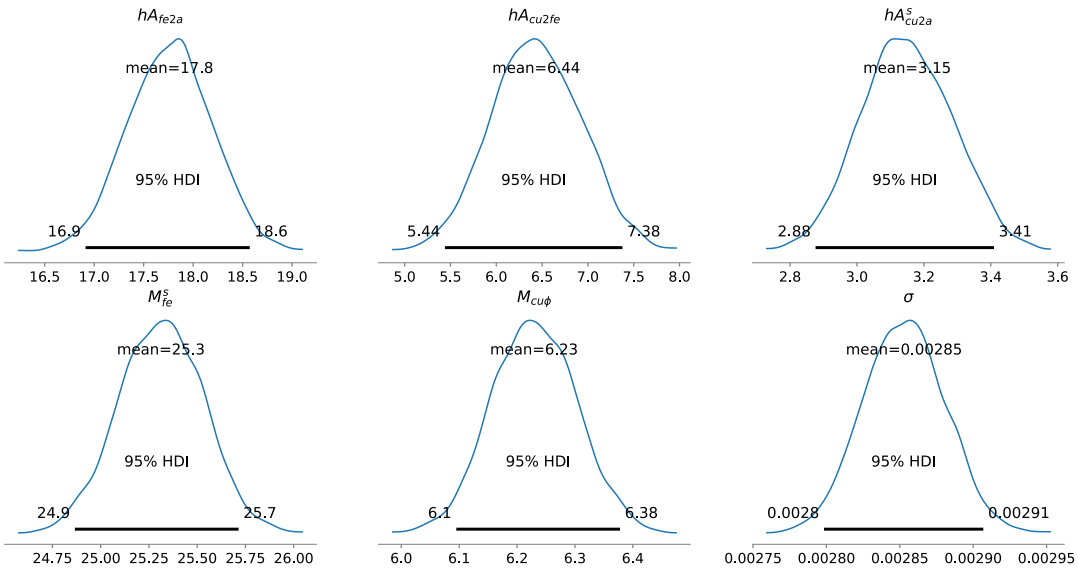

Figure 4.15: Posterior distribution of armature thermal parameters from stray loss estimation session

transfer coefficient and surface area from each of the stator phase windings to air at room temperature, hA_{cu2a}, was estimated to have a value of 3.15 W/K, with a 95 % certainty that the value is in the range of 2.88 to 3.41 W/K. The total heat transfer coefficient and surface area between each stator phase winding and the core, hA_{cu2fe}, was estimated to have a value of 6.44 W/K, with a 95 % certainty that the value is in the range of 5.44 to 7.38 W/K. The estimated masses for a phase copper winding and the core were estimated to respectively be 6.44 kg and 25.3 kg, with a 95 % certainty that the value is in the range of 6.1 to 6.38 kg for a winding, and 24.9 to 25.7 kg for the core.

The kernel density estimation plot, available in Appendix B, Figure B.6, presents a low correlation between the estimated parameters, except for the masses, which presents a high correlation due to the deterministic prior. The heat transfer coefficients from copper windings are also negatively correlated with the heat transfer coefficient from the core.

The mean values from the parameter posterior distributions were used to estimate the temperatures, given the measured power losses and temperature change in the room. The resulting simulations, compared to the measured temperatures, are presented in Figure 4.16. 4.16.

Rotor temperature and parameter estimation

The rotor temperature was calculated using Equation 2.44 and measurements of field voltage and current. The calculated rotor temperature is presented in Figure 4.17.

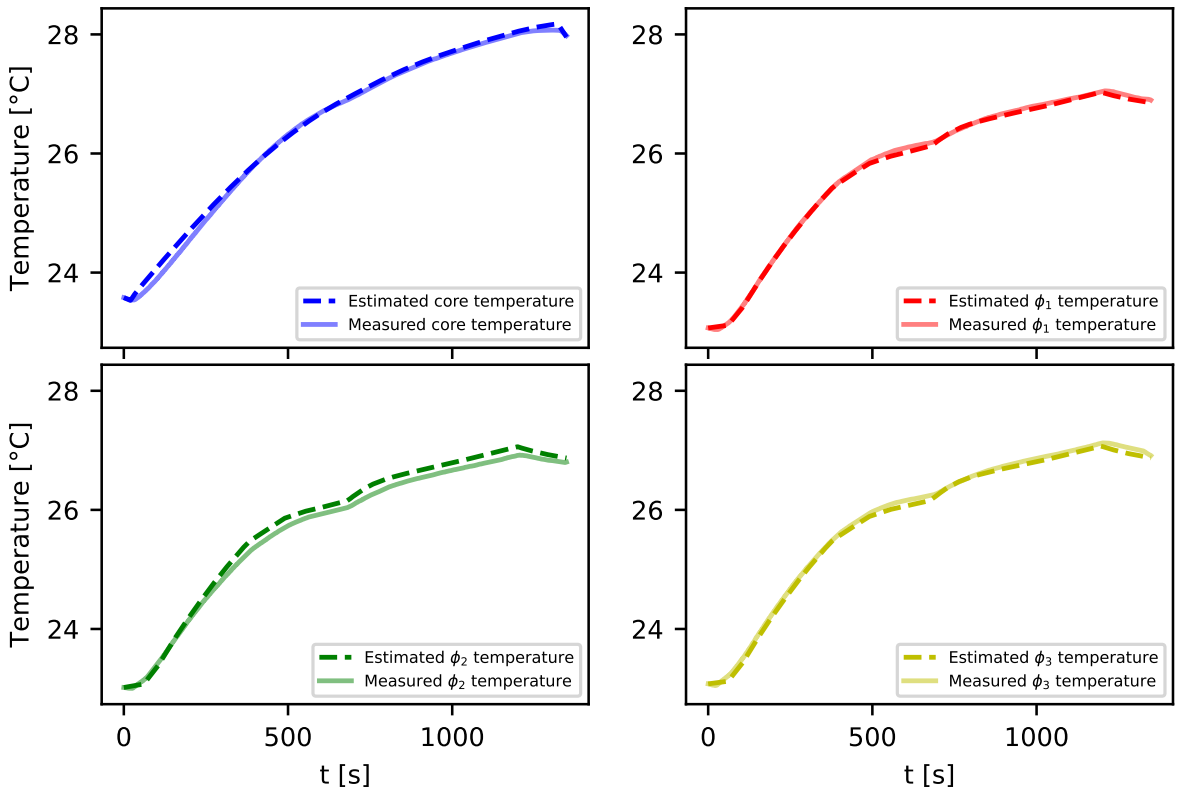

Figure 4.16: Comparison between estimated and measured temperatures in stator core and phases during stray load loss session

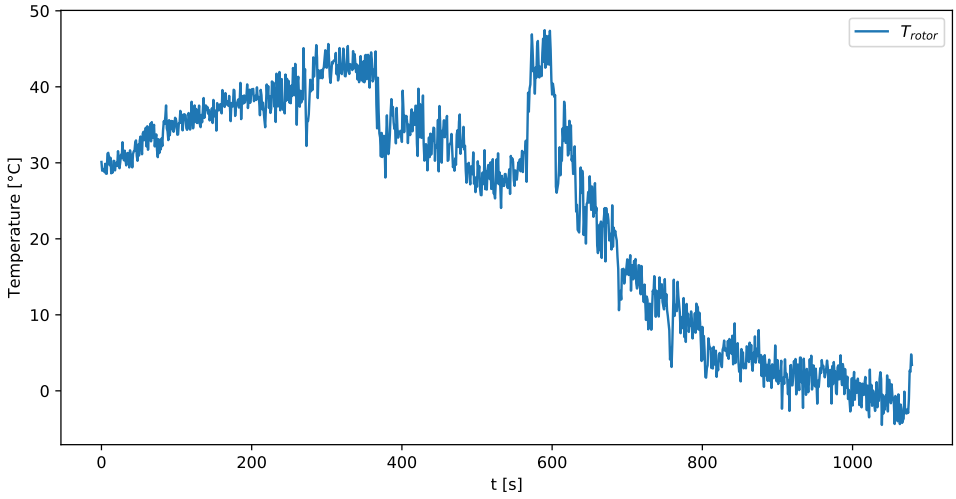

Figure 4.17: Calculated rotor temperature, during the dynamic load session.

Bayesian inference was applied with the calculated rotor temperature as observation together with measured room temperature, and likelihood and prior distributions as presented in Chapter 3.4.2. The resulting posterior distribution is presented in Figure 4.18. The

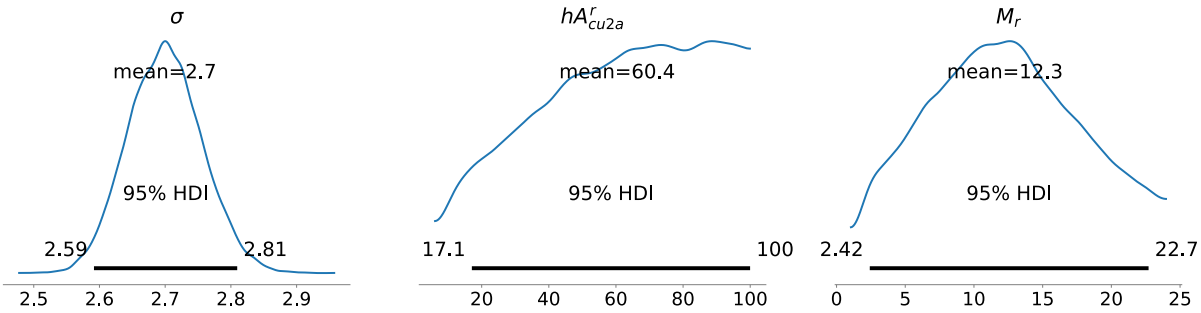

Figure 4.18: Posterior distribution of the rotor thermal parameters

standard deviation of the likelihood was estimated to be 2.7 K, the estimated total heat transfer coefficient and surface area from the rotor to air was estimated to have a mean probability of 60.4 W/K, yet, with a 95 % certainty of being in the range of 17.1 to 100 W/K. The mass of the rotor was estimated to have a mean probability of 12.3 kg, with 95 % certainty of the value being in the range of 2.42 to 22.7 kg. The kernel density estimation, available in Appendix B, Figure B.8 presents no significant kernel density, as also seen from the high confidence intervals in the posterior distributions. Figure 4.19 presents a simulation with the mean values of the posterior probabilities, compared to the calculated temperature.

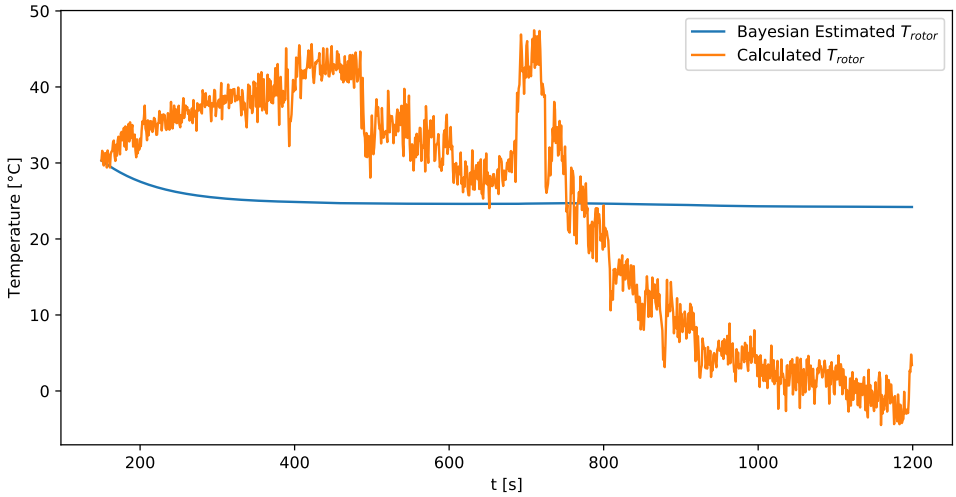

Figure 4.19: Comparison plot of Bayesian estimated- and calculated temperature of the rotor.

Goodness of fit

The goodness of fit for the simulated temperatures versus the measured and calculated values are summarized given in Table 4.10.

Table 4.10: Goodness of fit measures for estimated versus measured temperatures.

Location	R^2	MSE	RMSE
Phase 1	0.999	0.001	0.037
Phase 2	0.989	0.015	0.122
Phase 3	0.998	0.003	0.057
Core	0.997	0.006	0.078
Rotor	0.041	234.452	15.312

All phase winding and core estimates was measured to a R^2 value of 0.99 when rounded to two digits, with a low mean error of 0.1 K being the highest mean error for the aforementioned estimations. Yet, the rotor temperature estimate proved a poor fit, compared to the measured value.

4.4.2 Constant load

A steady-state laboratory test was conducted with the test rig. The journal from the laboratory session is included in Appendix C. Measured temperature values are presented in Figure 4.20.

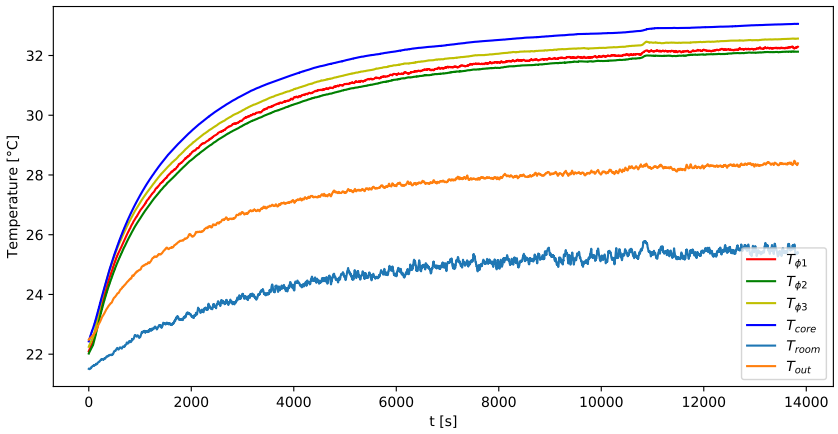

Figure 4.20: Temperature measurements from the steady state temperature session.

The core temperature proved the highest change in temperature, with each of the stator windings temperature rise being a little less. There was also a significant increase in room temperature, as well as the air going out of the generator.

Parameter estimation of stator thermal parameters

Applying Bayesian Inference, using the obtained measurements from the steady state session as observations. The selected prior and likelihood distributions presented in Chapter 3.4.2, resulting in the posterior distribution of stator thermal parameters, are presented in Figure 4.21.

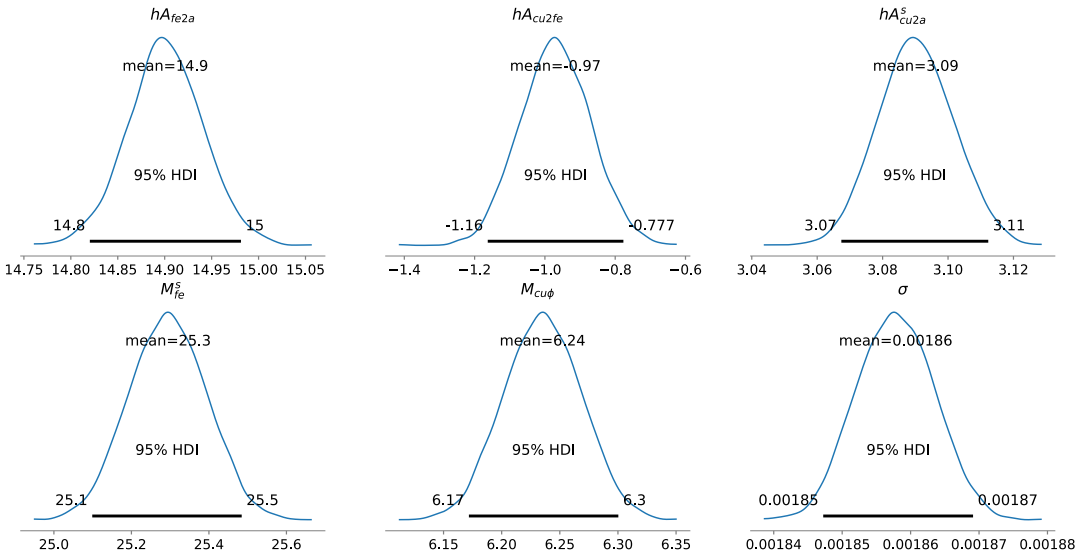

Figure 4.21: Posterior distribution of armature thermal parameters from steady state session

The standard deviation from the likelihood distributions was estiamted to a mean probability of $1.87 \cdot 10^{-3}$, with a 95 % certainty that the value is in the range of $1.85 \cdot 10^{-3}$ to $1.87 \cdot 10^{-3}$. The mean posterior probability for the total heat transfer coefficient and surface area between the core and windings was estimated to be -0.97 W/K, with a 95 % certainty of the value being in the range of -1.16 to -0.777 W/K. Considering the temperatures in Figure 4.20, and the thermal model in Chapter 2.4, does this result in the core being heated by copper windings. The total heat transfer coefficient and surface area from the core to the air at room temperature, hA_{fe2a}, was estimated to have a mean probability of 14.9 W/K, with a 95 % certainty that the value is within the range of 14.8 to 15 W/K. The total heat transfer coefficient and surface area from each of the stator phase windings to air at room temperature, hA_{cu2a}, was estimated to have a value of 3.09 W/K, with a 95 % certainty that the value is in the range of 3.07 to 3.11 W/K. The mass of the core was estimated to have a mean posterior probability of 25.3 kg, while each copper winding

was estimated to have a mean posterior probability of 6.24 kg, with a 95 % certainty of the masses being in the range of 25.1-25.5 kg and 6.17-6.3 kg respectively.

The kernel density estimation plot, available in Appendix B, Figure B.9, presents a low correlation between the estimated parameters, except for the masses, which presents a high correlation due to the deterministic priors. The heat transfer coefficients from copper windings are also negatively correlated with the heat transfer coefficient from the core.

The mean values from the parameter posterior distributions were used to estimate the temperatures, given the measured power losses and temperature change in the room. The resulting simulations, compared to the measured temperatures, are presented in Figure 4.22.

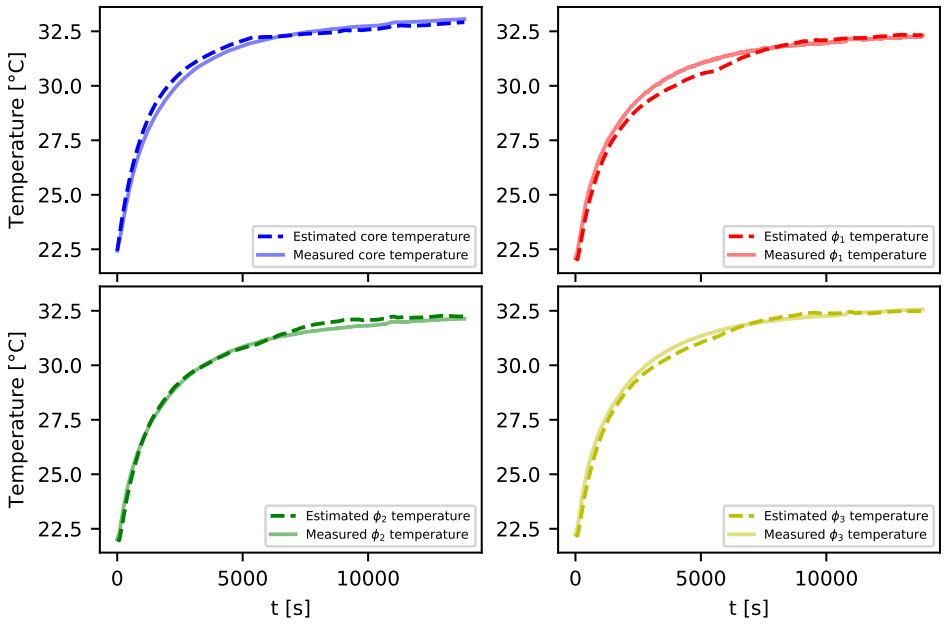

Figure 4.22: Comparison between estimated and measured temperatures in stator core and phases.

Rotor estimation

The rotor temperature was calculated using Equation 2.44 and measurements of field voltage and current. The calculated rotor temperature is presented in Figure 4.23. Bayesian inference was applied with the calculated rotor temperature as observation together with measured room temperature, and likelihood and prior distributions as presented in Chapter 3.4.2. The resulting posterior distribution is presented in Figure 4.24.

The standard deviation of the likelihood was estimated to be 2.25 K. The estimated total heat transfer coefficient and surface area from the rotor to air was estimated to have a

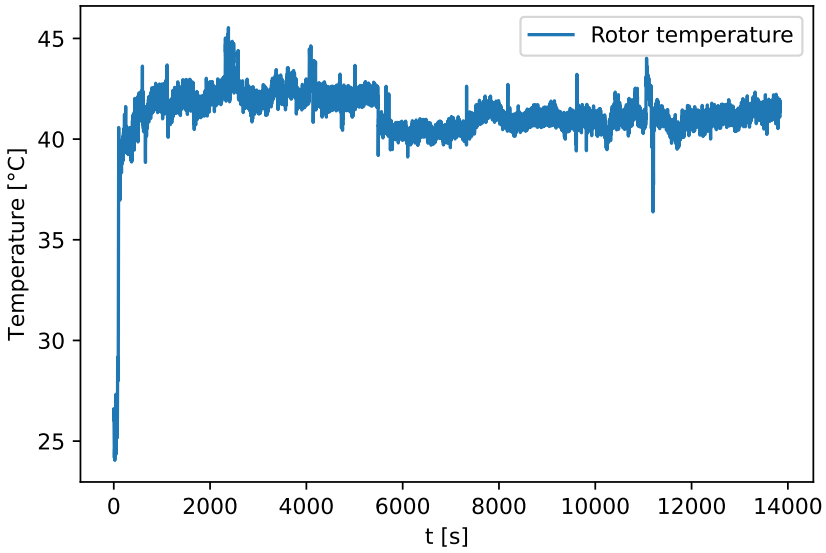

Figure 4.23: Estimated rotor temperature during the steady state measurement session.

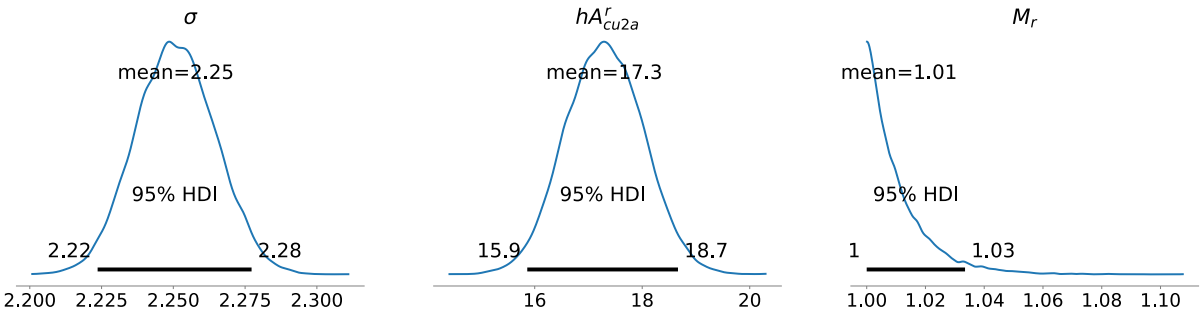

Figure 4.24: Posterior distribution of thermal rotor parameters.

mean probability of 17.3 W/K, yet, with a 95 % certainty of being in the range of 15.9 to 18.7 W/K. The mass of the rotor was estimated to have a mean probability of 1.01 kg, with 95 % certainty of the value being in the range of 1 to 1.03 kg. Figure B.10 presents kernel distributions close to the edges of the given range. Figure 4.25 presents a simulation with the mean values of the posterior probabilities, compared to the calculated temperature.

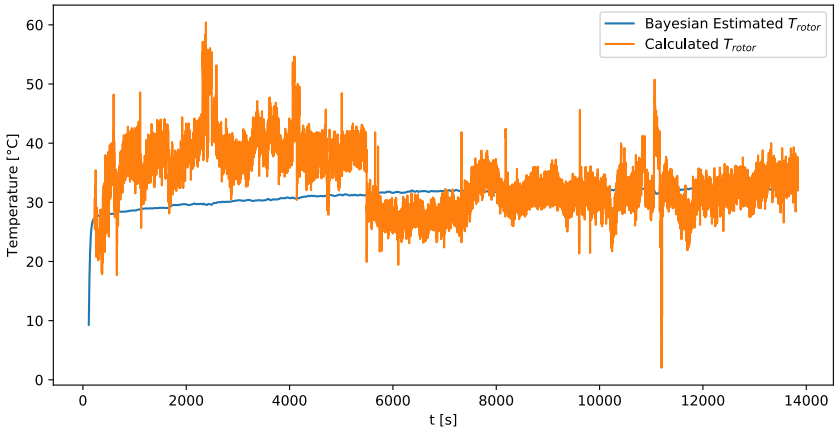

Figure 4.25: Comparison plot of Bayesian estimated- and calculated temperature of the rotor.

Goodness of fit

The goodness of fit measurements for the core and stator phase are presented in Table 4.11.

Table 4.11: Goodness of fit

Location	R^2	MSE	RMSE
Phase 1	0.975	0.109	0.33
Phase 2	0.992	0.036	0.189
Phase 3	0.987	0.057	0.239
Core	0.985	0.07	0.264
Rotor	-0.392	41.184	6.417

All phase winding and core estimates proved a high R^2 value of 0.975-0.99, with a low mean temperature error, yet, the rotor temperature estimate proved a poor fit, compared to the measured value. The rotor temperature presented a mean error of above 6 Kelvin.

5 Discussion

This chapter will attempt to interpret the obtained results presented in Chapter 4, mainly by considering the original problem statements presented in Chapter 1.3.

5.1 Data acquisition application

The thesis work was resolved around the main objective, further development of the data acquisition application as presented in the (MO). To address this objective, the software was rebuilt as a state machine in LabVIEW, with the key benefit of native support for the sensor measurements as National Instrument does the data acquisition hardware modules. The previously made SQL database solution was a cloud-based storage method with improved offline storage solutions. The main improvements of the application include improved measuring capabilities for the test rig and the making of a digital twin model. The results obtained in these subjects will be addressed in the following sections.

General Hydropower plant

The basis of a hydropower plant had to be established to establish a valid digital twin model of a hydropower plant. Hence, a brief survey of the hydropower plant was done in compliance with the first sub-objective, (O2). The findings from the survey presented the hydropower plant as an electromechanical model built on electromagnetic phenomena. The primary energy source of the hydropower plant stems from converting kinetic energy from a hydraulic system. The hydraulic part of the hydropower plant depends on the geometrical shape of the landscape around the turbine with the effect on the waterway. The hydropower plant's hydraulic system mainly controls the amount of active power. In order to maintain synchronous frequency in the power grid, the synchronous generator's active power production setpoint is set dynamically through the governor droop control, which controls the opening of the gate valves. Due to peculiar reactions in the waterway, hydropower plants acquire transient droop, lowering the initial movement of the gate valves. The amount of reactive power is controlled through the degree of excitation of the field winding, which controls the degree of magnetization. The degree of magnetization is controlled through the AVR, controlled through feedback from the terminal voltage of

the synchronous generator. The AVR control scheme contains configurable parameters for limiting the excitation, reference limits, and a voltage stabilizer signal.

Control systems

In an attempt to address sub-objective 3, (O3), were relevant control systems for the hydropower plant implemented into the application. In the digital twin were the control systems implemented directly into the solver, resulting in excepted behaviour, as seen in Chapter 4.1.1. When used to control the test rig, did the control systems get a time delta between measurements and control signals, resulting in a required low gain to remain stable, especially the AVR suffered from this added time delta, making it not possible to implement during the project work. Governor control and speed and control were implemented based on feedback measurements of the terminal frequency of voltage in phase a. However, the experimental testing of the implemented control systems was brief and required more testing and tuning.

Digital twin

The theoretical basis for an electromechanical mechanistic model of the synchronous generator was presented in Chapter 2.2.1, with the fourth-order model of the synchronous generator as the choice, neglecting direct consideration of damping windings, only including them through a damping coefficient. In addition, a simplified lumped capacity thermal model was developed with certain assumptions. The heat sources in the thermal model stem from the implemented power loss model presented in Chapter 2.3.

The digital twin was built using the relationship between the aforementioned electromechanical, power loss, and thermal models. Considering the types of digital twins, are the resulting implemented digital twin to be considered a type T3 from Table 2.1, as this type suggests a digital twin, compiled to represent a system of T2 twin models. Hence do the objectives, (O3), and (O4), complement each other into a system of mechanistic models, as they ought to be implemented in the same model or with some interaction between the models. The implemented digital twin was implemented with a direct connection to an infinity bus, which was assumed to represent a power grid with infinitely high network frequency characteristics, meaning changes in the generator production had no effect on the frequency of the power grid. This could be changed to a more realistic case with a transformer and transmission lines between the digital twin and the infinity bus.

To improve the digital twin, can either one of the mechanistic models be improved, or the system of mechanistic models can get a wider grasp of the entire hydropower process. A critical model that needs to be included in the aforementioned mechanistic model is the hydraulic system of the hydropower plant. The hydraulic system of the hydropower plant represents the water dynamics, as seen in Chapter 2. Does this depend on the

geometrical shape of the landscape close to the installed hydropower plant, as this affects the waterway and hence the behaviour of the water to changes in the rest of the digital twin. The hydraulic system plays a considerable role when putting together the rest of the digital twin, for instance, the configuration of the governor control, more specifically the transient droop as presented in Chapter 2.1.3, as this has to handle the waterway reaction to initial shifts in the gate valve position.

Moreover, will the waterway affect the choice of the turbine, which, as presented in Figure 2.2, represents changed efficiency at different load ratios. The generator's efficiency should be considered at a long term-life time reference, which is considerably altered when including the hydraulic efficiency with seasonal changes. The hydraulic system is part of the entire powerplant system. The typical use cases of the implemented digital twin would be of type S3 from Table 2.2, representing performance optimization. The expected behaviour of the synchronous generator can be significantly improved through simulations of operational states. Considering the test rig, for example, responses to parameter changes such as room temperature can be dynamically emulated, including varying operational loading of active and reactive power.

Further study of the behaviour can enable the system to be optimized regarding the possibility of using the controllable parameters to their strengths instead of possibly letting them be a synergetic power loss process. At a larger scale, to comply with changes in the other. For larger powerplant models that, for example, are cooled through a heat exchanger, can the twin allow simulations of different setpoints in the heat exchanger, together with planned production and expected power losses.

5.2 Parameter estimation

During the project work, several parameter estimation methods were applied in an attempt to address the sub-objectives (O6) and (O7). Chapter 5.2.1 addresses the findings concerning electrical parameter estimation applied to simulated measurements in Study Case A and applied to the test rig in Study Case B. Section 5.2.2 will address the findings concerning thermal parameter estimation, considering two separate measurement sessions from the test rig.

5.2.1 Electrical parameter estimation

Throughout the process of electrical parameters and state estimation, in total, four algorithms were considered. Where two of the algorithms, the Kalman Filter, (KF), and Bayesian Inference, (e1), consider the estimation of parameters at steady state operation.

Both require knowledge of either directional and quadrature voltage and currents or terminal PMU quantities with available rotor angle measurement. Given knowledge about the generator's parameters, the rotor angle can be measured or estimated, as presented in Chapter 2.2.3. The latter algorithms, Bayesian Inference, (e2), and the proposed extended Kalman Filter, EKF, are measures that can be applied to increase the certainty of rotor angle position as intermediate steps to the estimation of the parameters of the generator, ending with the implementation of one of the two first mentioned algorithms.

Case A

Study Case A, considered electrical parameter estimation based on a simulation with several setpoint changes for governor and AVR, providing several steady-state conditions for parameter estimation. The simulation includes measurements of the rotor angle, enabling direct usage of both the Kalman filter, KF, and Bayesian inference (e1) at steady state conditions. Both estimation methods presented promising results, with Bayesian Inference proving to be the superior estimation method of the two. The Kalman filter presented deviations in estimated parameters depending on both applied noise and initial parameter values, with increasing deviation when a greater noise was applied. The main parameters that are misestimated from the Kalman filter are the stator winding resistance as well as the directional axis reactance. The Bayesian Inference algorithm, on the other hand, estimated correct parameter values with very low deviations for all parameters estimated. At last, was the proposed extended Kalman filter applied, with different noise levels added to the rotor angle measurement. The filter proved promising results regarding filtering out the correct rotor angle. The higher deviation was seen at increased noise, yet, a reaction that is to be expected.

Case B

Study Case B, considered a measurement session with varying loading of both active and reactive power. Hence, enabling estimation of rotor angles and parameters through Bayesian Inference (e2), through the multiple steady-state operational conditions that were identified. The shape of the posterior distributions is interesting, as it proves that the non-linear system got multiple close-to-equilibrium points with multiple significant protrusions. The resulting posterior distribution from the Bayesian inference presented three reasonable estimates of the rotor angle, all within a 95 % confidence interval of 0.06 radians for the first steady-state condition, 0.05 radians for the second steady-state condition and 0.09 radians for the latter Case. Converting to degrees, does this give an estimate of the rotor angle with a 95 % certainty within a range of 2.9 to 5.2 degrees. The estimated reactances all presented a larger confidence interval from their mean posterior distribution, with the direct magnetizing reactance, X_{ad}, as the most confident estimate with a standard deviation of about 0.05 p.u. Considering the changes in delivered reactive

power for the considered steady-state operations, could the deviations in the estimation of the reactance stem from the changed degree of saturation during the session. The test rig open circuit curve, Figure 4.8, presents increasing saturation at nominal voltage and higher. The posterior distribution of the resistance in the stator winding did not seem to settle to a significant protrusion, yet, interpreting the kernel density estimation of the posterior distribution did, the resistance seem to increase during the session. When considering the temperature evolution during the session, presented in Chapter 4.4.1, the temperatures in the phase windings increased by about 3 Kelvin during the session. Considering Equation 2.44, will the increased temperature increase the resistance in the windings, hence is it expected that the estimated parameter would have an increased estimated value throughout the session. Still, the estimated resistance proved a significantly higher value than the previously estimated resistance. This can be explained by the assumed increase in resistance when applying alternating current, compared to the resistance when applying direct current, which was used to measure the resistance, further explained in Chapter 2.3.1.

The proposed extended Kalman filter, EKF, was applied to the calculated rotor angle throughout the measurement session, calculated by a stochastical approximation of the estimated quadrature reactance. Both Bayesian Inference, (e1), and the Kalman filter, KF were applied using the estimated rotor angle from the extended Kalman filter, with promising results. In the estimated parameters from the Kalman filter, all parameters are roughly estimated down to an error below $\pm$ 2 % in most cases. Only the stator resistance estimation was higher at high noise levels. The quadrature and directional magnetization reactance were the closest estimated values, with an error below 0.07 % in several estimates, yet, the mean estimates for the last 100 iterations prove a high deviation from the final estimates, with a high standard deviation, indicating that the filter is not fully converged and further measurements are needed. In Case of further measurement points, could the filter improve the estimation. The Bayesian Inference estimation presented both lowered standard deviations in estimated parameters and lowered correlation in the kernel density estimations, implying a more informative model compared to the parameters estimated through Bayesian Inference (e2).

5.2.2 Thermal parameter estimation

Thermal parameter estimation was done through Bayesian inference based on a linearized thermal model of the synchronous generator. The initially presented heat balance from the first law of thermodynamics was used as a basis for the developed thermal model. As a result of available measurements and known parameters of the synchronous generator test rig, the thermal model was reduced to a lumped capacitance model with a total heat transfer coefficient representing both radiation and convection. Two separate measurement sessions were considered in an attempt to validate the assumptions that were made when simplifying the thermal model.

Considering the stator parameter estimations, both resulting parameters proved consistency in regard to mass estimation, with the core being estimated to be 25.8 kg with a certainty of 95 % that the mass is within a range of 24.9-25.8 kg, and each stator winding estimated to be 6.7 kg, with a certainty of 95 % that the mass is within a range of 6.08-6.37 kg from both sessions. The estimated total heat transfer coefficients varied a bit when comparing the two estimations between the two measurement sessions, especially when considering the total heat transfer coefficient representing heat transfer between the core and stator windings. During the dynamic load session, the mean posterior estimated value at 6.7 W/K, while the constant load session presented a mean posterior estimate of -0.97 W/K. Simulation of the sessions with the different estimated parameters, presented in Appendix B, presents that simulated temperatures fit better at lower temperatures, while especially the core temperature deviates at higher temperatures. Considering the heat transfer processes from Chapter 2.4.2, higher deviations are expected at higher temperatures due to the simplification of including the radiation heat dissipation in a total heat transfer coefficient. The heat dissipation due to radiation is given by the temperature differences in absolute temperatures to the power of 4. Hence, the effect of radiation will be amplified at higher temperatures, while the simplified thermal model only considers the relative temperature differences.

The respective total heat transfer coefficients from surfaces to room temperature air are within the same range from both sessions for both the core and windings, something that is expected as the heat transfer process to the room temperature air is represented mainly by convection, hence a more fitting model than for the heat transfer between the objects.

Simulation of the temperatures proved promising results in both cases, with a R^2 value of 0.99 for most of the estimates. The estimation of phase winding 1 in the constant session proved the lowest 1 R^2 value with 0.975.

The thermal parameters of the rotor were not possible to be estimated in either of the measurement sessions. The rotor temperature had to be estimated through changes in the field winding resistance, resulting in fluctuating measurements with much noise, resulting in very broad estimates with unlikely mean. As the rotor thermal parameters only were considered to dissipate heat through convection to fluid, the thermal model of the rotor was greatly simplified, yet, the poor measurements of the rotor temperature through voltage and current measurements are arguably the main reason for the poor thermal parameter estimations. With an increased accuracy of the measurements could, the thermal model of the rotor temperature be further developed to include dissipation to surrounding objects also. Measurements of surface temperatures of the stator cage could allow the integration of radiation dissipation, as it will represent a significant portion of surrounding surface areas for the heat sources in the generator.

6 Conclusion and further work

In an attempt to address the problem statements, the data acquisition software was further developed with improved measurement and digital twin functionality. In an attempt to thoroughly validate the implemented functionality of the software and increase information about the test rig parameters, three rigorous parameter estimation studies were conducted. In Case A, simulated electrical measurements were used to estimate electrical parameters. In Case B, electrical parameters were estimated using measurements from the test rig. Lastly, in Case C, thermal parameters were estimated using measurements from the test rig. Estimation methods included Kalman filters for the electrical parameter estimation and Bayesian inference. Findings will be concluded in Section 6.1, and proposed further work in Section 6.2.

6.1 Conclusion

Study Case A presented a simulated session with governor and AVR setpoint changes. Electrical parameter estimation was applied at identified steady-state conditions throughout the simulation. Both a Kalman filter and Bayesian inference were applied as estimation methods. The Kalman filter was able to identify correct parameters at low noise levels, with improved results when feeding the correct initial parameters. At higher noise levels were, the general results less accurate, with the best accuracy when feeding zero initial parameters. With the latter presenting superior estimation accuracy. The proposed Extended Kalman Filter was also applied for filter validation, prior to a more vital role in Study case B, the filter showed promising results in estimating the rotor angle, even when subject to high noise scenarios.

In Study Case B, was Bayesian Inference applied with rotor angles included as parameters. The resulting rotor angles and estimated parameters were used to further analyze the parameters through the proposed Extended Kalman filter and Bayesian Inference without rotor angles as parameters, as well as through a Kalman filter. The final estimates of the Bayesian Inference presented more certain estimates with less standard deviation. In contrast, the estimates through the Kalman filter presented deviating results, further discussed in Chapter 5.2.1.

The last Study Case evaluated the estimation of thermal parameters to a developed lumped capacitance model of the synchronous generator. Two measurement sessions were considered in an attempt to validate the model and assumptions that were made. Thermal parameters were estimated using Bayesian Inference, and the resulting stator parameters proved consistent mass estimations and a somewhat consistent estimate of the total heat transfer coefficient from the surfaces to room temperature air. However, comparing the two results, the total heat transfer coefficient between core and stator windings deviated significantly. Hence, the results discard the simplification of assuming a total heat transfer coefficient, including both convection and radiation, for the dissipation between the objects.

Considering improvements in the data acquisition applications, the application moved from C# to LabVIEW. Furthermore, the presented electrical model of the synchronous generator electrical, power loss model, and thermal model of the generator was compiled into a digital twin, implemented as a part of the application, with included governor and AVR control. The measurement state of the application was also equipped with controlling functionality, including control of the DC-motor applied torque and speed and excitation current and voltage. Governor control was implemented as an option to control the DC motor, which is yet to be thoroughly tested. The implemented AVR control of the excitation proved unstable when discretized. As a result, it was not implemented into the control system of the DAQ.

6.2 Further work

The proposed extended Kalman filter proved promising results when compared to simulation results, although further experimental validation and tuning are necessary for better accuracy of the filter. The basic Kalman filter proved less accurate than the Bayesian inference estimations, yet, with the Kalman filter being able to run in real-time during measurement sessions, it could prove to be useful in providing increased operational information. Proposed further work in regard to increasing parameter estimation of the synchronous generator test rig is listed below.

- Implementation of Unscented Kalman filter.
- Implement the hydraulic system of the hydropower plant
- Include saturation in estimations.

Proposed Further work in regard to improving the test rig is listed below

- Improve accuracy of excitation voltages and currents
- Conduct conventional parameter estimation measures, enables comparison of the estimated

- Implementation of hardware AVR, enabling control over terminal voltage during different operational conditions.

Bibliography

[1] A. S. Kvalsund and A. Bazargan, 'Design and test procedures for synchronous machines in laboratory,' dissertation, University of South-Eastern Norway, Porsgrunn, 2021.

[2] F. A. Strøm, C. M. T. Pineda, G. Shahmohammadi and M. A. A. Jobayer, 'Test procedures and data acquisition for laboratory synchronous machines,' dissertation, University of South-Eastern Norway, Porsgrunn, 2022.

[3] E. G. Melfald, 'Thermal model parameter estimation of a hydroelectric generator using machine learning,' dissertation, University of South-Eastern Norway, Porsgrunn, 2020.

[4] 'What is a digital twin?' (2020), [Online]. Available: https://www.ibm.com/topics/what-is-a-digital-twin.

[5] 'What is a digital twin?' (2020), [Online]. Available: https://www.plm.automation.siemens.com/global/en/our-story/glossary/digital-twin/24465.

[6] 'Hardware-in-the -loop.' (), [Online]. Available: https://www.opal-rt.com/hardware-in-the-loop/.

[7] P. Kundur, *Power system stability and control.* New York, USA: McGraw-Hill, Inc., 1994.

[8] A. Kjølle, *HYDROPOWER IN NORWAY- Mechanical Equipment.* Trondheim, Norway: NTNU, 2001.

[9] M. Sinagra, V. Sammartano, C. Aricò, A. Collura and T. Tucciarelli, 'Cross-flow turbine design for variable operating conditions,' *Procedia Engineering*, vol. 70, pp. 1539–1548, 2014, 12th International Conference on Computing and Control for the Water Industry, CCWI2013, ISSN: 1877-7058. DOI: https://doi.org/10.1016/j.proeng.2014.02.170. [Online]. Available: https://www.sciencedirect.com/science/article/pii/S1877705814001726.

[10] P. Schavemaker, *Electrical Power System Essentials.* Hoboken, New Jersey, USA: Wiley-Blackwell, 2008.

[11] A. Goikoetxea, J. A. Barrena, M. Rodriguez-Vidal and F. Chivite, 'Frequency restoration in insular grids using ultracaps ess,' Jul. 2010, pp. 1280–1285. DOI: 10.1109/SPEEDAM.2010.5542084.

[12] J. W. B. Jan Machowski and D. J. Bumby, *Power System Dynamics : Stability and Control*. 2nd ed. New York, USA: Wiley, 2008.

[13] J. J. Grainger, W. D. Stevenson and G. W. Chang, *Power System Analysis*. McGraw-Hill Education, 2016.

[14] H. Hosseini, B. Tusi, N. Razmjooy and M. Khalilpoor, 'Optimum design of pss and svc controller for damping low frequency oscillation (lfo),' *Journal of Electrical Engineering and Technology*, vol. 1, p. 5, Dec. 2012. DOI: 10.1109/ICCIAutom.2011.6356631.

[15] 'Static exciter transfer functions (2016).' (2016), [Online]. Available: https://www.pscad.com/webhelp-v5-ol/Master_Library_Models/Machines/Exciter_Models/Static_Exciter_Transfer_Functions_(2016).htm#IEEE_Static_Exciter_Type_ST7C.

[16] E. D. C. Bortoni, B. T. D. Arujo and J. A. Jardini, 'Estimation of quadrature axis synchronousreactance using the constantexcitation test,' *IEEE Power and Energy Technology Systems Journal*, 2016.

[17] E. d. C. Bortoni, R. T. Siniscalchi, S. Vaschetto, M. A. Darmani and A. Cavagnino, 'Efficiency mapping and weighted average efficiency for large hydrogenerators,' *IEEE Open Journal of Industry Applications*, vol. 2, pp. 11–20, 2021. DOI: 10.1109/OJIA.2020.3048989.

[18] Y. C. Karekezi, T. Øyvang and J. K. Nøland, 'The Energy Transition's Impact on the Accumulated Average Efficiency of Large Hydrogenerators,' Oct. 2021. DOI: 10.36227/techrxiv.16834195.v1. [Online]. Available: https://www.techrxiv.org/articles/preprint/The_Energy_Transition_s_Impact_on_the_Accumulated_Average_Efficiency_of_Large_Hydrogenerators/16834195.

[19] F. P. Incropera, D. P. DeWitt, T. L. Bergman and A. S. Lavine, *Incropera's Principles of heat and mass transfer*, 8th edition. Hoboken, New Jersey, USA: Wiley, 2017.

[20] G. E. P. Box and G. M. Jenkins, *Time series analysis forecasting and control*, Revised Edition. San Francisco, USA: Holden-Day, 1976.

[21] Y. V. Kim, *Kalman Filter - Engineering Application*. London, United Kingdom: IntechOpen, 2023.

[22] F. Gustafsson, *Statistical sensor fusion*, 8th edition. Hoboken, New Jersey, USA: Wiley, 2017.

[23] W. von der Linden, V. Dose and U. von Toussaint, *Bayesian Probability Theory-Applications in the Physical Sciences*. Cambridge, United Kingdom: Cambridge University Press, 2014.

[24] A. Chugh. 'Mae, mse, rmse, coefficient of determination, adjusted r squared — which metric is better?' (2020), [Online]. Available: https://medium.com/analytics-vidhya/mae-mse-rmse-coefficient-of-determination-adjusted-r-squared-which-metric-is-better-cd0326a5697e.

[25] H. P. Halvorsen. 'Labview applications using state machine,' Youtube. (2020), [Online]. Available: https://www.youtube.com/watch?v=-b9St8wNhpQ.

[26] E. F. Alves, J. K. N land, G. Marafioti and G. Mathisen, 'Online parameter identification of synchronous machines using kalman filter and recursive least squares,' in *IECON 2019 - 45th Annual Conference of the IEEE Industrial Electronics Society*, vol. 1, 2019, pp. 7121–7128. DOI: 10.1109/IECON.2019.8926707.

[27] 'Temperature coefficient of resistance.' (), [Online]. Available: https://www.allaboutcircuits.com/textbook/direct-current/chpt-12/temperature-coefficient-resistance/.

[28] 'Specific heat capacity of materials.' (2016), [Online]. Available: https://theengineeringmindset.com/specific-heat-capacity-of-materials/.

Appendix A

Task description of the Master Thesis

This appendix presents the task description for the Master Thesis.

University of South-Eastern Norway

Faculty of Technology, Natural Sciences and Maritime Sciences, Campus Porsgrunn

FMH606 Master's Thesis

Title: Data acquisition, digital twin, and controller implementation of in-house generator lab

USN supervisor: Thomas Øyvang(Main supervisor) and Emil Melfald (co-supervisor)

External partner: Kelda (Ole Magnus Brastein) and Tinfos (Ole Petter Bjørnstad)

Task background:
USN has had a generator laboratory used by students for manual control and testing of a 2 kW synchronous machine, driven by a 10 kW DC machine as the primary runner. The desire for a more automated control system, together with better measurement and data acquisition techniques, has been requested by current research activity at USN. The work will develop digital twins and advanced control schemes and strengthen cooperation between USN and other partners by having a test rig for synchronous machine tests. In Autumn 2022, a master project developed a prototype data acquisition software compatible with the installed Compact DAQ hardware in the lab. The main tasks of this master thesis will build upon the work accomplished in that project.

Task description:
The main task of this thesis includes further development of the data acquisition software made from the master project subject. The extension of the software should focus on implementing control loops relevant to hydropower plants, more specifically, control of active power and voltage through a governor and AVR, respectively. The work should support acquiring data at user-specified intervals and real-time data processing. The real-time data processing variables should be implemented as soft sensors through simple mechanistic models of the generator at the lab. Real-time data processing should be able to provide state estimation of both the thermal and electrical aspects of the synchronous machine. The software should support storing user-specified sensor measurements locally and in a cloud-based database. Summarized in the following list are the objectives for the student working towards the primary goal of this thesis:

- Do a survey on digital twin of hydro power modelling and control systems.
- The software should be developed to control the synchronous machine. A governor for active power, a PID speed controller, and an AVR for voltage regulation should be implemented. In addition, if time allows tune controllers towards IEEE standards and Norwegian standards and implement simple overexcitation and stator current limiters. (OXL/SCL)
- A simple electrical model of the generator, e.g., a third-order model and a lumped parameter thermal model from [1], should be implemented in LabView.
- Implement an already developed loss model of the synchronous machine.
- Controllers should be tested on the generator lab setup, with control through the Compact DAQ.
- Collect a sufficient amount of data from the generator through test runs to estimate the model parameters of the lab generator for both the thermal and electrical models. In addition, if time allows, expand data collection to an external study case.

- Implement a Kalman filter for real-time state estimation of the synchronous generator states and variables, and do proper verification tests of the filters.
- The work should be compiled into a paper manuscript for further publication.

Student category: Reserved for EPE student Fredrik Andre Strøm

Is the task suitable for online students (not present at the campus)? No

Practical arrangements:
Regular lab sessions at the USN laboratory in Porsgrunn

Supervision:
As a general rule, the student is entitled to 15-20 hours of supervision. This includes necessary time for the supervisor to prepare for supervision meetings (reading material to be discussed, etc).

Signatures:

Supervisor (date and signature): Thomas Øyvang 01.02.2023

Student (write clearly in all capitalized letters): FREDRIK ANDRE STRØM

Student (date and signature):

31/01-23

References:

[1] E. G. Melfald, «Thermal model parameter estimation of a hydroelectric generator using machine learning,» University of South-Eastern Norway, Porsgrunn, 2020.

Appendix B

Measurements of interest

This appendix contains figures, measurements and results that are referenced in the report, yet, for readability, are placed here.

Electrical parameter estimation - simulation

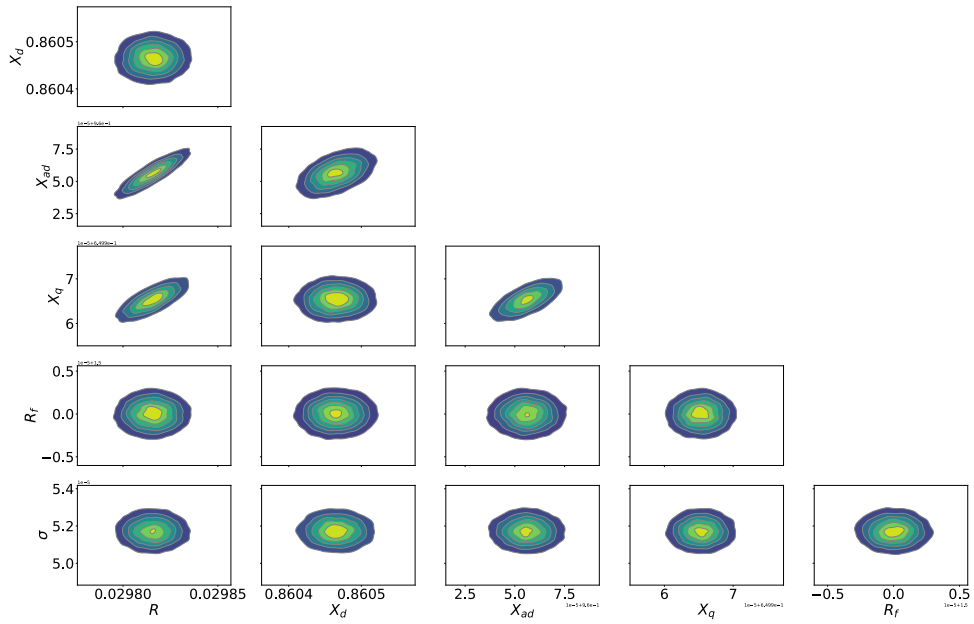

Figure B.1: Kernel density estimation of estimated parameters

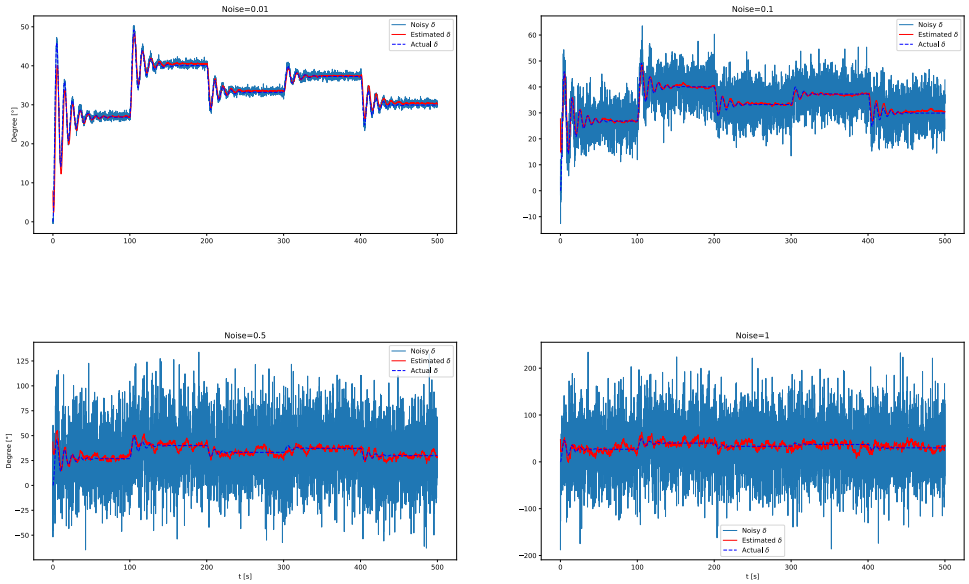

Figure B.2: Estimated rotor angle with the noisy rotor angle measurement included

Electrical parameter estimation - test rig

This section presents measurements and results that are obtained from the electrical parameter estimation of the measurement session. Measurement files are found in Appendix D.1.

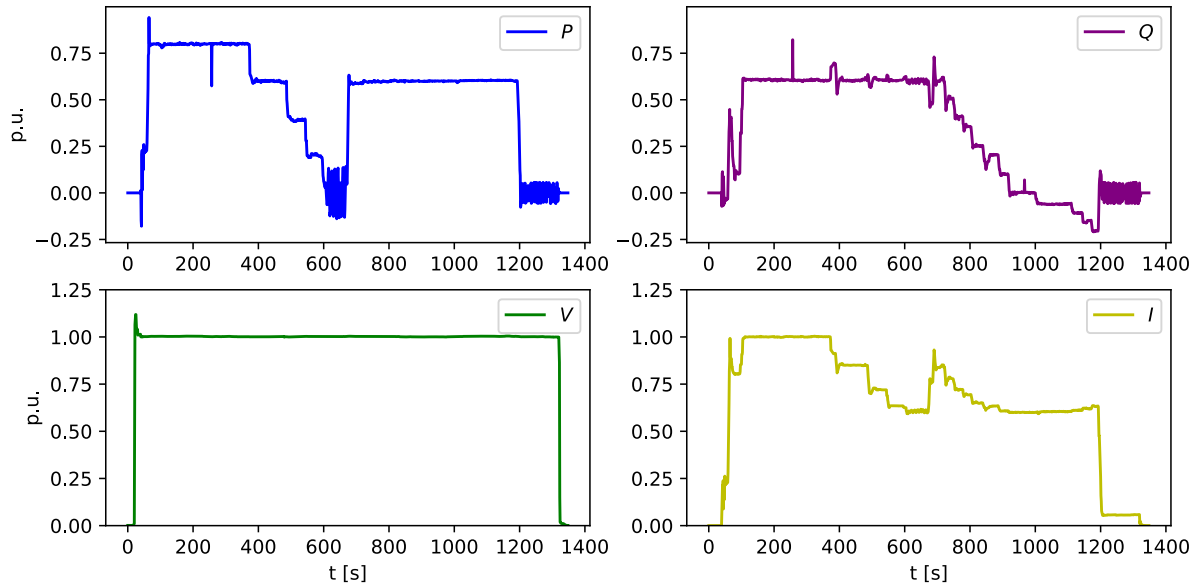

Figure B.3: Measurements considered for electrical parameter estimation with noise.

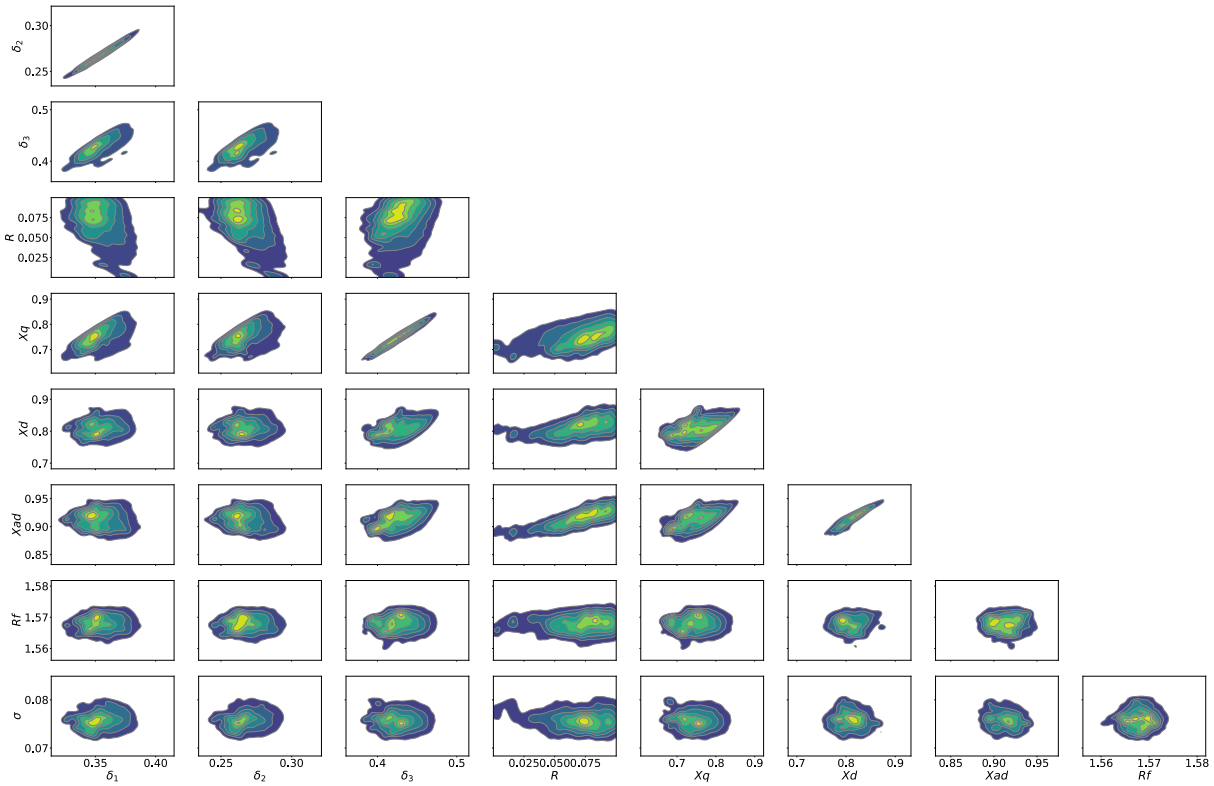

Figure B.4: Kernel density estimation for estimated posterior distributions of rotor angles and parameters during the session.

Bayesian estimation using rotor angle estimated from EKF.

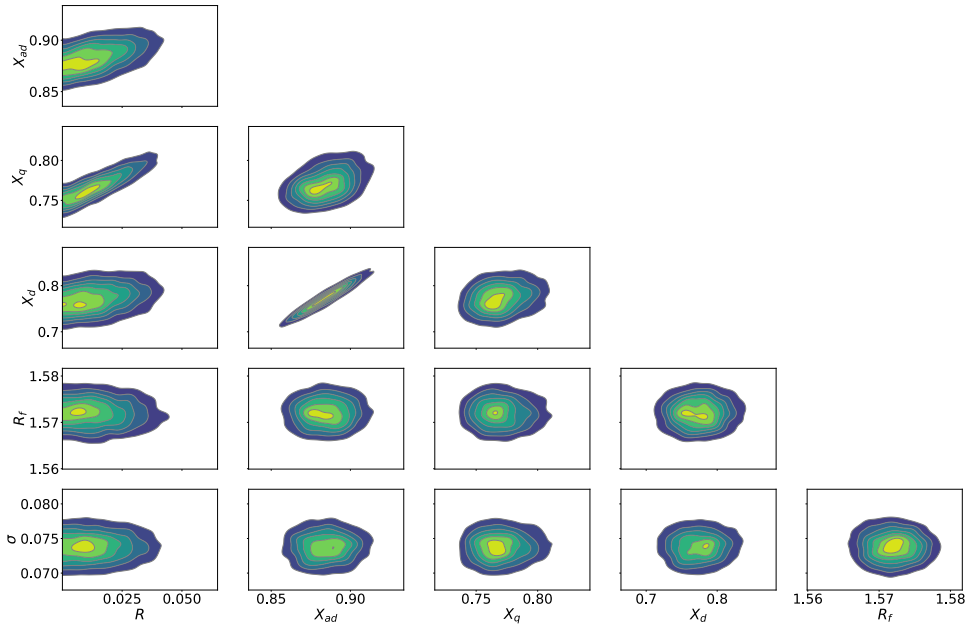

Figure B.5: Kernel density estimation- post rotor angle estimation

Thermal parameter estimation

This section presents measurements from the thermal measurements sessions during the project work.

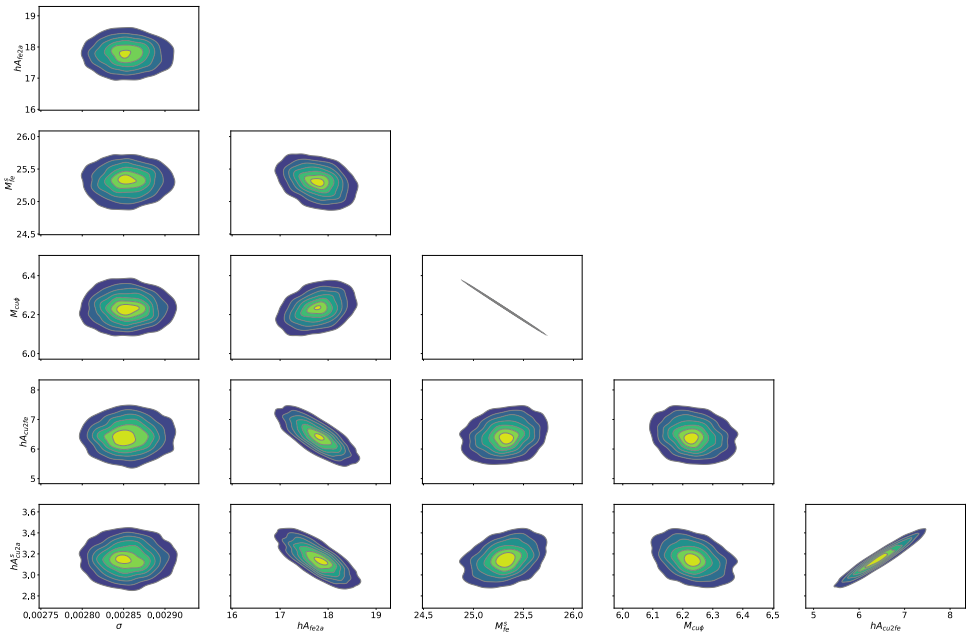

Figure B.6: Kernel density estimation - dynamic load session

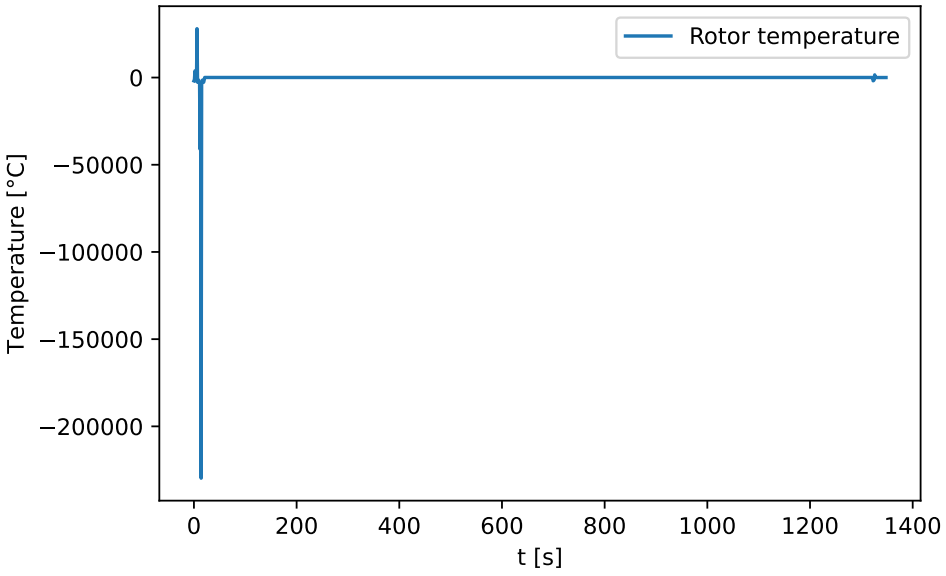

Figure B.7: Estimated rotor temperatures with noise

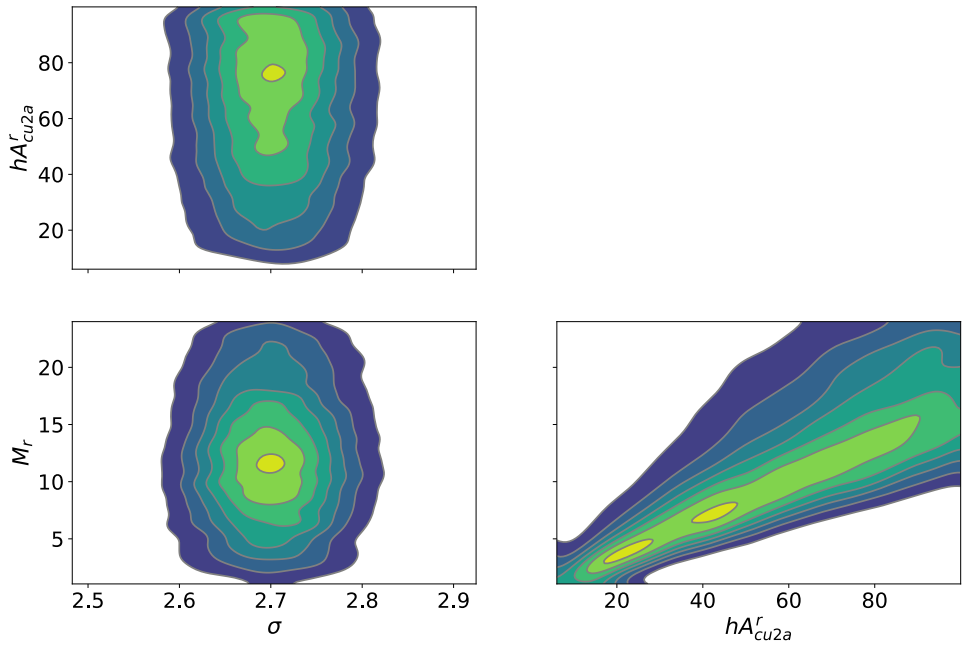

Figure B.8: Kernel density estimation of rotor parameters - dynamic session

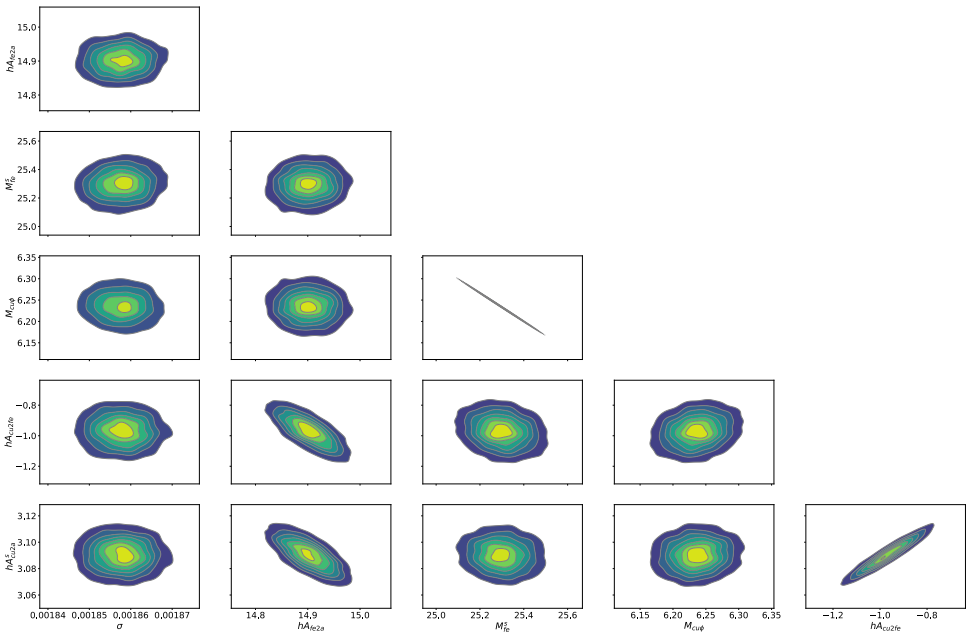

Figure B.9: Kernel density estimation - steady state session

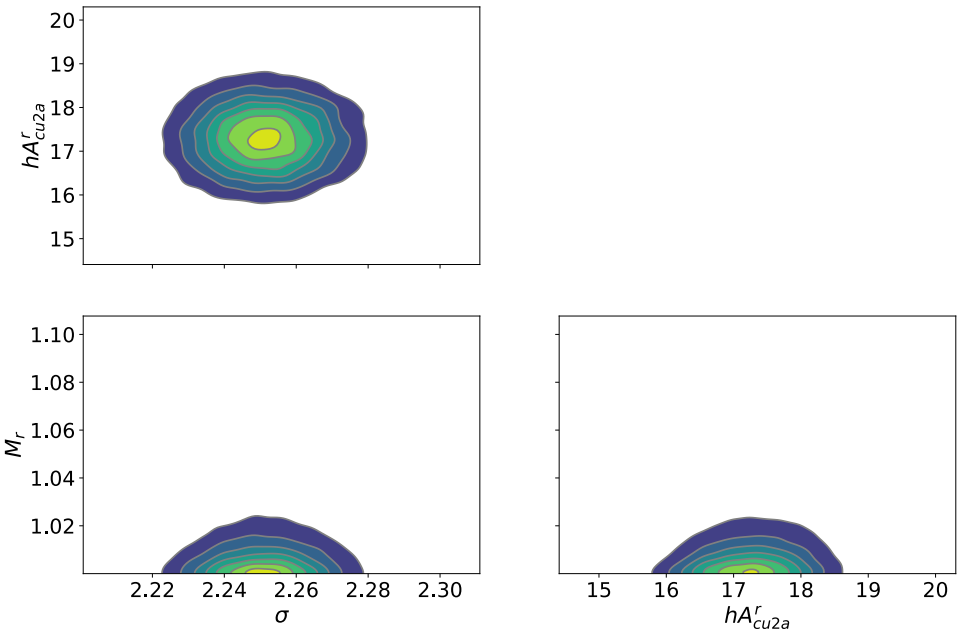

Figure B.10: Kernel density estimation of rotor parameters - steady state session

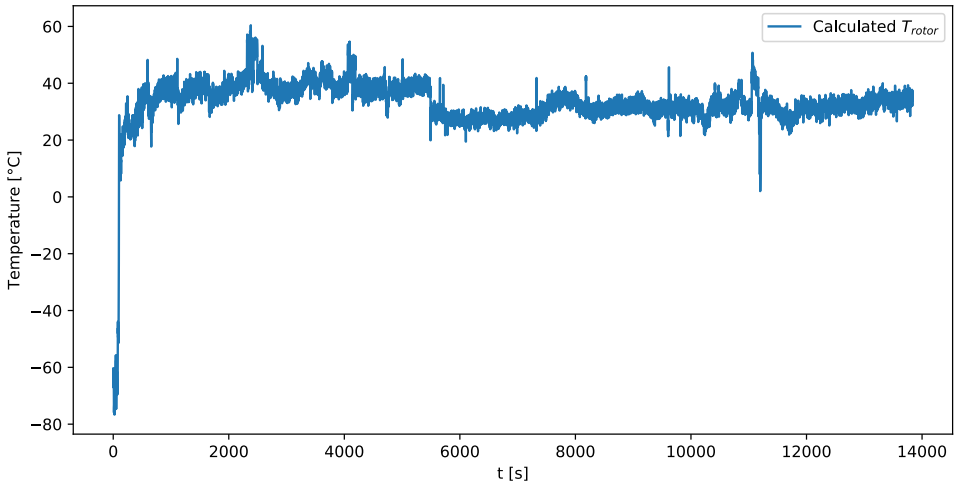

Figure B.11: Estimated rotor temperatures with noise

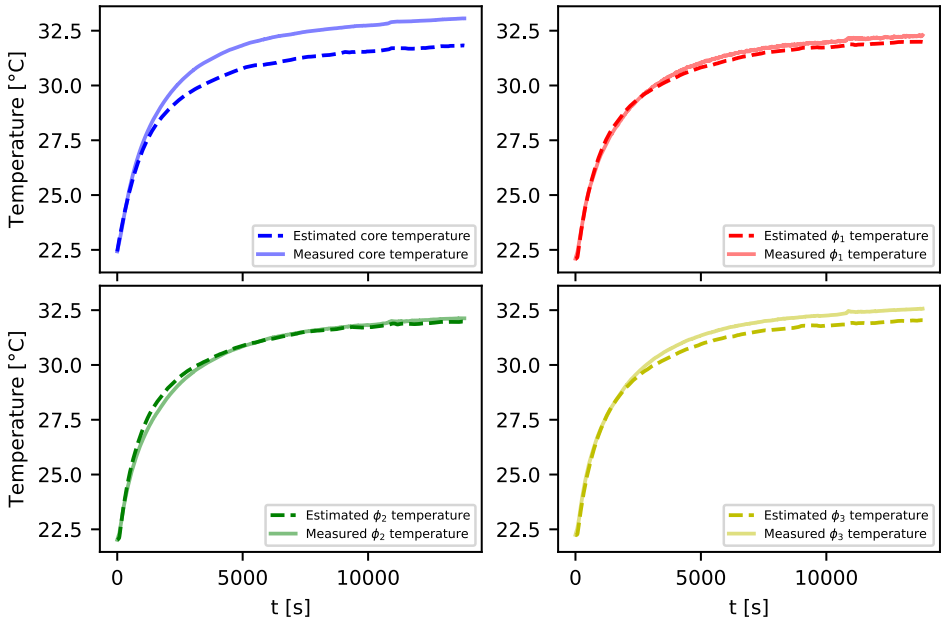

Figure B.12: Simulation of the steady state session using the estimated thermal parameters from the dynamic measurement session.

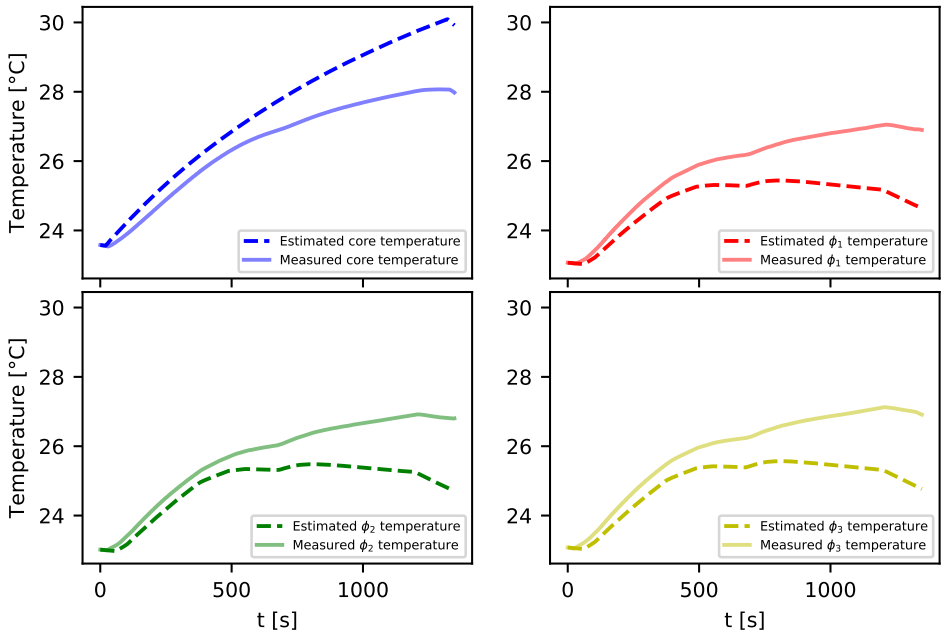

Figure B.13: Simulation of the dynamic load session using the estimated thermal parameters from the steady state measurement session.

Appendix C

Calibration of torque sensor and estimation of nominal losses

This appendix presents the journal from the calibration lab session, measurements used in the Journal are available in Appendix E5. With the filenames:

- *Stray_losses_measurements*
- *Torque_calibration_measurements*
- *Core_loss_measurements*
- *Friction_measurements*

University of South-Eastern Norway
Faculty of Technology, Natural Sciences and Maritime Sciences
Study programme: M.Sc. - Electrical Power Engineering

–

Laboratory journal
Lab date: 20.04.23

Calibration of torque sensor and estimation of losses

Contents

1. Purpose

The laboratory session will through linear regression estimate a scaling factor for determining the input torque provided to the rotor of the synchronous generator from the DC motor. The DC motor will Test object.

2. Test object

The test object for the laboratory session is the synchronous generator test rig, specifications given in figure 1.

DC resistance measurements of the armature windings have estimated a phase resistance of $0.804\ \Omega$.

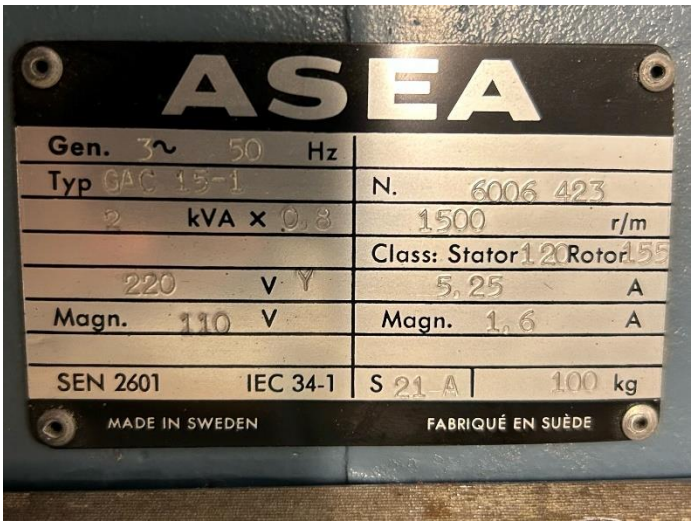

Figure 1, Generator specifications

3. Experimental set-up

The setup for calibration of the torque sensor is presented in figure 2.

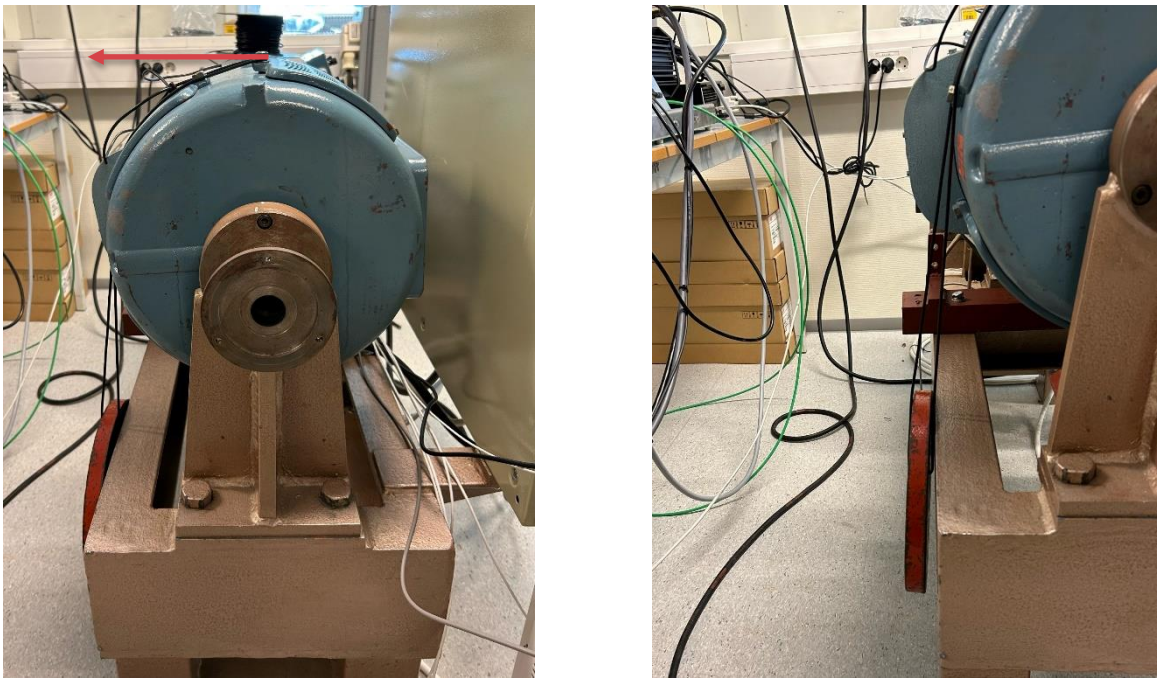

Figure 2, Setup torque calibration

There was taken supplementary measurements to the setup in figure 2, listed in table 1.

Table 1, Measurements

Measured object	Distance from center of inertia [cm]
Length Torque Sensor arm	20
Center of inertia to bearing	29,9
Height of bearing	5,7
Bearing to the force sensor	4,2
Center of inertia to force sensor	20
Radius from center of inertia to point of weight attachment	17,9-18,3

4. Procedure

3.1 Torque estimation

The estimation of the torque will be done by measuring physical scales and determining the radius from center of inertia to the sensor pressure point. There will be mounted assumed known weights while measuring the output mounted from the mounted sensor. The angle of the weights was

estimated from measurements of the tangential point and length of the rope and estimated center of inertia.

3.2 Nominal loss estimation

The nominal losses will be estimated through three sessions:

The first session will determine the nominal friction and windage loss, given as the loss at the nominal angular velocity, without magnetization:

$$P_{f\&w}^{*} = \tau\omega \quad |_{\omega=\omega_s}$$

The second session will determine the nominal core loss, given as a difference from the friction losses to the losses at the nominal angular velocity, with magnetization giving rated voltage at the armature.

$$P_{core}^{*} = \tau\omega - P_{f\&w} \quad |_{\omega=\omega_s, V=V_n}$$

The third session will determine the nominal stray losses, given as the losses not accounted for by friction, core, or ohmic losses. The nominal stray load losses are given as input torque at rated load, the rated load.

$$P_s = \tau\omega - P_e - P_{core}^{*} - P_{f\&w}^{*} - P_a \quad |_{P=P_n, Q=Q_n}$$

5. Results

5.1 Calibration of torque

The angle of the weight was estimated to 5.7 °, altering the effective gravitational acceleration.

$$g = 9.81 \cdot \cos 5.7° = 9.76\, m/s^2$$

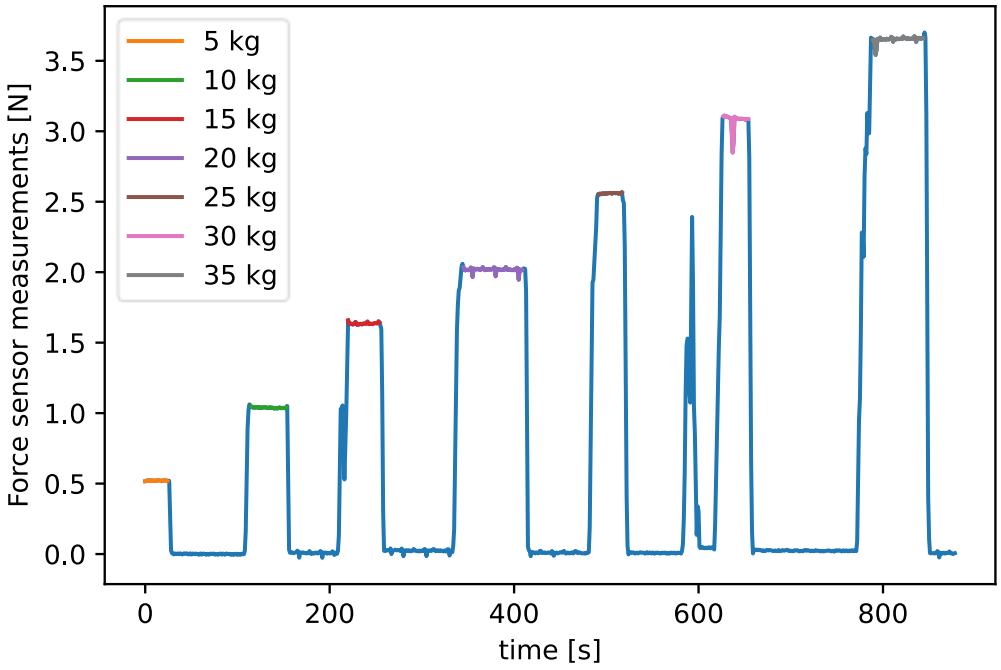

Figure 3, Torque measurements at different weights with removed bias 0.12

The measured values at each weight were accounted into a mean value for each weight, the mean weight was used to calculate torque together with the distance from center of inertia, as

$$\tau = F \cdot r$$

Assuming the force to be perpendicular to the center of inertia. The measured and applied force was scaled to torque, using the equation above and distance from sensor and applied weight to center of inertia. Scipy curve fitting was applied to curve fit the measurements to a linear curve. The estimated curve is plotted together with the equation and the R^2 of the estimated parameters and the measurements in figure 4.

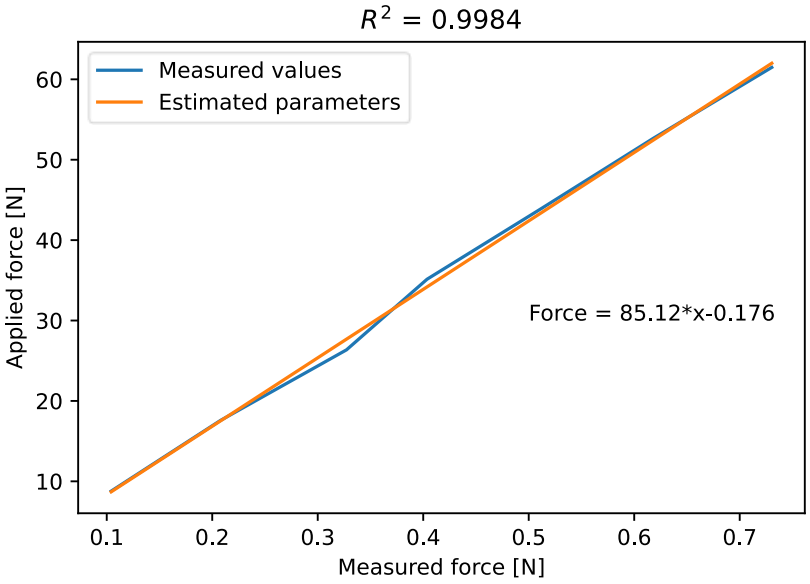

Figure 4, Curve fitted line

The resulting scale for estimation of force applied to the torque sensor is given as

$$F = 85.12 \cdot x - 0.176[N]$$

Where x is the value from the sensor with the bias subtracted. Hence will the torque and Pmec be given as

$$\tau = F \cdot r = (85.12 \cdot x - 0.176) \cdot 0.2\ [Nm]$$

$$P_{mec} = \tau \cdot \omega_{mec} = (85.12 \cdot x - 0.176) \cdot 0.2 \cdot \frac{2\pi f}{\#p}\ [W]$$

Where ω_{mec} is given as mechanical rad/s, and #p is the pole pairs.

5.2 Nominal losses estimation

Using the calibrated estimate of the torque, the nominal losses are plotted in figure 5-8.

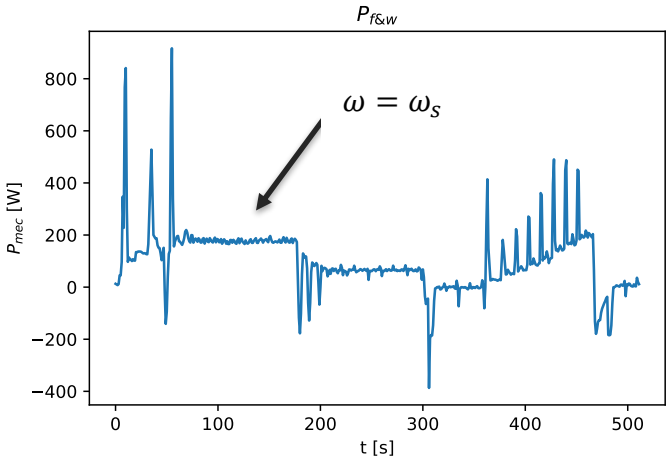

Figure 5, Measured Pmec for estimation of friction and windage losses

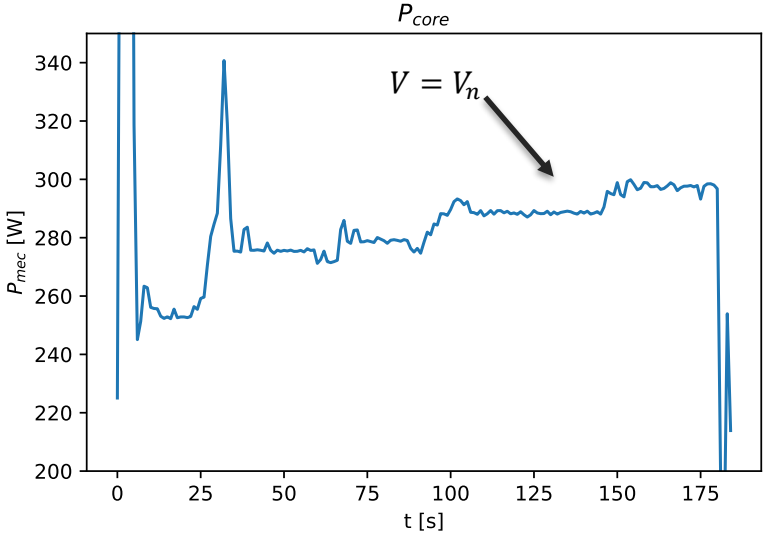

Figure 6, Measured Pmec for estimation of core losses

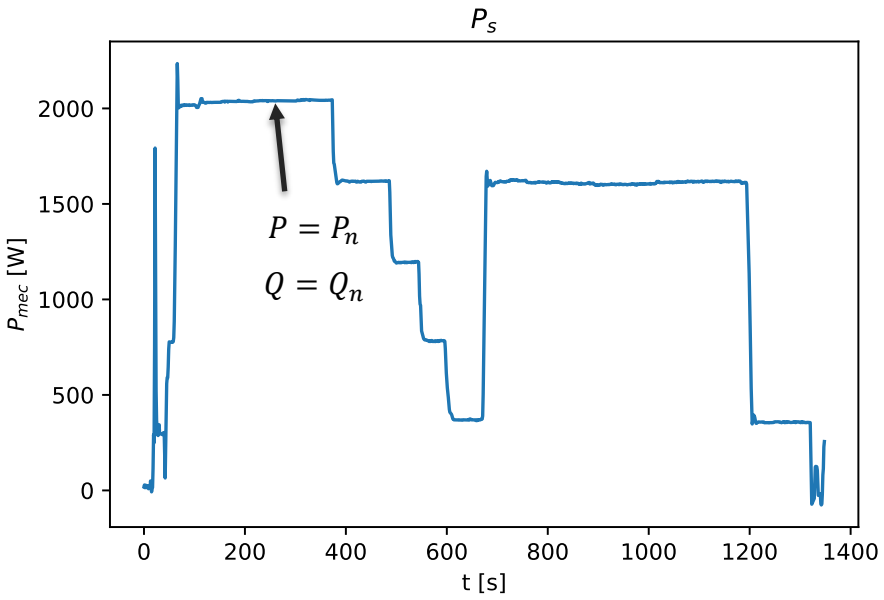

Figure 7, Measured Pmec for nominal stray loss

Summarized nominal losses, calculated by equations in section 4.2 is given in table 2.

Table 2, Nominal losses

Measured object	Loss [W]
$P^*_{f\&w}$	176.0
P^*_{core}	113.2
P^*_s	87.7

6. Conclusion

An input mechanical power scale for the force sensor was proposed and the nominal losses were estimated based on assumed losses at different operational points. Rotor ohmic losses from excitation does not contribute to increased torque. Assumed room temperature in armature windings during load at stray losses.

Appendix D

Electronic Appendices

The LabVIEW software developed as part of the project, together with relevant measurements obtained during the thesis, are included as electronic appendices. They are not included as part of the report as they take up a lot of pages, yet, they are included as they are part of the thesis work.

Appendix number	**Description**
Appendix E1	README file, which further explain the electronically submitted appendices
Appendix E2	LabView Project Folder
Appendix E3	Powerpoint file with presentation videos, showcasing the use of the developed application's main features.
Appendix E4	Python Scripts used for parameter/state estimation and analysis/plotting of obtained data.
Appendix E5	Relevant measurement files obtained throughout the project work
Appendix E6	LabView application aliases
Appendix E7	SQL database setup